U.PORTO
FEUP FACULDADE DE ENGENHARIA
UNIVERSIDADE DO PORTO

MSc Thesis

Modal Analysis of a FOWT under Different Modelling Techniques

Afonso Ribeiro Faro

Supervisors:
Rui Filipe Magalhães Couto
Manuel António Rodrigues Franco
Pedro Leal Ribeiro

Document submitted in partial fulfilment of the requirements
for the degree of Master of Science

Porto, September 2025

"If something seems completely doomed, just give it a little more time. Worst case scenario, you get to be right."

Jon Bois

Modal Analysis of FOWT under Different Modelling Techniques

Afonso Ribeiro Faro

Abstract

This thesis investigates the coupled dynamic response of a semisubmersible floating offshore wind turbine (FOWT) using two modelling strategies in OrcaFlex: a simplified *beam* model and a diffraction-based *vessel* model (frequency-dependent added mass, radiation damping, and second-order wave loads). Three operating scenarios are analysed across a range of wind speeds: (A) regular waves with steady wind, (B) irregular waves with steady wind, and (C) irregular waves with turbulent wind.

The principal result is a consistent separation between the first coupled tower-platform frequency bands predicted by the two models: the beam model clusters around 0.48–0.49 Hz whereas the vessel model yields 0.43–0.44 Hz, evidencing a systematic softening from hydrodynamic compliance in the vessel formulation. Across Scenarios A–C the bands remain relatively tight; the beam model shows small seed-to-seed scatter, while the vessel model exhibits higher variability due to sensitivity to wave radiation/diffraction and second-order effects. Identification is further complicated by deterministic rotor harmonics: the $3P$ band can overlap the structural peak (notably at mid-range winds), and, together with turbulence in Scenario C, leads to visibly broader and sometimes ambiguous peaks.

Overall, the study quantifies a clear trade-off: the beam model offers robustness and repeatability with modest input requirements, while the vessel model delivers higher physical fidelity at the cost of greater data demands and sensitivity. These insights support model-choice decisions for design studies, validation exercises, and operational modal analysis pipelines.

Keywords: Floating offshore wind turbine; semisubmersible platforms; coupling modes; radiation–diffraction hydrodynamics; added mass and radiation damping; response amplitude operators (RAOs).

Modal Analysis of FOWT under Different Modelling Techniques

Afonso Ribeiro Faro

Resumo

Esta dissertação analisa a resposta dinâmica acoplada de uma turbina eólica offshore flutuante (FOWT) com plataforma semissubmersível, comparando duas estratégias de modelação no OrcaFlex: um modelo *de vigas* e um modelo por difração (massa adicionada e amortecimento por radiação dependentes da frequência e esforços de segunda ordem). Consideram-se três cenários operacionais ao longo de várias velocidades de vento: (A) ondas regulares com vento estacionário, (B) ondas irregulares com vento estacionário e (C) ondas irregulares com vento turbulento.

Constata-se uma separação sistemática entre as bandas de frequência da primeira flexão da torre: o modelo de linhas concentra-se em 0.48–0.49 Hz, enquanto o modelo de difração apresenta 0.43–0.44 Hz, refletindo o amolecimento devido à conformidade hidrodinâmica. As bandas mantêm-se pequenas nos três cenários; o modelo de linhas mostra reduzida dispersão entre sementes, ao passo que o modelo de difração é mais sensível à radiação/difração e a efeitos de segunda ordem. A identificação modal é dificultada pelos harmónicos do rotor: o $3P$ pode sobrepor-se ao pico estrutural (sobretudo a ventos médios) e, em conjunto com a turbulência do Cenário C, origina picos mais largos e por vezes ambíguos.

Em síntese, evidencia-se um compromisso: o modelo de linhas é robusto e repetível com menores requisitos de entrada, enquanto o modelo de difração oferece maior fidelidade física, exigindo bases hidrodinâmicas extensas e revelando maior sensibilidade. Estes resultados apoiam a escolha de modelos para estudos de projeto, validação e análise modal operacional.

Palavras-chave: Turbina eólica offshore flutuante; plataformas semissubmersíveis; modos de acoplamento; hidrodinâmica de radiação–difração; massa adicionada e amortecimento por radiação; operadores de amplitude de resposta (RAOs).

Acknowledgments

I would first like to express my deep gratitude to my company supervisor, Eng. Rui Filipe Magalhães Couto, whose tireless dedication was central throughout this process. His guidance extended far beyond technical discussions, providing reassurance, structure, and foresight at every stage. I am equally thankful for his role in integrating me into the LaC Team at Vestas, which created a highly valuable professional and personal experience in an environment that shaped me as a young engineer.

I also thank my company co-supervisor, Eng. Manuel António Rodrigues Franco, for his consistent support and insight. This acknowledgment extends to the entire LaC Team, whose diverse expertise was essential whenever new challenges emerged. Their willingness to contribute made this journey richer and more rewarding.

I would also like to express my gratitude to Professor Pedro Leal Ribeiro for his guidance and support throughout this dissertation. His availability, constructive feedback, and insightful perspective were invaluable in keeping this work on track and ensuring its quality. I am truly thankful for his role as an academic supervisor and for the trust and encouragement he provided during this process.

To my parents, I dedicate this work as the culmination not only of five demanding years of studies, but of twenty-three years of unconditional care. Their patience, example, and guidance have been fundamental in shaping who I am today, and for that I will remain forever grateful.

To Francisco, Guilherme, Filipa, Maria Miguel, Maria Inês, Mia, and Rita, I owe heartfelt thanks for being an inseparable part of this journey. Although our paths first crossed through “work”, it soon became much more than that: countless shared experiences (with much more to come!) have shaped a friendship that I deeply treasure, and that has been fundamental to my growth as a person, in ways you might not even realise.

Finally, but certainly not least, to André, Beatriz, Diogo, João, and Miguel: far more than classmates, you have been companions with whom I shared the triumphs and struggles of these five years. Your presence turned the path into something truly meaningful, and a major reason why every effort was worthwhile.

Contents

List of Tables

List of Figures

List of Abbreviations

Table 0.1: List of abbreviations (in order of appearance).

Abbreviation	**Meaning**
FOWT	Floating Offshore Wind Turbine
OWT	Offshore Wind Turbine
OC4	DeepCWind OC4 semisubmersible platform
NREL	National Renewable Energy Laboratory
RAO	Response Amplitude Operator
QTF	Quadratic Transfer Function
OMA	Operational Modal Analysis
FA / SS	Fore–aft / Side–side (tower directions)
DoF	Degree(s) of freedom
1P / 3P	Once-/Three-per-revolution rotor harmonics
RPM	Revolutions per minute
PM	Pierson–Moskowitz wave spectrum
JONSWAP	Joint North Sea Wave Project spectrum
NTM	Normal Turbulence Model
DLC	Design Load Case
HAWC2	DTU aeroelastic simulation code
OpenFAST	NREL aero–hydro–servo–elastic simulation code
WAMIT	Diffraction–radiation hydrodynamics solver
BEM	Blade-Element–Momentum aerodynamics
TMD	Tuned Mass Damper
TLP	Tension-Leg Platform
CFD	Computational Fluid Dynamics
SSI-COV	Covariance-Driven Stochastic Subspace Identification
PSD	Power Spectral Density
CoM	Centre of mass

Chapter 1

Introduction

1.1 Context

Global efforts to combat climate change and achieve net-zero emissions by mid-century have placed a premium on expanding renewable energy sources. Offshore wind power has rapidly emerged as a cornerstone of this clean energy transition, capable of delivering large-scale, reliable zero-carbon electricity [1]. Offshore wind is considered the renewable energy technology with the highest decarbonization potential per MW installed [1]. Yet, despite a global technical potential estimated at more than 71,000 GW (including floating platforms), only a fraction of this capacity has been deployed to date [1]. Bridging this gap will require accelerated deployment of offshore wind farms, supported by continuous innovation and investment.

A key enabling technology is the floating offshore wind turbine (FOWT). Traditional fixed-bottom turbines are constrained to relatively shallow waters (typically not exceeding 50–80 m depth) where they can be anchored to the seabed [2]. Floating platforms remove this restriction, allowing installation in deep waters with stronger and more consistent winds [2]. They also offer reduced visual impact from land and the potential for higher capacity factors, as turbines can be sited farther offshore [2]. These features make floating wind particularly attractive for countries with steep continental shelves, where conventional foundations are not viable.

At the same time, floating wind introduces significant engineering challenges. Unlike bottom-fixed structures, FOWTs operate as fully coupled aero–hydro–servo–elastic systems subject to dynamic loads from wind, waves, and currents. Their performance and long-term reliability depend on complex interactions between structural flexibility, hydrodynamic response, and control system behaviour. This complexity creates uncertainties not only in the design phase but also in predicting operating conditions, assessing fatigue, and planning maintenance. Moreover, the possibility of dynamic instabilities – such as excessive platform motions, resonance phenomena, or negative damping effects – further underlines the importance of robust design. Consequently, accurate numerical modelling and simulation of FOWT dynamics are essential: first, to evaluate the feasibility of deployment at a given site; second, to predict in-service behaviour under diverse environmental conditions; and third, to develop strategies for monitoring and maintenance throughout the turbine's lifetime.

The present thesis is framed within this context, contributing to the broader effort of improving modelling approaches for floating offshore wind turbines. By focusing on the dynamic response of a semisubmersible platform, the work supports the reliable prediction of natural frequencies and modal interactions under realistic operating conditions, which is a critical step toward ensuring safe, cost-effective, and sustainable deployment of floating wind technology.

1.2 Objectives

The thesis aims to characterise and compare the coupled dynamic response of a semisubmersible FOWT using two modelling strategies in OrcaFlex. The specific objectives are:

- Compare a simplified *beam model* (rigid platform assembled from line elements) with a diffraction-based *vessel model* (frequency-dependent added mass, radiation damping, first/second-order wave loads).
- Validate both models via chirp excitation and free-decay (winch-release) tests to establish baseline frequencies.
- Under three different Scenarios (regular+steady wind; irregular+steady wind; irregular+turbulent wind), quantify frequency bands, their tightness across seeds, and sensitivity to the modelling choice.
- Benchmark against HAWC2 simulations and published values where possible; discuss practical trade-offs between fidelity and robustness.

1.3 United Nations Sustainable Development Goals

This thesis directly aligns with several of the United Nations Sustainable Development Goals (SDGs) by advancing renewable energy technology and its applications:

- **Affordable and Clean Energy**: Developing floating offshore wind contributes to this goal by increasing the supply of sustainable electricity. FOWTs open up new areas for wind power generation, which helps provide clean energy access on a large scale and at declining costs, thereby supporting the transition to affordable low-carbon power in line with SDG 7.
- **Industry, Innovation and Infrastructure**: Floating wind technology embodies innovation in engineering and infrastructure for clean energy. This thesis' focus on advanced modelling of FOWT dynamics supports technological innovation and improved design methods in the offshore wind industry. The knowledge gained contributes to building reliable renewable energy infrastructure (offshore wind farms) and fosters industrial expertise in an emerging sector, aligning with the targets of SDG 9.
- **Climate Action**: Floating offshore wind directly supports climate action by enabling more deployment of wind energy, especially in regions where fixed turbines are not feasible. By

helping to decarbonize electricity generation, FOWTs contribute to mitigating climate change. The research and developments in this thesis thus aid in expanding clean energy capacity, which is crucial for meeting climate targets under the Paris Agreement and SDG 13.

In summary, by improving floating wind turbine technology and facilitating its adoption, the work of this thesis advances global goals on clean energy access, innovation in sustainable infrastructure, and urgent climate change mitigation. These contributions also indirectly support other goals, such as SDG 8 (Decent Work and Economic Growth), by spurring a new green industry and job creation, and SDG 14 (Life Below Water), by promoting sustainable use of ocean resources for energy. The thesis underscores the interdisciplinary impact of engineering research on broader sustainability objectives.

1.4 Relevance in Portugal's Geography and Industry

Portugal's geographic conditions make it especially well-suited for floating wind solutions for offshore energy development. The country possesses a lengthy Atlantic coastline with strong wind resources, but its continental shelf descends sharply into deep waters only a short distance from shore [3]. In practical terms, this means conventional bottom-fixed turbines are largely infeasible beyond near-coastal areas, compelling Portugal to explore floating platform technology. Out of this necessity, Portugal became a pioneer in floating wind: it is home to the world's first semi-submersible floating wind farm, the WindFloat Atlantic project [4]. This pilot wind farm, operating since 2020, consists of three 8.4 MW turbines (25 MW total) mounted on floating platforms about 18 km off the coast of Viana do Castelo in water depths of approximately 100 m [4]. WindFloat Atlantic successfully delivers power to around 25,000 Portuguese households and avoids more than 30,000 tons of CO_2 emissions per year [4], demonstrating the viability of floating wind in Portugal's deep marine waters. This early adoption not only provides clean energy locally but also positions Portugal at the forefront of an emerging renewable technology.

Building on this early success, Portugal is actively scaling up its offshore wind ambitions, with a clear focus on floating wind. The Portuguese government has set ambitious targets for offshore wind capacity as part of its national energy strategy: about 10 GW of offshore wind by 2030 have been announced to accelerate the country's energy transition [5]. To achieve this, authorities begun delineating ocean zones for development and are preparing competitive auctions for project licenses [6]. Floating wind farms are expected to comprise the majority of this new capacity, given Portugal's deep-water sites. Crucially, the offshore wind push is not only about energy production but also industry development. The government's plan "will allow the development of an offshore renewable energy cluster in Portugal," aiming to develop a domestic industry and attract investment by creating the scale and predictability needed for a thriving supply chain [6]. This involves upgrading port infrastructure for turbine assembly, mobilizing local companies, and fostering innovation ecosystems around offshore renewables. Portuguese firms are already deeply involved – for example, the WindFloat Atlantic project was led by the joint venture Ocean Winds (EDP Renewables and ENGIE) with technology from Principle Power [6] - with several Portuguese and international developers (including EDP, Galp, and others) positioning themselves to invest in upcoming projects [6].

Portugal's unique geography has made floating wind power a strategic necessity and opportunity. The combination of abundant wind, deep coastal waters, and strong policy support provides a sustainable pathway for the country to expand its renewable energy portfolio. Investing in floating offshore wind aligns with Portugal's decarbonization commitments (carbon neutrality by 2050) and leverages its maritime heritage. It promises significant benefits: boosting energy security with home-grown clean power, reducing greenhouse gas emissions, and stimulating economic growth through high-tech industry and green jobs. These factors strongly justify continued research and investment in floating wind technology for Portugal. By advancing the analysis and design of FOWTs, this thesis contributes to that national endeavor, helping to ensure that Portugal can harness its offshore wind potential in an environmentally and economically sustainable manner.

1.5 Thesis Layout

This thesis is organised as follows. Chapter 1 introduces the context and motivation, states the objectives, and outlines the structure of the work. Chapter 2 reviews the relevant literature, covering floating offshore wind turbines and their control, the OC4 DeepCWind platform, operational modal analysis and filtering methods, key hydrodynamic concepts (including RAOs and QTFs), and wind–wave spectral characterisation. Chapter 3 describes the numerical models and inputs: the OrcaFlex elements, turbine and catenary moorings, and the two modelling strategies — *beam* and *vessel* (diffraction-based) — together with the environmental scenarios, the post-processing workflow, and the HAWC2 configuration used for comparison. Chapter 4 presents and discusses the results, beginning with baseline identification via chirp and free-decay tests, then examining the three scenarios considered, the influence of rotor harmonics (notably 3P) and mooring effects, and a comparative analysis of frequency bands and variability between models. Chapter 5 summarises the main conclusions and outlines avenues for future work.

Chapter 2

Literature Review

This chapter provides a comprehensive overview of Floating Offshore Wind Turbines (FOWTs), starting with a general introduction to wind turbine technology and progressing towards floating foundation systems. Historical developments and classification of wind turbines were reviewed and their operational principles as well as structural components were explored. The chapter then examines control systems and site-specific considerations distinguishing onshore and offshore installations. A detailed analysis of fixed-bottom foundations precedes the transition to an in-depth discussion on various floating platform types - monopiles, jackets - and four principal floating categories: barge, semi-submersible, spar, and tension-leg platforms. Emphasis is placed on the stability and dynamic characteristics of these (rigid body) platforms, including their six degrees of freedom.

2.1 Floating Offshore Wind Turbines

2.1.1 Wind Power Turbines

2.1.1.1 Classification

Historically, mankind has consistently experimented with harnessing wind power, from ships to windmills. This perpetual research eventually led to the development of the wind turbines we know today, with continuous improvements not only to the turbines themselves but also to their locations, such as the growth of offshore wind farms. Wind turbines operate on a simple principle: the wind causes the blades to rotate, and this rotational motion is transferred to the generator, which converts it into electricity. In some designs, this connection involves a gearbox to increase rotational speed, while others, known as direct-drive turbines, connect the rotor directly to the generator without a gearbox. [7].

Generally, turbines can be classified according to three indicators:

1. **Rotor's Axis Alignment**: For **Horizontal-axis wind turbines (HAWTs)**, the rotating axis is parallel to the ground. HAWTs need to be aligned with the wind direction, a more complex installation process and a large space of operation [8]. Moreover, their efficiency is larger in normal operating

conditions as well as being more suited for installation on mountain tops and offshore [8]. For **Vertical-axis wind turbines (VAWTs)**, the rotating axis is vertical, i.e, perpendicular with the ground, providing a better option for turbulent and high-speed wind conditions, where HAWTs struggle to provide reasonable efficiencies, due to its omni-directional properties [9]. However, large scale VAWTs are, currently, not economically attractive [9].

Another key difference can be observed in Figure 2.1, which highlights the difference in generator height between the two configurations, impacting accessibility. Additionally, horizontal-axis wind turbines (HAWT) are typically larger and installed at greater heights than vertical-axis wind turbines (VAWT), which allows them to harness stronger and more consistent wind speeds, contributing to their generally higher efficiency.

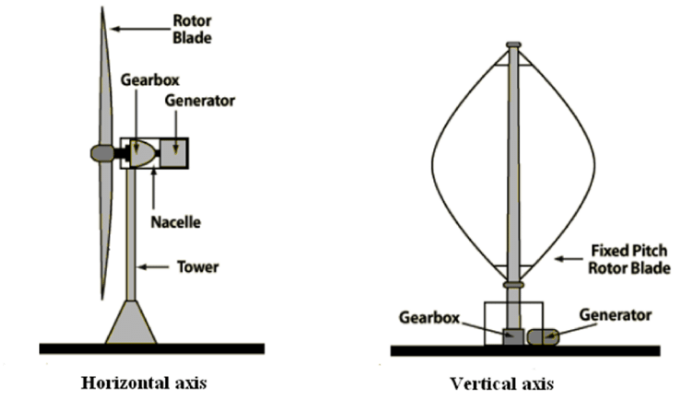

Figure 2.1: Horizontal axis (left) and Vertical axis (right) wind turbines. [10]

2. **Direction of the wind** – For **upwind turbines**, the blades face the wind direction, reducing tower shadowing effects [11]. While this design is more aerodynamically efficient, it also requires the blades to be positioned safely away from the tower and, therefore, to be as inflexible as possible, particularly for MW-class turbines [11]. For **downwind turbines**, the rotor is placed on the lee side of the turbine. In this configuration, the turbine generates slightly less power and experiences higher fatigue loads due to the shadowing effect [11]. This explains why the upwind configuration is the one most commonly used [12]. These considerations apply specifically to horizontal-axis wind turbines HAWTs. Figure 2.2 illustrates both configurations.

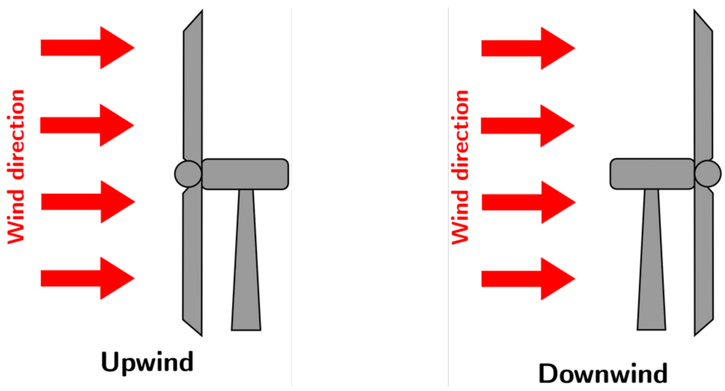

Figure 2.2: Upwind (left) and Downwind (right) configurations. Adapted from [13].

3. **Installation site** - The technology for generating electricity used by both onshore and offshore wind turbines is fundamentally identical. However, they differ in terms of their location, dimensions, scale, and methods of transmission of electricity. Simply put, **onshore** refers to turbines installed on land, while **offshore** refers to turbines installed in the sea. Figure 2.3 illustrates some variations in the dimensions and power generation of both onshore and offshore wind turbines, along with their projected developments through 2035 [14].

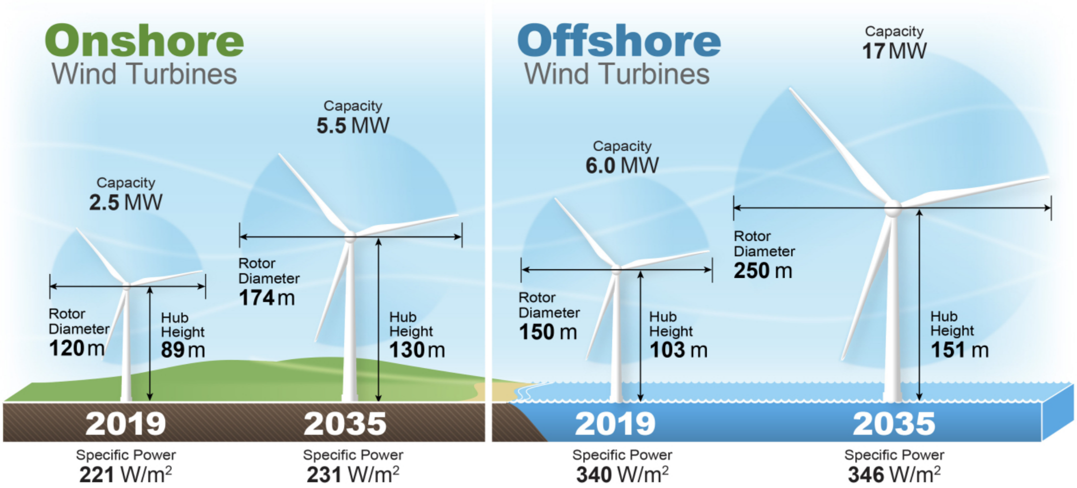

Figure 2.3: Anticipated growth in land-based and offshore wind turbine size, based on responses to a global expert survey (m: meters; W: watts) [14]

In contrast to onshore turbines, offshore wind turbines require anchoring to the seabed, necessitating sturdier support structures. Underwater cables are essential for electricity transmission, and specialised ships and equipment are required for construction and maintenance [15]. These factors contribute to an increased levelized cost of energy (LCOE), which represents the cost per unit of electricity that equalises the present value of all costs associated with the commissioning and operation of a generation plant over its expected lifetime.[16]. However, the gap in LCOE between offshore and onshore wind energy has been narrowing in recent years. In 2010, the global weighted average LCOE for onshore wind was USD 0.111 per kWh, which was 23% higher than the average cost of new fossil fuel capacity additions at USD 0.090 per kWh. By 2023, the global weighted average LCOE for new onshore wind projects had decreased to **USD 0.033 per kWh**, making it 67% lower than the average cost of fossil fuel-fired electricity, which had increased to USD 0.100 per kWh. During the same period, the global weighted average LCOE for offshore wind dropped from being 126% more expensive than the average fossil fuel cost to 25% less expensive, with costs falling from USD 0.203 per kWh to **USD 0.075 per kWh** [17].

Onshore wind energy offers several advantages. The energy harvested can be easily delivered to the grid system, and there is a large pool of professionals specialized in onshore wind energy installation [18]. Additionally, onshore wind has lower greenhouse gas (GHG) emissions over its lifetime when compared to offshore wind, primarily due to simpler installation, maintenance, and decommissioning processes [19]. Figure 2.4 illustrates the different contributions to the total emissions during the phases of the lifetime for 2 MW onshore and offshore wind turbines. It is clear that the main difference comes from the transport and installation phases. However, onshore wind power industries face challenges, such as the need for more rigorous prediction of wind conditions and speeds to maximize efficiency and stability [18]. There are also limitations on potential sites due to high land costs and possible urban expansions [18]. Furthermore, residents may express concerns regarding the visual and noise impacts of onshore wind energy installations in residential areas.

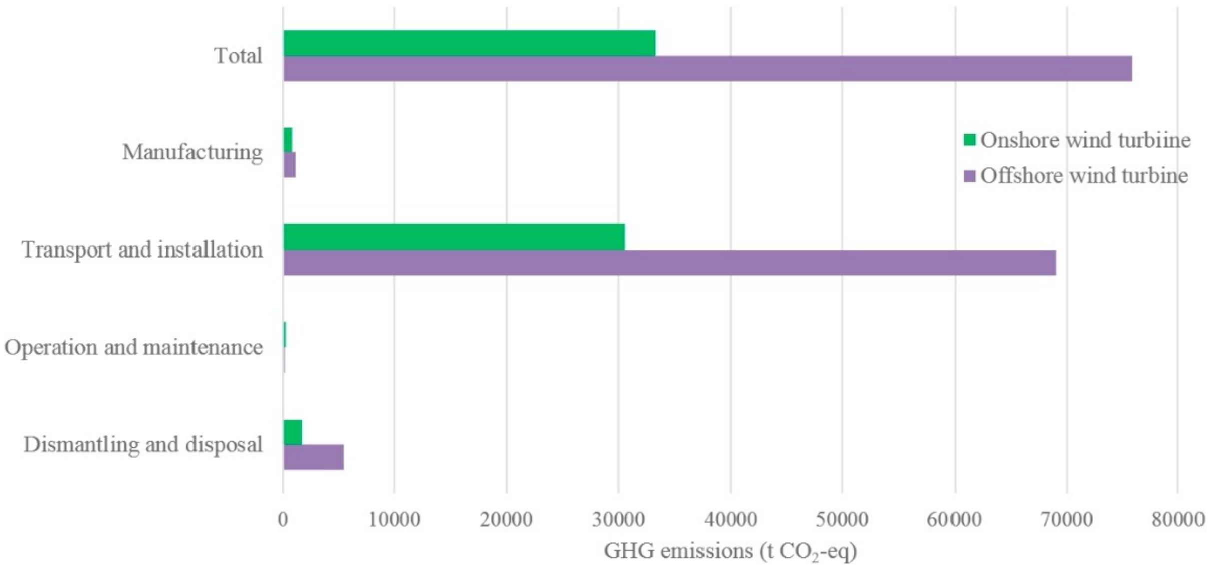

Figure 2.4: 20-year lifetime GHG emissions for 2MW onshore and offshore wind turbines [19]

Despite the higher costs and complexity of installation and maintenance, offshore wind energy provides access to vast sites suitable for multi-mega-scale generation [18]. These turbines eliminate concerns related to visual and noise impacts in humans, as these are significantly reduced offshore. Moreover, offshore locations benefit from stronger, more stable wind regimes with higher wind speeds that increase with distance from shore, and lower turbulence levels, enhancing overall energy capture efficiency [18].

However, offshore operations also introduce underwater noise, particularly during construction phases such as pile driving. According to [20], pile driving generates intense impulsive sound fields that can disrupt marine fauna, including fish and marine mammals. Measurements from a Korean offshore wind farm revealed sound exposure levels between 183–184 dB re 1 $\mu Pa^2 \cdot s$ near the source[1], high enough to potentially exceed auditory damage thresholds for various species [21]. Additionally, [22] report that aerodynamic noise from operating wind turbines can propagate underwater and intersect with the hearing ranges of marine animals, posing behavioural and ecological risks.

It is important to note that floating offshore wind platforms eliminate the need for monopile installation through pile driving. This significantly reduces the high-intensity impulsive noise associated with such activities, thereby lowering the potential for acute acoustic disturbance or injury to marine life during the construction phase.

[1] A value representing the total acoustic energy over time relative to a reference pressure-squared-time unit.

2.1.1.2 Functioning and structural composition

Most modern wind turbines feature a horizontal-axis configuration, and can usually be described as the composition of five key components: the tower, nacelle, hub, blades, and foundation. Figure 2.5 illustrates these components.

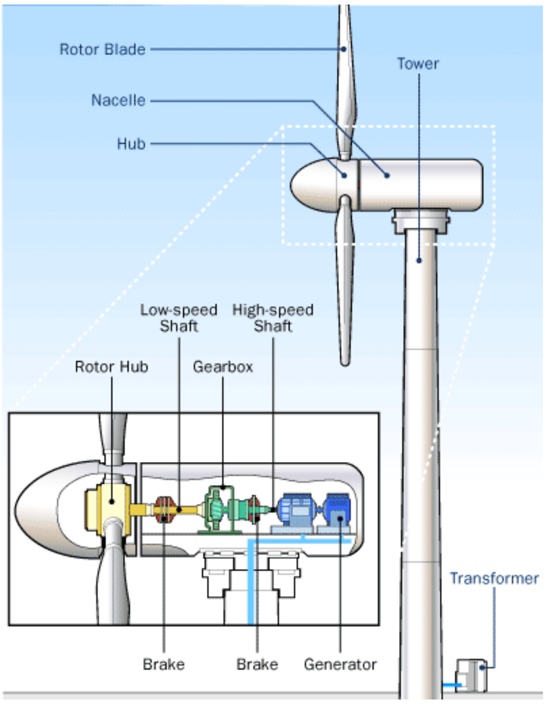

Figure 2.5: Main components of a wind turbine: tower, nacelle, hub, blades, and foundation. Adapted from [23]

The **tower** provides structural support and houses the internal wiring that transmits electrical power. Tower height is a crucial factor, as wind speeds tend to be stronger and more consistent at higher altitudes [24]. At its base, the **foundation** ensures stability, anchoring the turbine securely. Positioned, usually, at the top of the tower, the **nacelle** houses the essential mechanical and electrical components, including the generator, gearbox, and controllers [25]. The gearbox is typically needed in order to increase the rotational speed, optimising power generation efficiency [14]. The **hub**, connected to the nacelle, serves as the attachment point for the **blades**. These blades, designed with an aerodynamic profile, interact with the wind, causing the rotor to spin. This rotation drives the turbine shaft, which transfers mechanical energy to the generator [25].

The generator converts the mechanical energy into electrical energy, which is then transmitted through the wiring within the tower to a transformer or battery, ensuring the distribution of usable electricity [25]. Additionally, a braking system is incorporated within the nacelle to prevent mechanical failure caused by excessive wind speeds [25].

2.1.1.3 Control Systems

Wind is a naturally variable phenomenon, with both speed and direction fluctuating continuously. To maximise energy capture and ensure the reliable operation of wind turbines under these dynamic conditions, various control systems are implemented. These systems play a crucial role in adjusting the turbine's behaviour in real-time, optimising performance while protecting structural components from excessive loads.

The **Blade Pitch Control** system adjusts the angle of attack of the blades to optimise energy capture and regulate turbine loads. At higher wind speeds, it pitches the blades to align with the wind direction, thereby reducing aerodynamic forces and protecting the structure [14]. However, not all wind turbines rely on active pitch control. Older designs often employed a *stall regulation* strategy, where the blades were passively designed to enter stall conditions above a certain wind speed, thus limiting power output without the need for moving parts. The blade's rotation axis is shown in red in Figure 2.6. The **Yaw Control** ensures that the turbine rotates to align with the changing wind direction, maximising energy production [26]. Figure 2.6 also shows the Yaw's rotation axis in blue.

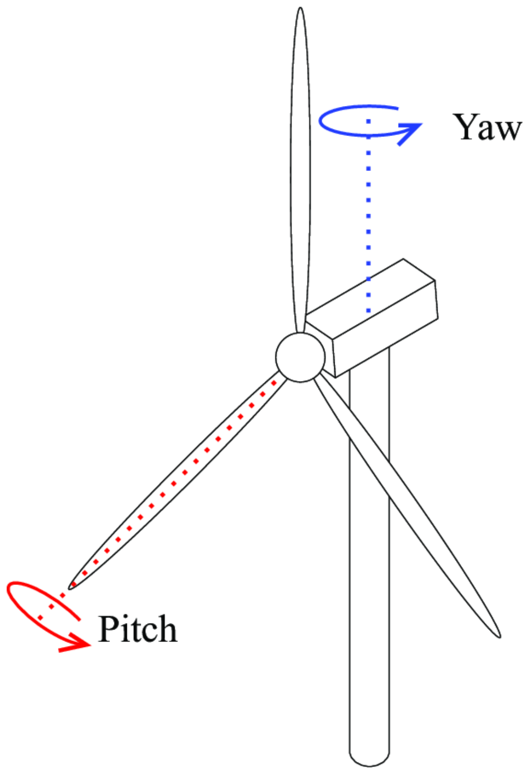

Figure 2.6: Schematic of yaw and pitch control of a wind turbine [27]

A typical control strategy for wind turbines is based on three critical wind speed thresholds [28]:

Cut-in Speed: This is the minimum wind speed at which the turbine starts operation. Below this threshold, wind energy is only used to accelerate the rotor, but no electricity is produced.

Rated Speed: This is the wind speed at which the turbine reaches its nominal power output. Beyond this speed, the generator operates at full capacity.

Cut-out Speed: This is the wind speed at which the turbine ceases operation due to excessive wind loading. It serves as a protective measure against extreme conditions.

Most pitch control systems maintain blade angles at 0°, where the rotor is able to capture the maximum possible energy from the wind, for speeds between the **Cut-in Speed** and the **Rated Speed**, meaning the turbine operates below its nominal capacity [29]. For wind speeds above the **Rated Speed** but below the **Cut-out Speed**, the pitch control system incrementally adjusts blade angles to regulate power output, ensuring it does not exceed the turbine's nominal capacity. Once wind speeds surpass the **Cut-out Speed**, most pitch control systems rotate the blades towards a feathered position, corresponding to the highest attainable pitch angles. As the pitch increases, aerodynamic thrust on the rotor decreases, which progressively reduces its rotational speed until complete stoppage is achieved. This constitutes the primary protective measure against extreme wind conditions [29].

For example, for the NREL 5-MW Reference Wind Turbine (NREL/TP-500-38060) [29], Figures 2.7 and 2.8 illustrate some of the steady-state responses during operation. Points A and B represent the power output and blade pitch for the cut-in and rated wind speeds, respectively, with the eventual cut-out speed not represented. The operating behaviour can be further described in terms of two distinct regions: the **Partial Load Control (PLC)** region and the **Full Load Control (FLC)** region. In the PLC region (from cut-in up to rated speed), the power output increases with the wind speed, while the blade pitch remains essentially fixed at 0°, maximising energy capture. In the FLC region (from rated speed up to cut-out), the turbine output is regulated to remain at its nominal capacity: this is achieved by incrementally pitching the blades, which reduces aerodynamic efficiency and stabilises the power output despite further increases in wind speed.

- *GenSpeed* represents the rotational speed of the generator (high-speed shaft).
- *RotPwr* and *GenPwr* represent the mechanical power within the rotor and the electrical output of the generator, respectively.
- *RotThrust* represents the rotor thrust.
- *RotTorq* represents the mechanical torque in the low-speed shaft.
- *RotSpeed* represents the rotational speed of the rotor (low-speed shaft).
- *BlPitch1* represents the pitch angle of Blade 1.
- *GenTq* represents the electrical torque of the generator.
- *TSR* represents the tip-speed ratio.

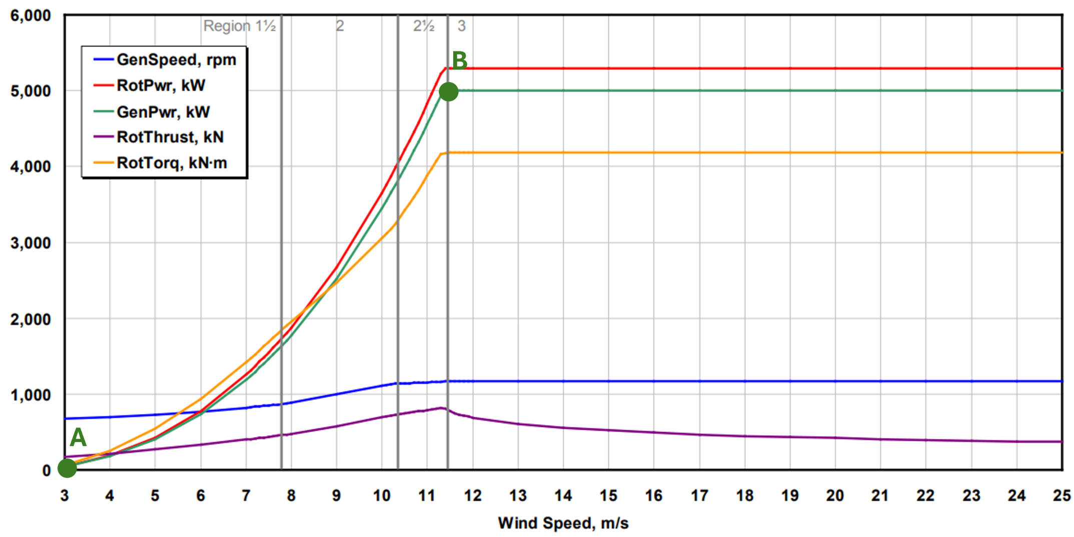

Figure 2.7: Steady-state responses as a function of wind speed (power curve). Adapted from [29]

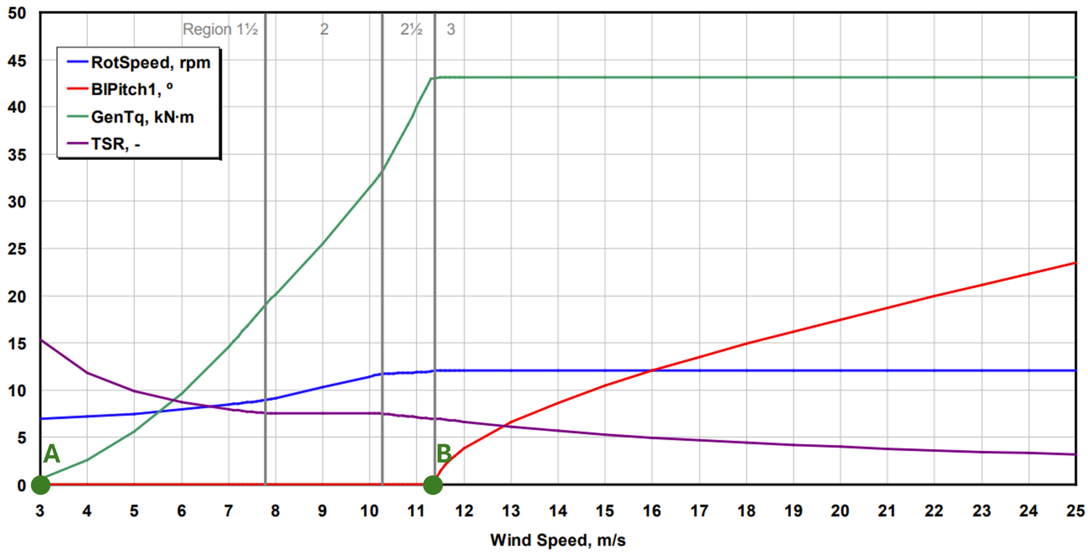

Figure 2.8: Steady-state responses as a function of wind speed. Adapted from [29]

2.1.2 Offshore Foundations

Foundations play a crucial role in offshore wind projects, as they must support the turbines while withstanding the dynamic and powerful marine environment. In fact, they account for over one-third of the total cost of these projects [30]. Selecting the appropriate foundation type is a key factor in ensuring both economic viability and structural reliability. This has become increasingly critical in recent years as wind farms are being installed further offshore, requiring optimised designs to minimise performance issues and maintenance efforts. Selecting the right foundation is ultimately a matter of balancing costs against the benefits of higher and more consistent wind speeds, as offshore winds are typically less turbulent and experience fewer obstructions. These characteristics enhance energy production, since even small increases in wind speed can lead to significantly higher power output due to the relationship between wind speed and energy generation.

This has become increasingly critical in recent years as wind farms are being installed further offshore, requiring optimised designs to minimise performance issues and maintenance efforts. Selecting the right foundation is ultimately a matter of balancing costs against the benefits of higher and more consistent wind speeds, as offshore winds are typically less turbulent and experience fewer obstructions. These characteristics enhance energy production, since even small increases in wind speed can lead to significantly higher power output due to the relationship between wind speed and energy generation.

Typically, water depth is classified into three groups: shallow waters, up to 30 metres deep; transitional waters, from 30 to 60 metres deep; and deep waters, beyond 60 metres in depth [30]. **Water depth** significantly affects installation expenses. Greater depths require more complex and specialised technologies, increasing overall investment and potentially reducing profitability [31]. However, **distance from the coast** influences both wind resource availability and infrastructure requirements. Moving wind farms further offshore allows for higher wind speeds and larger turbines while reducing visual impact [32]. It is important to note that these conditions, among others, restrict the number of suitable locations for offshore wind farms. By the end of 2018, over half of the world's offshore wind farms were located in the North Sea, with an average depth of 23.4 m [30].

There are two main types of platforms: fixed-bottom and floating foundations, both of which use the same type of turbines [33]. Over 99% of offshore wind turbines currently utilize fixed-bottom support structures, which are designed for installation in shallow waters [34]. These turbines are anchored securely to the seafloor and are typically deployed in water depths of up to 60 meters [34].

Monopile foundations, shown in Figure 2.9, are currently the most widely used due to their structural simplicity and ease of adaptation from onshore wind applications [35]. Gravity-based foundations follow in popularity and are typically deployed where seabed conditions or installation requirements favour their use [35]. Other alternatives for shallow water installations, such as *suction bucket* foundations, are under active research and development [35]. However, with the increasing deployment of larger and heavier turbines in deeper waters, **jacket-type structures**, shown in Figure 2.9 supported by multiple foundations (e.g., piles or suction caissons) have become more prominent. These multi-member lattice structures offer greater stiffness and load distribution capabilities, making them well-suited to evolving turbine scales and harsher environmental conditions [36].

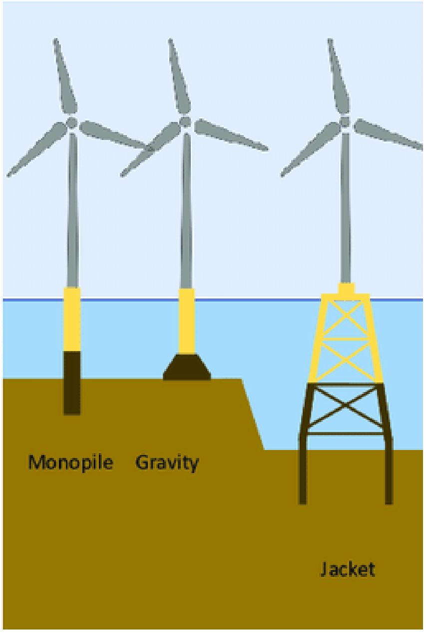

Figure 2.9: Monopile and Gravity-based fixed-bottom foundations. Adapted from [35]

A fundamental distinction between monopile and jacket-supported foundations lies in their load transfer mechanisms and resulting dynamic behaviour:

- **Monopile-supported turbines** resist external loads primarily through bending moments. The monopile itself acts as a moment-resisting foundation embedded into the seabed. The dynamic response of such systems is governed by sway bending modes, since the monopile's stiffness typically dominates the global system response [36].
- **Jacket-supported turbines**, by contrast, transfer loads mainly through axial push–pull forces along each leg. Consequently, the vertical stiffness and vertical load-bearing capacity of the sub-foundations become critical design parameters [36]. The contribution of the foundation to the system's dynamic behaviour is more strongly influenced by rocking motions, rather than sway bending, with the overall stiffness of the foundation-tower system being distributed [36].
- For axially loaded pile groups used with jackets, the ultimate axial capacity is a key concern, although deformation criteria must also be considered to ensure displacements remain within serviceability limits [36].

Fixed-bottom offshore wind technology is currently the dominant and cost-effective solution. However, as the demand for offshore wind energy increases and deeper waters are explored, floating wind turbines are being developed to harness energy from previously inaccessible regions. Floating foundations must counteract wind turbine thrust and inertial forces while minimising pitch motions for operational efficiency. Stabilisation is achieved through gravity (increasing the distance between the centre of gravity and buoyancy), water-plane (maximising pitch moment), and mooring (using mooring lines) [37]. Four main floating foundation types are used: barge, semi-submersible, spar and tension-leg platform (TLP), with selection depending on depth and seabed type, with no particular model being considered ideal uniformly [33][37].

Barge-type platforms are characterised by a shallow, wide floating structure that stabilises primarily through water-plane effects. They do not require deep docks or specialised towing equipment and can be constructed onshore or in dry docks. Fully equipped platforms can be transported with drafts below 10 m. Barge foundations enhance stability by increasing the water-plane area away from the centre of gravity, and additional stability can be achieved by incorporating ballast systems. Despite their advantages, barge platforms have a large seabed footprint, are more difficult to manufacture than Spar designs, and experience larger heave motions, which can impact operational performance.

Semi-submersible platforms (Semi-sub) consist of multiple vertical cylinders arranged in a triangular configuration, connected by submerged pontoons and exhibit similar characteristics to barge platforms. They also rely on water-plane and gravity stabilisation, with mooring lines and drag anchors ensuring positional stability. These platforms do not require deep docks or specialised equipment for towing and installation. With over 70 MW in operational capacity, Semi-sub platforms are a well-established technology. Their lower material requirements relative to Spar platforms and their ability to function across various water depths provide a significant advantage. Additionally, they offer increased deck space for maintenance. However, manufacturing complexity is greater than that of Spar platforms, and their larger heave motion and extensive seabed footprint present engineering challenges.

Spar platforms are relatively simple to manufacture and have a proven track record, with operational capacity exceeding 30 MW. Their small heave motion improves stability. However, they require deep water for operation, particularly for larger turbines, and have a large seabed footprint. Their heavy structure results in high fatigue loads at the base, while installation is complex, necessitating deep docks, sheltered areas, and large offshore cranes. Furthermore, Spar platforms exhibit larger pitch and roll motions compared to other designs and have limited deck space for maintenance.

TLPs are characterised by their small heave and pitch motions, a compact seabed footprint, and suitability for various water depths. Their lightweight structure leads to reduced material costs. However, installation challenges arise due to their instability during towing, requiring specialised vessels. The high cost of mooring lines and anchors, combined with potential catastrophic failure if a mooring line breaks, further complicates their deployment. Additionally, TLPs have limited deck space for maintenance and are not well-suited to areas with large tidal ranges. The technology readiness level (TRL) remains low for floating offshore wind turbine (FOWT) applications.

Figure 2.10 illustrates these four different types of offshore foundations.

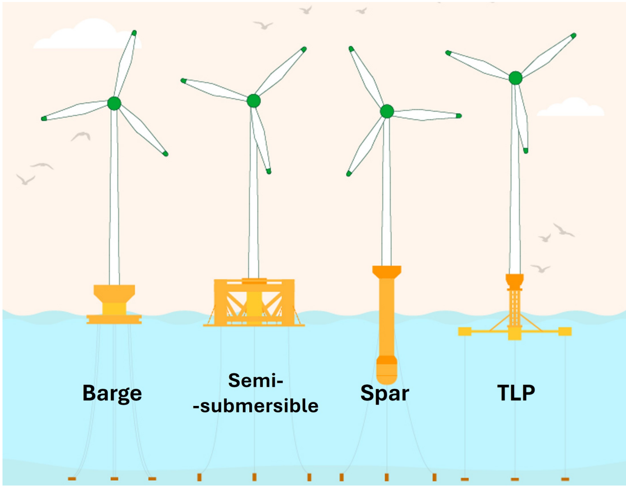

Figure 2.10: Different types of floating platforms for wind turbines. Adapted from [38]

In contrast to fixed-bottom turbines, floating turbines have six additional degrees of freedom associated with the translations and rotations of the foundation. Figure 2.11 is presented to illustrate each of these.

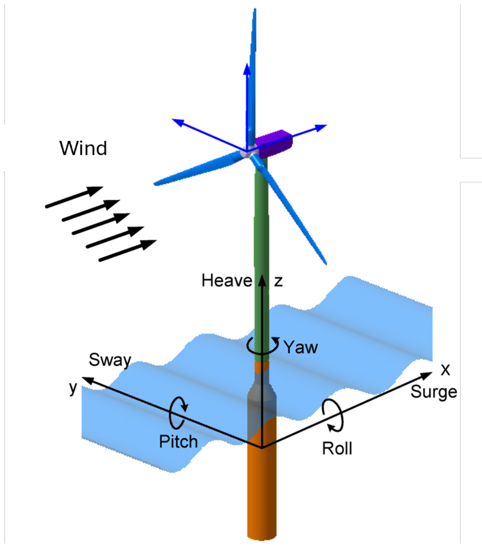

Figure 2.11: Degrees of freedom for a floating offshore wind turbine platform. Adapted from [39]

2.1.3 DeepCWind Semisubmersible Platform

The semisubmersible platform analysed in this dissertation is based on the DeepCWind foundation design. This structure was developed by the DeepCWind consortium, a research group led by the University of Maine and funded by the U.S. Department of Energy. The consortium aimed to advance the maturity of floating offshore wind technologies, with the long-term goal of installing 5 GW of floating wind capacity off the coast of Maine, United States [40]. The project brought together universities, research institutes, industry partners, and non-profit organisations.

Within this initiative, several prototype concepts were developed and tested both in wave tanks and offshore environments. One of these concepts, the DeepCWind semisubmersible, was selected for the analysis in this dissertation. In September 2014, the National Renewable Energy Laboratory (NREL) published the report "Definition of the Semisubmersible Floating System for Phase II of OC4" [41], which formally documented the structure's specifications. As part of Phase II of the OC4 (Offshore Code Comparison Collaboration, Continuation) project, the DeepCWind platform was numerically modelled to generate benchmark test data for validating floating offshore wind turbine simulation tools. The platform was designed to support the NREL 5-MW reference turbine and has become a widely adopted benchmark in the offshore wind research community. Full properties regarding the turbine can be found in [29]. Its performance under a range of environmental conditions has contributed significantly to the understanding of floating platform dynamics and the accuracy of various numerical modelling approaches. Figure 2.12 shows a computer designed representation of the DeepCWind platform in operation with a wind turbine installed.

Figure 2.12: DeepCWind Semisubmersible Platform

The platform consists of three columns arranged in an equilateral triangle, providing stability and buoyancy. Each of these columns is composed of two parts: the upper column and the lower column. The lower columns, which have significantly larger diameters compared to the upper columns, are designed to resist heave motion due to the high hydrodynamic drag created by their geometry. This additional resistance improves the motion performance of the floating foundation and provides significantly greater damping for pitch, roll, and heave motions.

The upper and lower columns are separated by a plate, allowing ballast to be placed in both sections and adjusted independently. This design enables precise tuning of the platform's centre of mass location. At the centre of the equilateral triangle is the main column, which serves as the base for the wind turbine. All columns are interconnected by slender members, arranged either horizontally or in a crossed configuration.

The foundation is held in position within a defined perimeter by three catenary mooring lines, each set at an angle of 120° and attached to one of the base columns. This type of mooring system is typically pre-installed by dragging anchors into place.

2.1.3.1 Stability under Environmental Loading

Ensuring stability under wind and wave loads is critical for floating turbines, as excessive platform motions directly affect safety and power production [42]. Hydrodynamic analyses of the OC4 DeepCWind platform show that its natural response is dominated by low-frequency, large-amplitude modes. For example, CFD simulations reveal that the platform's Response Amplitude Operators (RAOs)[2] increase sharply at long-wave periods: low-frequency waves induce notably large heave and pitch motions, whereas high-frequency (short-period) waves have relatively minor effects [43].

Key factors affecting stability have been identified in the literature:

- **Wave motion sensitivity:** The DeepCWind semisubmersible's hydrodynamic performance is highly sensitive to long waves. The calculated RAO peaks in heave and pitch grow rapidly as wave period increases [43].This implies that the platform can experience disproportionately large motions under low-frequency sea states, making resonance avoidance a design priority.
- **Center-of-gravity height:** Studies show that reducing the platform's CG height raises its natural frequencies and shrinking pitch amplitudes [43]. With a lower CG, the metacentric restoring effect is stronger, and simulations confirm smaller pitch excursions. Designers can thus enhance stability by careful mass distribution and ballast configuration.
- **Mooring redundancy:** The three-leg catenary mooring system is crucial to station-keeping. Time-domain simulations of the OC4 platform indicate that failure of even one mooring line causes sudden large horizontal drift and sharply increased tension in the remaining lines [43]. This highlights that adequate mooring redundancy and layout are essential: when one line breaks, the unbalanced restoring force allows abrupt surging, so all lines must be robust against overload.
- **Design optimizations:** Recent studies have examined geometric modifications to suppress motions. For instance, Zhao et al. (2024) proposed a novel "small-diameter" semi-submersible and found in both frequency-domain simulations and wave-tank tests that it yields lower RAOs in heave and pitch compared to OC4-DeepCWind [42]. In their analysis, the optimized platform avoided regions of high wave energy and low-frequency resonance, resulting in improved motion stability. Their experiments confirmed that the new design exhibited smaller heave/pitch motions under combined wind-wave loading than the benchmark DeepCWind model.

[2] RAOs, discussed in detail in Section 2.3.1, quantify the relationship between incident wave excitation and the resulting platform motions, and are a standard parameter for hydrodynamic characterisation of floating structures.

- **Seismic load effects:** In earthquake-prone regions, seismic excitation can be a critical load case for floating platforms. Yu et al. [44] investigated the 5-MW OC4 semisubmersible under multidirectional seismic motions using ABAQUS finite-element analysis. They found that long-period ground motions induced significant structural responses, while high-frequency motions had comparatively smaller effects. Vertical shaking, in particular, caused notable acceleration amplification at the nacelle, highlighting the importance of considering seismic effects in offshore wind turbine design. Although seismic waves do not act directly on the turbine, their energy can be transmitted through the seabed into the mooring system and surrounding water, which in turn excites the floating platform.

The collective findings from these studies suggest the following: to maintain stable operation, the DeepCWind platform and similar semisubmersibles must be designed with sufficient restoring (through buoyancy and low CG), well-tuned hydrostatic metacentric heights, and efficient damping to reduce resonant response [42, 43]. In practice, designers verify hydrostatic stability criteria (e.g., DNV ST-0119) and compute *GZ curves* [3] to ensure adequate static stability under different ballast or loading conditions. Figure 2.13 illustrates the definition of the righting lever (GZ) for a floating body heeled to an angle ϕ, highlighting the horizontal distance between the centre of gravity and the line of action of buoyancy, which generates the restoring moment.

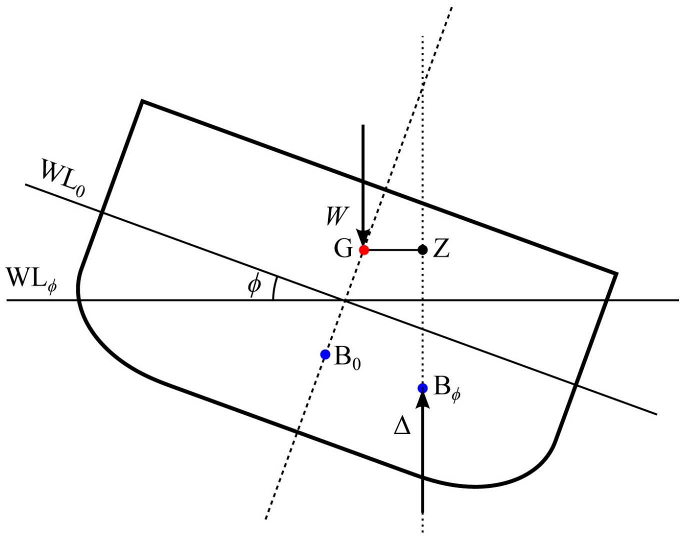

Figure 2.13: Righting lever (GZ) definition for a vessel heeled at an angle ϕ. [45]

Dynamic analyses in coupled aero-hydro-elastic tools then predict motions under combined wind–wave–current loads. For example, introducing additional viscous damping devices such as *heave plates* [4] has been shown to more accurately capture the true RAOs and to reduce peak amplitudes [42].

[3] Plots of the righting arm versus heel angle, representing the platform's ability to generate a restoring moment at various inclinations [45]

[4] Horizontal appendages fitted to the base of columns or pontoons to increase added mass and dissipate wave energy [46]

2.2 Operation Modal Analysis in Floating Wind Turbines

2.2.1 Operation Modal Analysis

Operational Modal Analysis (OMA) is used to identify the natural frequencies, mode shapes, and damping of wind turbine structures under their normal operating conditions. In contrast to traditional experimental modal analysis, OMA does not require a known external excitation, it relies only on the response measurements (output-only) from ambient loads like wind and waves [47]. This makes OMA well-suited for in-situ floating offshore wind turbines (FOWTs), where shutting down the turbine or using shakers is impractical. Researchers have applied OMA techniques to wind turbines as part of structural health monitoring [47]. Typically, accelerometers mounted at the tower top (nacelle) record the tower's fore–aft (FA) and side–side (SS) accelerations. These sensors are even mandated by standards (IEC 61400) for all commercial turbines [48].

The first tower-bending modes (FA and SS) are of particular interest; these modes usually have the largest motion at the tower top [48], making the nacelle accelerations a sensitive measure of those natural frequencies. (Higher-frequency bending modes have smaller tower-top motion, so additional sensors further down the tower are sometimes used in research campaigns [48].) For floating turbines, the overall flexible modes include the tower bending and any platform-coupled motion, but the fundamental tower FA/SS modes remain key targets for OMA identification.

In practice, authors employ both time-domain and frequency-domain identification approaches. In the time domain, advanced system identification algorithms, such as Stochastic Subspace Identification (SSI) or variants combined with techniques like the Random Decrement Technique (RDT), have been used to extract modal parameters from ambient response data [47]. Such methods can automatically estimate the modal frequencies and damping by treating the turbine as a dynamic system with unknown inputs. In the frequency domain, a more straightforward approach is to examine the spectra of measured acceleration (e.g. via FFT or power spectral density - PSD) and identify peaks corresponding to the natural frequencies (so-called "peak picking") [47]. More sophisticated frequency-domain OMA methods like Frequency Domain Decomposition (FDD) refine this by separating closely spaced modes [47]. Many studies combine these approaches, for example, using spectral peaks as initial estimates for modal frequencies, then applying a refinement algorithm in time or frequency domain.

One challenge, however, is that a wind turbine's excitation is not purely random: the rotating blades introduce deterministic periodic loads that appear as distinct frequency peaks (harmonics) in the data. Specifically, the 1P (once-per-rev) rotor frequency and its multiples (e.g. 3P for a three-bladed rotor) can dominate the excitation spectrum and lie close to the structural modes [48]. For instance, if the turbine's first tower-bending frequency is low ("soft" tower design), it may fall below or near 1P, and imbalances can cause 1P excitation of that mode [48]. More commonly, the 3P harmonic (from aerodynamic loading as each blade passes the tower and through wind shear) lies in the same frequency range as the first FA/SS modes, especially at lower wind speeds [48]. These harmonic loads complicate modal identification, since in the response spectrum a peak may correspond either to a true structural resonance or to forced vibration at a known rotor harmonic. Therefore, authors consistently note that OMA on operating wind turbines must carefully separate structural modal responses from rotor-induced harmonics.

The DNV guidelines recommend applying a 10% safety margin around the 1P and 3P frequency ranges [49]. Depending on the location of the fundamental frequency (the first bending natural frequency), f_0, relative to these excitation ranges, the structural dynamic behaviour of a wind turbine can be classified as [50]:

- **Soft–Soft**: if $f_0 < f_{1P}$, i.e. the fundamental frequency is lower than the rotor's rotational frequency;
- **Soft–Stiff**: if $f_{1P} < f_0 < f_{3P}$, i.e. the fundamental frequency lies between the 1P and 3P excitations;
- **Stiff–Stiff**: if $f_0 > f_{3P}$, i.e. the fundamental frequency is higher than the blade-passing frequency.

Figure 2.14 illustrates these frequency intervals for a three-bladed, constant-speed wind turbine, distinguishing between the soft–soft, soft–stiff, and stiff–stiff design regimes [50].

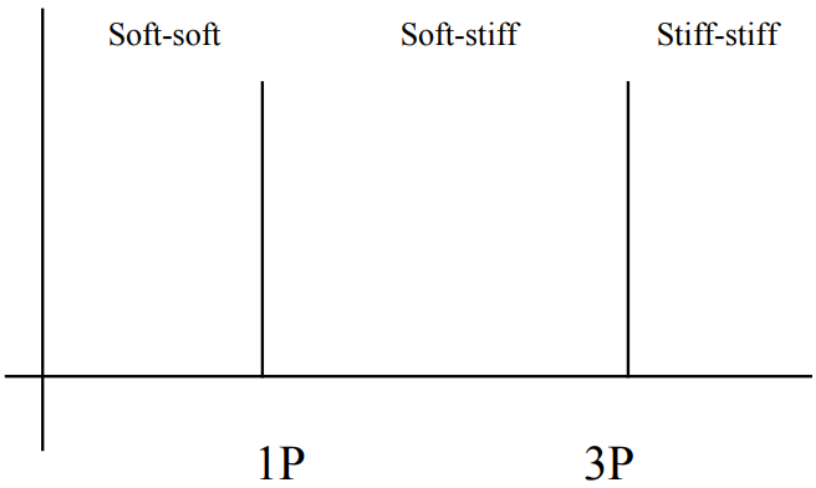

Figure 2.14: Soft–soft, soft–stiff, and stiff–stiff frequency intervals of a three-bladed, constant-speed wind turbine [50].

It is worth noting that several different OMA techniques exist, each with its own advantages and limitations. A comprehensive review of these approaches is provided by Zahid et al. [51], who compare methods such as Experimental Modal Analysis (EMA), OMA, and the more recent Impact Synchronous Modal Analysis (ISMA). The review also discusses more advanced OMA approaches based on complex frequency spectrum analysis, which allow for improved separation of closely spaced modes and better identification of damping characteristics in offshore wind turbines and other large structures.

2.2.2 Campbell Diagram

A Campbell diagram is a fundamental tool to analyze and visualize the interaction between wind turbine's natural frequencies and its rotor rotation speed [52]. It plots the system's eigenfrequency curves as a function of rotor speed, together with lines representing the rotor excitation frequencies (1P, 2P, 3P, etc.). In a Campbell diagram, the x-axis is typically the rotor speed (or corresponding 1P frequency), and the y-axis is frequency [52]. The straight lines denoted 1P, 3P, 6P, 9P, etc., indicate multiples of the rotation frequency [52], while the nearly horizontal lines represent the turbine's natural modes (which may shift slightly with centrifugal stiffening or platform effects). Resonance is predicted where a harmonic line intersects a natural frequency within the operating speed range [52]. For example, blade bending modes often intersect with 1P or 2P lines (for multi-blade rotors the blade passing frequency is nP), and tower bending modes often intersect with the 3P, 6P, etc., lines [52].

Wind turbine designers use the Campbell diagram to choose a safe margin between critical frequencies. Modern large turbines typically employ a soft–stiff design for the tower: the first tower-bending frequency is placed between 1P and 3P in the normal rpm range [53]. This avoids continuous operation exactly at resonance. The NREL 5MW reference wind turbine is an example: its first tower FA mode (around 0.32–0.34 Hz for a fixed-base) lies above the 1P line at rated speed and below the 3P line [53]. The Campbell diagram for the OC4 5MW semisubmersible FOWT (see Figure 2.15) shows the coupled first fore–aft bending mode around 0.45 Hz [52].

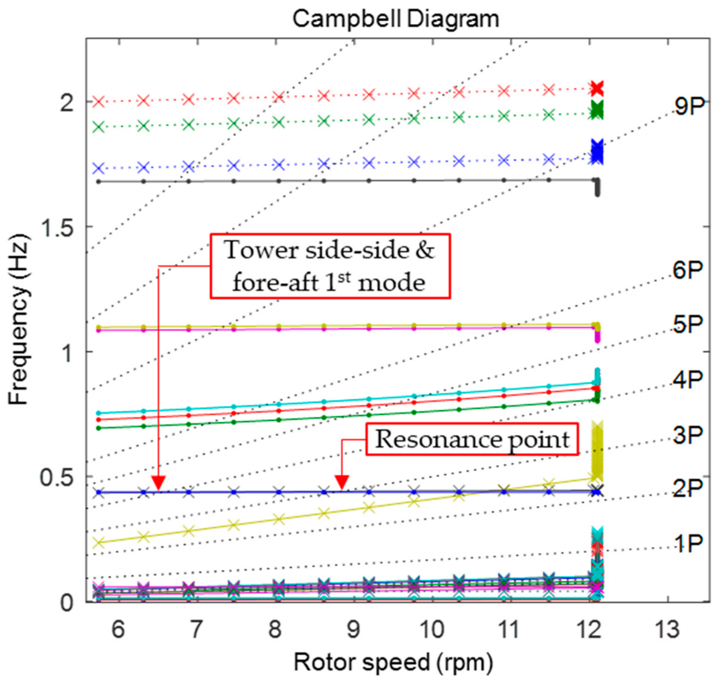

Figure 2.15: Campbell diagram for the OC4 5 MW semisubmersible showing the coupled first tower fore–aft and side–side modes across rotor speed, along with 1P–9P lines. The 3P intersection indicates a resonance point for the coupled tower–platform mode [52].

As rotor speed increases, the 3P line (which starts at 3 times the 1P frequency) will intersect this 0.40 Hz mode at a certain speed. In fact, for OC4, the 3P equals 0.40 Hz at roughly 8.8 rpm [52]. This means if the turbine were to operate steadily at around 8.8rpm (around 7.5m/s wind for that turbine), the coupled first fore–aft bending mode would be directly excited by the blade-passing frequency, leading to a resonance condition [52]. Running continuously at that speed could greatly amplify tower vibrations and fatigue. To prevent this, engineers establish exclusion zones or "no-go" speed ranges. In the OC4 case, a controller can be programmed to avoid holding the rotor at 8.8rpm, either by accelerating through it quickly or not parking the rotor at that frequency [52].

2.2.3 Filtering

Because operational data from a wind turbine contain both broadband random excitation and discrete harmonic components, filtering techniques are crucial to extracting the true modal characteristics. A common approach in literature is to apply band-pass filters to the measured acceleration signals in order to isolate the frequency band of a particular mode. By narrowing the FFT analysis to a band around the expected modal frequency, one can "focus on critical frequency ranges" and effectively eliminate the influence of unrelated dynamics such as the 3P frequency [54]. In [54], a narrow 0.3–0.5 Hz band-pass filter was applied around the first fore–aft mode (around 0.35 Hz) before performing damping identification ; this yielded more consistent and accurate estimates of the modal damping, because it removed other overlapping content (including nearby 3P noise) from the signal [54]. In general, if multiple modes or harmonics are present in the raw vibration signal, it is "recommended to filter the data using a band-pass filter to isolate the mode under test" [54]. This ensures that the subsequent analysis (whether fitting a decay curve in time domain or peak picking in frequency domain) is dominated by the single mode of interest rather than a mix of modes.

2.3 Hydrodynamic Response of a Floating Semisubmersible

A semisubmersible is a large floating platform is considered to behave as a rigid body in six degrees of freedom (6-DOF). These motion modes include three translations (surge, sway, heave) and three rotations (roll, pitch, yaw) defined with respect to the vessel's axes [55]. When waves excite a semisubmersible, it will respond in some or all of these modes depending on wave direction and frequency. The equations of motion for a floating body include contributions from hydrodynamic reaction forces, which account for fluid effects beyond the vessel's own weight and buoyancy [56]. In particular, as the semisubmersible accelerates in water, it must also accelerate some surrounding fluid, effectively increasing the system's inertia. This added inertia is quantified by the added mass coefficient (also called hydrodynamic mass), with units of mass [56]. Added mass represents the additional force required to accelerate the entrained water; it depends on the geometry of the structure and is generally frequency-dependent, meaning it varies with the oscillation frequency of the body [55, 56] (see Figure 2.16).

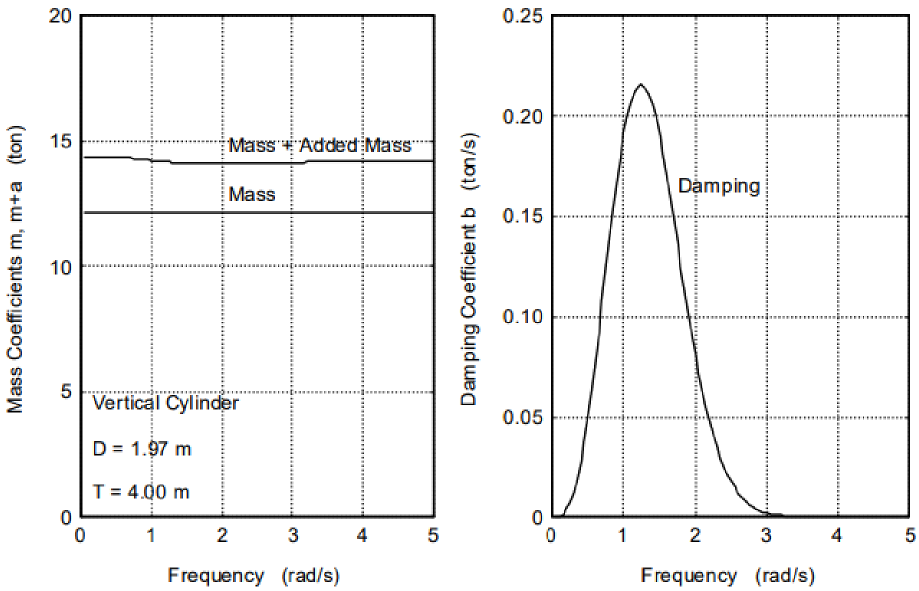

Figure 2.16: Mass and damping of a heaving vertical cylinder on a free decay test [55]

In a similar way, an oscillating semisubmersible radiates waves that carry energy away, introducing a hydrodynamic damping force proportional to the velocity [55, 56]. Both added mass and radiation damping are key components of the linear wave-induced loads on a floating body. Under typical conditions for a large offshore structure, viscous damping (from flow separation and friction) is relatively small and thus the wave radiation damping dominates the total damping at small motion amplitudes [56].[5]

2.3.1 Response Amplitude Operators (RAOs)

In linear wave theory, the response of a floating body to wave excitation can be analysed either in the time or frequency domain, since the principle of superposition applies. Any irregular sea state can be represented as a sum of harmonic components, and the system's linearity ensures that the overall response is the superposition of the individual responses. The **Response Amplitude Operator (RAO)**, however, is inherently a frequency-domain concept since it represents the transfer function linking wave input to motion output for a given degree of freedom. More precisely, the RAO is defined as the ratio of a structure's motion amplitude (in a particular mode) to the amplitude of an incident wave, as a function of wave frequency [55, 56] (see Figure 2.17).

[5] These conclusions follow the linear frequency-domain equations of motion for a floating body, $\left[\mathbf{M}+\mathbf{A}(\omega)\right]\ddot{\boldsymbol{\xi}}+\mathbf{B}(\omega)\dot{\boldsymbol{\xi}}+\mathbf{C}\boldsymbol{\xi} = \mathbf{F}_{\text{exc}}(\omega)$, where $\mathbf{A}(\omega)$ and $\mathbf{B}(\omega)$ are the added-mass and radiation-damping matrices, $\mathbf{C}$ is the hydrostatic restoring matrix, and $\mathbf{F}_{\text{exc}}$ is the wave-excitation load. A compact derivation and discussion of hydromechanical loads, wave loads, the equation of motion and RAOs is given in [55, Ch. 6, esp. §§6.3.2–6.3.5, see also §6.4 for second-order wave-drift forces]. Foundational potential-flow theory and added-mass concepts are treated in [56, Ch. 3], while linear wave–body interaction, radiation/diffraction and wave-excitation loads are developed in [56, Ch. 5].

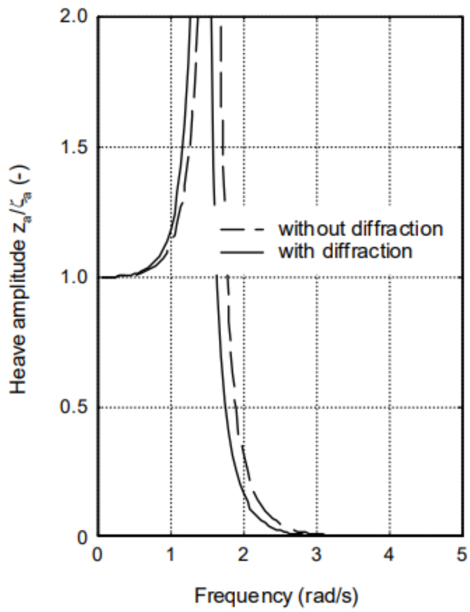

Figure 2.17: Heave RAO curve of a vertical cylinder in regular waves [55].

For each motion mode (surge, heave, pitch, etc.), an RAO curve can be obtained, typically from potential-flow simulations or experiments, describing how the semisubmersible responds to unit-amplitude waves across a range of frequencies. In the case of heave response in regular waves, Figure 2.18 shows the typical heave RAO curve for a vertical cylinder. Notably, in Figure 2.18, the label *without diffraction*[6] indicates that the wave loading is taken purely as the undisturbed pressure field acting on the wetted surface.

The heave RAO exhibits three characteristic frequency regions [55]:

- **Low-frequency region:** when the wave frequency is much smaller than the natural frequency, the vertical response is dominated by hydrostatic restoring forces. In this regime the cylinder tends to follow the incident wave profile, with the RAO approaching unity and the phase lag tending to zero.

- **Natural-frequency region:** around the body's natural period, the motion response is controlled by damping. If damping is small, a sharp resonance peak appears and the RAO reaches high values. At this point, the motion exhibits a rapid phase change of approximately π radians.

- **High-frequency region:** at wave frequencies much higher than the natural frequency, the response is controlled by the inertia term. In this regime the cylinder cannot keep up with the rapid oscillations of the incident wave, and the RAO tends toward zero. A second phase transition occurs at still higher frequencies as inertial effects dominate.

[6] In this context, "without diffraction" means that only the Froude–Krilov force is considered as the incident wave load, i.e. neglecting the additional contribution from diffracted waves. A full derivation and discussion of these hydrodynamic forces is given in [55, §6.3.5].

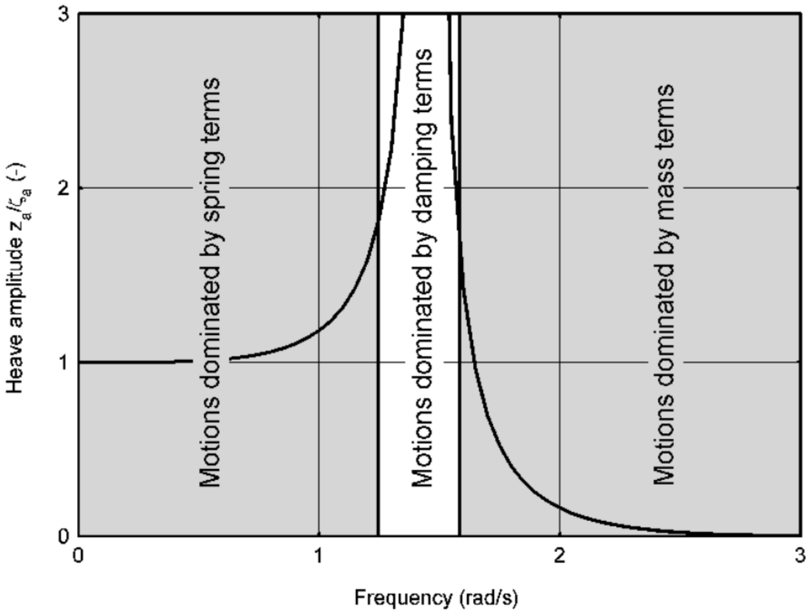

Figure 2.18: Heave RAO curve of a vertical cylinder in regular waves, showing the influence of diffraction and the three characteristic frequency regions [55].

2.3.2 Wave-Frequency vs. Low-Frequency Motions

In a real irregular sea state, a floating body is subjected to both wave-frequency motions (driven by the immediate wave oscillations) and low-frequency motions (driven by slowly-varying second-order forces). The wave-frequency motions are the direct, first-order response described by the RAOs occuring at the same frequencies as the incoming wave components [55]. In contrast, second-order hydrodynamic forces arise from nonlinear interactions of waves. These forces oscillate at frequencies different from the incident wave frequencies, specifically at combinations like the sum or difference of wave frequencies [55]. The difference-frequency components (i.e. the difference between two wave frequencies) produce forces at much lower frequencies than any individual wave. In an irregular sea, groups of waves lead to a beating effect; the resulting low-frequency force is associated with the wave group envelope frequency (the difference frequency) [55] (see Figure 2.19). These low-frequency second-order forces are commonly called wave drift forces, since they include a non-zero mean component that can push a free-floating vessel downwind/downwave over time [55].

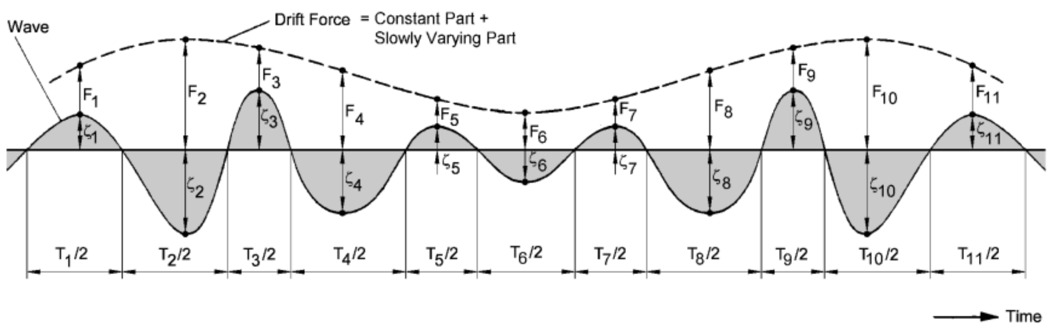

Figure 2.19: Wave Drift Forces Obtained from a Wave Record [55]. Here ζ_i denotes the crest or trough amplitude of the i-th wave, and T_i its associated period as determined by successive zero-crossings.

For a semisubmersible restrained by moorings or dynamic positioning, the drift forces manifest as a slow oscillatory motion (often in surge, sway, or yaw) around the equilibrium position. Importantly, if the wave-group (difference) frequency coincides with a natural mode of the system (such as the moored surge natural period, which is typically very low frequency), the semisubmersible can experience large slow-drift motions [55]. Remery and Hermans (1971) [57] demonstrated that when the period of wave groups equals a vessel's natural period, resonant amplification of low-frequency motion occurs [55]. In practice, this means that even if the wave frequencies themselves are far from a platform's resonance, the second-order beating can excite significant motion. By contrast, the sum-frequency second-order forces (at roughly twice the wave frequency) generally have minimal effect on a semisubmersible's horizontal motions [55]. (Sum-frequency effects can be relevant for high-frequency vertical loads or tension in stiff tether systems like TLPs, but for a conventional catenary-moored semisubmersible, they are usually negligible in the global responses [55].)

2.3.3 Quadratic Transfer Functions (QTFs)

A QTF characterizes the second-order force response due to two interacting wave components, analogous to how an RAO characterizes a linear response to a single wave frequency. In essence, the QTF is a frequency-domain mapping from a pair of wave frequencies (ω_i, ω_j) to the amplitude of the resulting second-order force at the combination frequency (sum or difference $\omega_i \pm \omega_j$). For wave drift forces (difference-frequency and mean forces), the QTF provides the magnitude of the slowly-varying force caused by every pair of wave components in a spectrum [55, 56] [7]. Using QTFs, the wave-drift force spectrum can be computed in the frequency domain by integrating over all wave frequency pairs [55, 56]. This analysis yields the low-frequency force spectrum and, ultimately, the expected slow-motion response of the semisubmersible when coupled with its mooring dynamics. In practical terms, the difference-frequency QTF (often obtained from potential flow solvers or experiments) is central to evaluating a semisubmersible's slow-drift motion and mooring loads in irregular seas [55, 56]. The term "quadratic" reflects that these forces scale with the square of wave amplitude: for instance, experiments show that slow-drift motion variance increases roughly with the square of significant wave height, consistent with quadratic wave forcing [56]. In summary, RAOs and QTFs provide a framework to decompose a semisubmersible's motion into a wave-frequency part and a low-frequency part. The wave-frequency motions are predicted by linear RAOs (first-order theory), while the low-frequency motions stem from second-order difference-frequency forces quantified by QTFs [55, 56].

2.4 Concepts relative to sea and wind conditions

In order to properly characterise the modal response of an offshore wind turbine, it is essential to understand how to represent its operating conditions accurately. For offshore structures used in wind

[7] A more detailed derivation and worked-out demonstration of QTFs, including their mathematical formulation and application to difference-frequency forces, is presented in Chapter 9.3.3 of [55]. This chapter shows how the quadratic nature arises from the second-order potential theory, and provides illustrative examples of how the transfer functions are calculated and applied in wave–structure interaction problems

energy exploitation, there are established standards that define the assumptions and approximations to be made for such characterisation. In this work, guidance was taken from the GL, DNV-GL, and IEC 61400–1/3 standards [58, 59, 60, 61], as well as recommendations found in [62]. As a starting point, it is reasonable to consider only the effects of wind, waves, and ocean currents, as these represent the dominant conditions experienced throughout the turbine's operational lifetime.

Wind and wave actions are inherently linked, as ocean waves are primarily generated by the wind. In general, the higher the wind speed, the longer its duration, and the larger the fetch area over which it blows, the greater the wave height. Therefore, wind can be considered a governing parameter, as it significantly influences the external environmental conditions acting on the offshore structure.

2.4.1 Joint Probability

As indicated by the GL and IEC 61400-3 standards [58, 61], the analysis must consider the external conditions specific to the installation site. Therefore, access to temporal wind and sea state data is required to carry out the intended structural analysis.

The concept of significant wave height (H_s) is introduced, referring to the average of the highest one-third of wave heights within a given time interval. The significant wave height is dependent on the mean wind speed ($\overline{u}_v$), and in order to perform the necessary simulations, it is essential to define how these two parameters relate.

The Joint Probability Distribution describes the statistical dependence between wave height and wind speed. This relationship allows the calculation of the Conditional Expected Value, represented in this case as $E[H_s \mid \overline{u}_v]$, i.e., the expected value of the wave height given a specific wind speed. Similarly, the concept can be extended to the wave peak period (T_p), yielding $E[T_p \mid \overline{u}_v]$.

A comprehensive description of the employed methodology is provided in [63]. It is also important to note that the sea state is influenced not just by the instantaneous wind speed but also by its history over the preceding days. This cumulative effect arises because wave formation depends on factors such as wind fetch[8] and duration, which integrate the wind's past behavior, and because wind energy is gradually transferred into the wave field over time, propagating through the water column and building the sea state [65].

2.4.2 Wind Field Characterisation and Turbulence Modelling

The incident wind acting on a wind turbine can be decomposed into three components: longitudinal (u_v), lateral (v_v), and vertical (w_v), aligned with the x, y, and z axes, respectively. These axes correspond to those illustrated in Figure 2.11. Among these, the longitudinal component is the most relevant for evaluating aerodynamic loads and structural response.

[8] The uninterrupted distance over which the wind blows in a constant direction across the water surface, thereby allowing energy to accumulate and transfer to the wave field [64]

The longitudinal wind speed is defined as:

$$u_v(t) = \overline{u}_v + u'_v(t) \tag{2.1}$$

where $\overline{u}_v$ is the mean wind speed and $u'_v(t)$ represents its turbulent component.

If the known wind speed data is given at a different height from the rotor centre (z), it must be converted using the Power Law [66, 67]:

$$\overline{u}_v(z) = \overline{u}_v(z_{\text{ref}}) \left(\frac{z}{z_{\text{ref}}} \right)^{\alpha} \tag{2.2}$$

where α is the shear exponent, z_{ref} is the reference measurement height, and z is the rotor centre height.

The turbulent component $u'_v(t)$ is modelled using spectral density functions. According to the IEC 61400 standard, the Von Karman and Kaimal spectra are the most commonly used. The Kaimal spectrum, which better represents atmospheric turbulence, is adopted in this work and defined as:

$$S_{\text{kaimal}}(f) = \frac{4\sigma_{u_v}^2 \dfrac{L_{u_v}}{\overline{u}_v}}{\left(1 + 6f \dfrac{L_{u_v}}{\overline{u}_v}\right)^{5/3}} \tag{2.3}$$

where σ_{u_v} is the standard deviation of turbulence (depending on the selected turbulence level, as defined in Section 6.3.1.3 of IEC 61400-1 [60]), L_{u_v} is the integral length scale (defined in Section 6.3(b) of [60]), and f is the frequency.

Recent studies have shown that the mixing length l, a parameter from classical boundary layer theory, exhibits a near-linear relationship with the turbulence length scale λ_m derived from the vertical velocity spectrum [68]. In particular, measurements from Høvsøre (Denmark) suggest that:

$$\lambda_m \approx 7l \tag{2.4}$$

This relationship holds for most heights and stability conditions, with minor deviations under highly unstable conditions and above 100 m due to reduced local wind shear [68]. These findings support the continued use of integral length scales in wind modelling, especially in the height range relevant to offshore wind turbines.

2.4.3 Wave Kinematics through Frequency Spectra

Given the inherent randomness of sea waves, wave parameters required for simulations are commonly defined using frequency density spectra grounded in probabilistic methods. Wave spectra, denoted as $S(f)$ or $S(\omega)$, can be described using various empirical formulations, including those proposed by Scott, Torsethaugen, Pierson–Moskowitz, Bretschneider, and Ochi–Hubble, among others [69]. The standards GL, DNV-GL, and IEC 61400-3 [58, 59, 61] recommend the use of the Pierson-Moskowitz and JONSWAP (Joint North Sea Wave Observation Project) spectra.

The key distinction between these two models lies in the assumed development stage of the sea state. The Pierson-Moskowitz spectrum is based on a fully developed sea, where a balance is achieved between the energy input from the wind and the dissipation by wave breaking, resulting in a steady-state wave energy distribution [70]. In contrast, the JONSWAP spectrum accounts for a fetch-limited sea where this balance has not yet been reached, and wave growth continues either spatially or temporally [70].

Practically, the JONSWAP spectrum extends the Pierson-Moskowitz formulation by introducing a peak enhancement factor γ, which accentuates the spectral peak. When $\gamma = 1$, the JONSWAP spectrum simplifies to the Pierson-Moskowitz model, making them equivalent under such conditions [69]. Compared to the Modified Pierson-Moskowitz (also known as Bretschneider) spectrum, the JONSWAP formulation presents a sharper spectral peak, better capturing the characteristics of evolving sea states, as shown in Figure 2.20.

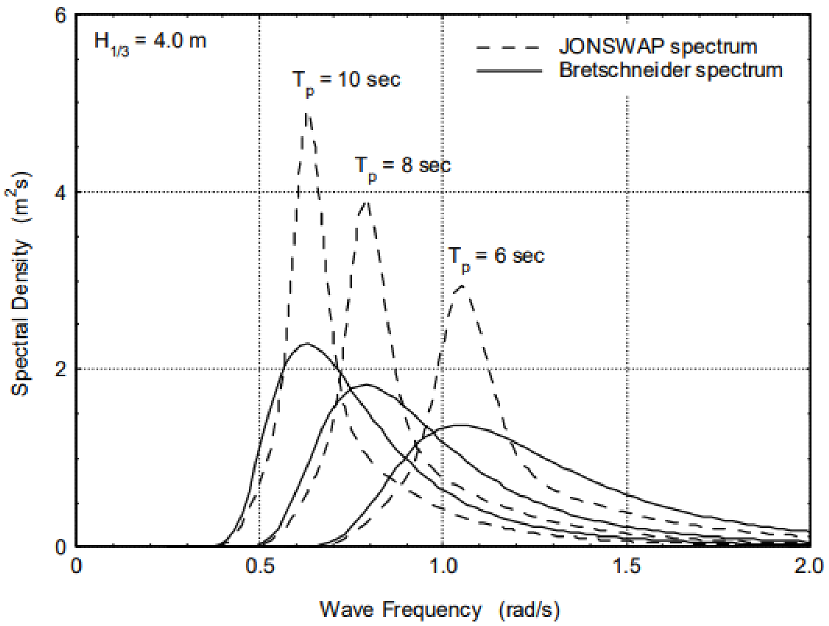

Figure 2.20: Comparison of Spectral Formulations [55]

Equations 2.6 and 2.7 give the Pierson–Moskowitz (PM) and JONSWAP spectra in standard form [55, 59]. Both describe the one–sided variance density spectrum $S(f)$ [$\mathrm{m^2 s}$] as a function of frequency f [Hz]. The PM spectrum represents a fully developed sea, while JONSWAP augments PM with a peak–enhancement factor γ and a frequency–dependent peak-shape function $b(f)$ to represent fetch and duration–limited growth.

Pierson–Moskowitz (PM) A common PM normalisation uses the dimensional constant α_{PM}:

$$S_{\mathrm{PM}}(f) = \alpha_{\mathrm{PM}} \frac{g^2}{(2\pi)^4} f^{-5} \exp\left[-\frac{5}{4}\left(\frac{f_p}{f}\right)^4\right], \tag{2.5}$$

where g is gravitational acceleration and f_p is the peak frequency. An equivalent form, normalised by significant wave height H_s, is

$$S_{\mathrm{PM}}(f) = \frac{5}{16} H_s^2 f_p^4 f^{-5} \exp\left[-\frac{5}{4}\left(\frac{f_p}{f}\right)^4\right]. \tag{2.6}$$

(Here f_p is often denoted f_m in the literature; we take $f_p \equiv f_m$.)

JONSWAP The JONSWAP spectrum enhances PM around f_p using γ and the peak–shape function $b(f)$:

$$S_{\mathrm{JON}}(f) = \alpha_{\mathrm{J}} \frac{g^2}{(2\pi)^4} f^{-5} \exp\left[-\frac{5}{4}\left(\frac{f_p}{f}\right)^4\right] \gamma^{b(f)}, \tag{2.7}$$

with

$$b(f) = \exp\left[-\frac{1}{2\sigma^2}\left(\frac{f}{f_p} - 1\right)^2\right], \qquad \sigma = \begin{cases} \sigma_1, & f \le f_p, \\ \sigma_2, & f > f_p, \end{cases} \tag{2.8}$$

where σ_1 and σ_2 are spectral width parameters (typically $\sigma_1 \approx 0.07$, $\sigma_2 \approx 0.09$ in DNV-GL).

Note on normalisation. The choice of the front–factor (scale) in (2.5)–(2.7) is addressed in Appendix A.1, where the spectra are normalised so that the zeroth spectral moment satisfies $m_0 = H_s^2/16$ [59, 55, 71, 72].

2.4.3.1 Wave Kinematics Using Airy Theory

The Airy wave theory, also referred to as linear wave theory, is adopted to model the kinematics of surface waves. This linear approach assumes that wave amplitudes are small relative to both the wavelength and the water depth, which permits the linearisation of the otherwise nonlinear free-surface boundary conditions. Under these conditions, the theory is valid for deep water waves and for small-amplitude waves in shallow water. Although higher-order wave kinematics may be necessary for extreme wave conditions or shallow water propagation, these effects are not considered within the scope of this work [55, 62].

Consider a single-frequency (monochromatic) progressive wave propagating over still water, described by the following surface elevation [73]:

$$\eta(x,t) = A\cos(kx - \omega t) \tag{2.9}$$

The amplitude A is defined as the maximum displacement from the still water level (SWL). The wave height H is the vertical distance between a crest and the adjacent trough. For sinusoidal waves, the relationship between amplitude and wave height is [73]:

$$H = 2A \tag{2.10}$$

In the case of non-sinusoidal waves, wave height H is generally easier to define and measure directly.

The wavenumber k determines the spatial frequency of the wave. A full wave cycle occurs when the product kx changes by 2π. Thus, the wavelength L is given by [73]:

$$L = \frac{2\pi}{k} \tag{2.11}$$

The angular frequency ω defines the temporal frequency of the wave. A complete wave cycle in time occurs when ωt changes by 2π [73]. Therefore, the wave period T is:

$$T = \frac{2\pi}{\omega} \tag{2.12}$$

The wave frequency f, measured in Hertz (Hz), is the reciprocal of the period:

$$f = \frac{1}{T} = \frac{\omega}{2\pi} \tag{2.13}$$

Figure 2.21 displays a schematic representation of the relevant wave parameters.

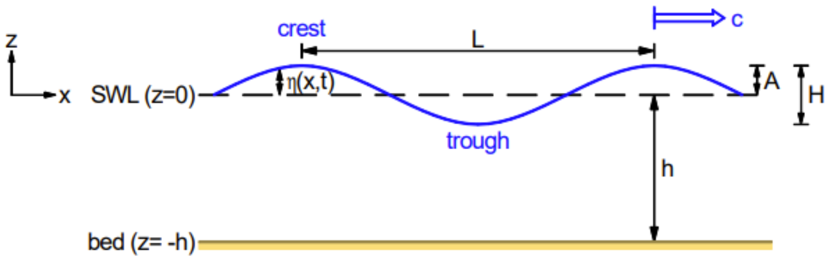

Figure 2.21: Main wave parameters, where c denotes the wave speed [73].

Further details on this methodology, particularly for the modelling of random waves under different frequency spectra, can be found in the OrcaFlex wave theory documentation [74].

2.4.4 Wind-Generated Currents

In this dissertation, only wind-generated currents are considered, as they typically have the greatest influence on floating platform loads due to their alignment with extreme wind and wave conditions, their concentration near the surface where most hydrodynamic forces act [59] and due to the lack of available data for other current sources at the location under study. Ocean currents can generally be divided into surface and sub-surface currents. The total current velocity profile $u_c(z)$, as defined in Equation 2.14, is a function of the vertical distance z from the still water level (positive upwards) and is the sum of the surface and sub-surface current velocities [58]:

$$u_c(z) = u_{c,\text{sub}}(z) + u_{c,\text{wind}}(z) \tag{2.14}$$

Since only wind-driven surface currents are considered, Equation 2.14 simplifies to the second term alone. According to IEC 61400-3, the vertical distribution of the wind-driven current velocity $u_{c,\text{wind}}(z)$

follows a linear profile, expressed by Equation 2.15. This profile linearly decreases with depth from the water surface down to a reference depth z_{ref}, typically set to 20 m:

$$u_{c,\text{wind}}(z) = \begin{cases} u_{c,\text{wind}} \cdot \left(\frac{z_{\text{ref}}+z}{z_{\text{ref}}}\right), & z \in [-z_{\text{ref}}, 0] \\ 0, & \text{otherwise} \end{cases} \tag{2.15}$$

The surface wind current velocity $u_{c,\text{wind}}$ is calculated based on the 1-hour averaged wind speed at 10 m height above sea level, $\overline{u}_v(10\,\text{m}, 1\text{ hour})$, using the empirical relationship provided in IEC 61400-3 (Equation 2.16) [61]:

$$u_{c,\text{wind}} = 0.015 \cdot \overline{u}_v(10\,\text{m}, 1\text{ hour}) \tag{2.16}$$

A visual representation of the seawater current profile corresponding to a reference wind speed of $u_v(10\,\text{m}, 1\text{ hour}) = 10$ m/s is presented in Figure 2.22, following the linear variation described by Equation 2.15.

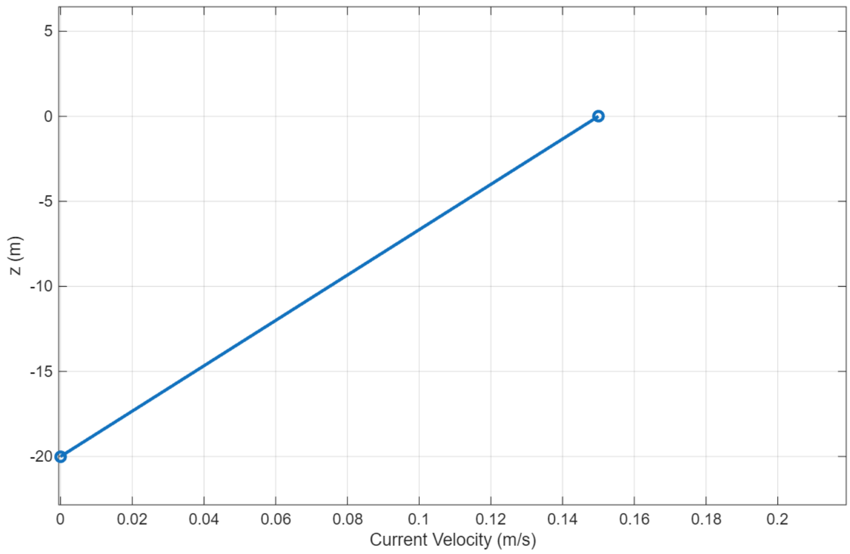

Figure 2.22: Seawater Current Profile for a $\overline{u}_v(10\,\text{m}, 1\text{ hour}) = 10\ m/s$

In some studies a power law is used for the near-surface shear [59, 75]. The wind-driven current in the top layer is written as

$$u_{c,\text{wind}}(z) = \begin{cases} u_{c,\text{wind}} \cdot \left(\dfrac{z_{\text{ref}}+z}{z_{\text{ref}}}\right)^{\alpha}, & z \in [-z_{\text{ref}}, 0], \\ 0, & \text{otherwise,} \end{cases} \tag{2.17}$$

where $u_{c,\text{wind}}$ is the surface value from Equation 2.16 and α is a dimensionless shear exponent. Setting $\alpha = 1$ recovers the IEC linear profile; $\alpha < 1$ gives slower decay; $\alpha > 1$ gives faster decay. The exponent is chosen by calibration to local measurements.

Chapter 3

Numerical Models

This chapter presents the numerical models developed for the analysis. It begins by outlining the fundamental elements adopted in the simulations and the theoretical principles underlying their formulation. The modelling approaches employed are then described in detail, including the assumptions, simplifications, and parameter selections guiding their implementation. This framework provides the basis for the subsequent evaluation of the system behaviour under the defined operating conditions.

3.1 OrcaFlex Elements

This section describes the elements employed within OrcaFlex to represent the components of the system. The formulation, properties, and discretisation of each element type are outlined, highlighting their role in accurately modelling the physical behaviour of the floating platform and its mooring system.

3.1.1 Introduction to Morison's equation

To compute hydrodynamic forces acting on submerged bodies, OrcaFlex adopts an extended formulation of Morison's equation. This empirical model was originally proposed in [76] to estimate wave-induced forces on slender, fixed vertical cylinders. The equation decomposes the total fluid force per unit length into two components: one proportional to the local fluid acceleration, referred to as the inertia force, and another proportional to the relative fluid velocity, known as the drag force.

The classical form of Morison's equation is:

$$\mathbf{f} = C_m \Delta \mathbf{a}_f + \frac{1}{2}\rho C_d A |\mathbf{v}_f| \mathbf{v}_f, \tag{3.1}$$

where:

- $\mathbf{f}$ is the hydrodynamic force per unit length,

- $\mathbf{C}_m$ is the inertia coefficient, which includes both the Froude–Krylov contribution and the added mass effect,
- Δ represents the displaced fluid mass per unit length,
- $\mathbf{a}_f$ is the fluid acceleration (in an Earth-fixed frame),
- ρ is the fluid density,
- C_d is the drag coefficient,
- A is the projected area for drag calculations,
- $\mathbf{v}_f$ is the fluid velocity (in an Earth-fixed frame).

The remainder of this subsection is based on the OrcaFlex documentation [77], which outlines how Morison's theory is implemented within the software environment.

When applied to a moving body, the formulation must account for the body's motion. The inertia term is then modified by subtracting a contribution related to the body's acceleration, and the drag force is computed using the velocity relative to the body:

$$\mathbf{f} = \left(C_m \Delta \mathbf{a}_f - C_a \Delta \mathbf{a}_b\right) + \frac{1}{2}\rho C_d A |\mathbf{v}_r| \mathbf{v}_r, \tag{3.2}$$

where:

- C_a is the added mass coefficient, representing the extra fluid mass that effectively accelerates with the body,
- $\mathbf{a}_b$ is the acceleration of the body (Earth-fixed),
- $\mathbf{v}_r$ is the velocity of the fluid relative to the body.

Note: The subtraction of the added mass term arises because the relative fluid acceleration is reduced by the body's own acceleration; this does not violate the concept of added mass, which still represents the extra inertia experienced by the body due to the surrounding fluid.

A common simplification assumes $C_m = 1 + C_a$, yielding:

$$\mathbf{f} = \left(\Delta \mathbf{a}_f + C_a \Delta \mathbf{a}_r\right) + \frac{1}{2}\rho C_d A |\mathbf{v}_r| \mathbf{v}_r, \tag{3.3}$$

where $\mathbf{a}_r = \mathbf{a}_f - \mathbf{a}_b$ denotes the relative fluid acceleration.

In this formulation, the inertia force encompasses both the *Froude-Krylov* component (associated with the undisturbed wave pressure field acting on the displaced volume) and the *added mass* component (arising from the acceleration of the surrounding fluid due to the presence of the body). The drag force dominates when relative velocity is high.

Regarding the energetic interpretation of added mass, an accelerating body moving through a stationary fluid requires not only the kinetic energy of the body itself but also additional energy to accelerate the surrounding fluid This is expressed as:

$$\mathbf{f}_b = (m + C_a \Delta)\mathbf{a}_b, \tag{3.4}$$

where both m and Δ must be expressed in the same units (either total mass or mass per unit length). Here, m is the mass of the body, and $\mathbf{f}_b$ is the total force required to accelerate the body including the effect of added mass.

This hydrodynamic model underpins the computation of wave-induced forces on lines and floating bodies such as 3D and 6D buoys within OrcaFlex.

3.1.2 Line elements

According to the OrcaFlex Manual [74], the line element is discretised into straight, massless model segments connected by nodes, which are numbered sequentially from end A to end B. The formulation corresponds more closely to a rod element with lumped bending properties at the nodes, rather than to a continuous beam element, since bending stiffness is not distributed along the segment length. Each segment represents only the axial and torsional stiffness of the line, while all other physical properties (mass, weight, buoyancy, drag) are concentrated at the nodes, as illustrated in Figure 3.1.

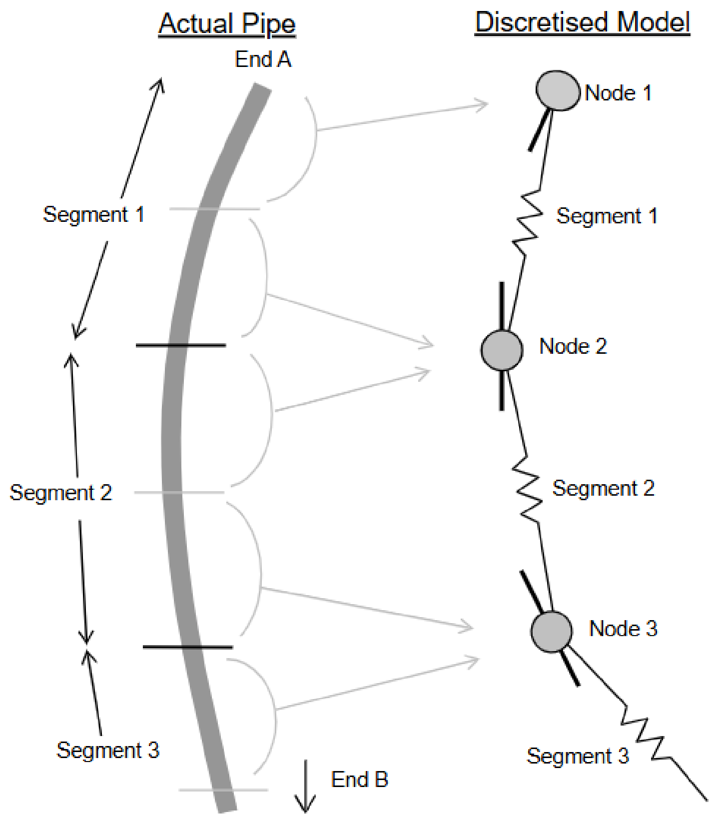

Figure 3.1: OrcaFlex line element [78]

Nodes represent the midpoints between adjacent segments and carry the lumped properties of the surrounding half-segments. End nodes, having only one adjacent segment, represent a single half-segment. External forces and moments act on the nodes, with fluid-related forces (such as buoyancy, added mass, and drag) accounting for the instantaneous wetted length when segments intersect the free surface.

Model segments behave as co-axial telescoping rods connected via axial and torsional spring-dampers. Bending is represented by rotational spring-dampers at each end of the segment, allowing for independent stiffness values in orthogonal bending planes [78].

3.1.3 6D Buoys

6D buoys in OrcaFlex are rigid bodies with six degrees of freedom: three translational and three rotational. They are primarily used in the drag/inertia regime where Morison's equation applies, assuming the buoy diameter is small relative to the wavelength. In cases where diffraction effects dominate, a vessel object may be more appropriate. It is also possible to define buoys with negligible properties.

These buoys account for mass and moments of inertia and can experience various forces, including buoyancy, added mass, drag, damping, slam, and connection loads. Lines may be attached at offset points, allowing the study of line clashing due to buoy rotation and translation.

Three buoy types are available: lumped, spar, and towed fish. Lumped buoys will be employed in this dissertation. These buoys do not have a defined geometry and model buoyancy as varying linearly with vertical displacement, while neglecting orientation-dependent effects such as rotational stiffness.

Further details are available in the OrcaFlex documentation [79].

3.1.4 Vessel object

This subsection explores the Vessel object in OrcaFlex. Due to the extensive capabilities of this element, only the features relevant to the modelling of semisubmersible platforms will be addressed.

In OrcaFlex, vessel motion can be defined using a variety of approaches. For simple simulations or predefined operations (e.g., remotely operated vehicle - ROV - deployment or vessel manoeuvres during installation), motions can be prescribed directly via time histories or harmonic inputs. In these cases, the vessel's movement is not computed by the software but imposed onto the system as external input [80].

However, the Vessel object is primarily intended for modelling rigid bodies representing large floating structures where wave-body interaction is non-negligible, such as ships, barges, tension leg platforms (TLPs), and semi-submersibles. For these cases, the vessel's dynamic response to waves is not imposed but computed using hydrodynamic data such as Response Amplitude Operators (RAOs), Quadratic Transfer Functions (QTFs), and added mass and damping matrices. These parameters are typically generated through an external diffraction analysis tool like OrcaWave or WAMIT and imported into

OrcaFlex. Depending on the modelling objective, the vessel's motion can either be imposed using displacement RAOs, or be solved dynamically, accounting for loads from connected elements and hydrodynamic forces [80].

To accurately simulate a floating body, OrcaFlex requires substantial input data. Basic configuration options, such as the vessel's initial position and how its motion is treated, are defined within the vessel's data form. More general hydrodynamic properties, such as RAOs, QTFs, and geometric data, are associated with the vessel type. Each vessel object can be linked to a specific vessel type and draught, enabling consistency across similar floating bodies [80].

3.1.4.1 Vessel Calculation Data

Static Analysis The static analysis settings define whether the equilibrium position of the vessel is calculated or whether the vessel remains at its initial position. The options are as follows [81]:

- **None**: The vessel remains at the user-defined initial position, which may not correspond to static equilibrium.
- **3 DOF**: The equilibrium position is calculated in surge, sway, and heading. Heave, roll, and pitch remain at their initial values, which may result in non-zero vertical forces and trimming moments at equilibrium.
- **6 DOF**: The equilibrium position is determined for all six degrees of freedom, resulting in balanced forces and moments in all directions.

Wave-related loads do not contribute during static analysis, except for the mean drift component if wave drift damping is enabled.

Dynamic Analysis In time domain dynamic simulations, vessel motion is represented by primary motion and an optional superimposed motion [81]:

- **Primary Motion**: Defines the main position of the vessel and can be set as:
  - None: No dynamic motion; the vessel retains the static position.
  - Prescribed: The vessel follows a user-specified trajectory or velocity profile.
  - Calculated (3 DOF): Motion is solved dynamically in surge, sway, and yaw, considering external loads and connected objects.
  - Calculated (6 DOF): Full six-degree-of-freedom motion is calculated based on hydrodynamic and external loads.
  - Time History: The primary position is defined as a function of time.
  - Externally Calculated: The motion is supplied through an external function.

  In summary, Time History uses a pre-defined time series. Prescribed applies motion from built-in or user-defined parametric functions. Calculated derives the motion numerically from the system's dynamic response.

- **Superimposed Motion**: Defines an offset applied to the primary position, with the following options:

  - None: No offset is applied.
  - RAOs + Harmonics: Harmonic motion resulting from wave RAOs and/or user-defined harmonics is superimposed.
  - Time History: A time-dependent offset is applied.

When both low frequency and wave frequency vessel motions are relevant, OrcaFlex allows these to be modelled separately through the combination of primary motion and superimposed motion. Each is optional and, when both are defined, the superimposed motion is applied concurrently as an offset to the primary motion [82].

Various load components depend differently on these motions. Added mass, radiation damping, and the interpolation or phase of displacement RAOs are evaluated using the full primary motion, unaffected by any filtering choices or dividing period. Other load types, such as wave load RAOs, wave drift Quadratic Transfer Functions (QTFs), and sum frequency QTFs, depend on the vessel calculation mode: they either use the low frequency component when filtering is applied, or the entire primary motion when QTF modification is selected [82].

Specific effects such as wave drift damping, manoeuvring load, current and wind loads are based solely on the low frequency primary motion. The choice of dividing period becomes essential when both motion types are present, as it defines the boundary between low and wave frequency components for filtering [82].

3.1.4.2 Dividing Period in Time Domain Analysis

In time domain simulations, different hydrodynamic loads on the vessel depend on distinct components of its primary motion. Some loads are influenced by low-frequency motions, others by wave-frequency motions, and some by the full spectrum. To properly handle these effects, OrcaFlex requires the user to define how the primary motion is to be interpreted: as low-frequency, wave-frequency, or a combination of both [81].

When a combined approach is selected, a **dividing period** must be defined. This value serves as a threshold to separate the primary motion into low-frequency and wave-frequency components via filtering. Motions with periods longer than the dividing period are assigned to the low-frequency domain, while those with shorter periods are treated as wave-frequency motions [81].

Choosing an appropriate dividing period is essential. It should be greater than the highest significant wave period and lower than the smallest period associated with slow-drift response. This ensures an accurate separation of dynamic effects and avoids overlap between spectral contributions [81].

3.1.4.3 Included effects

In OrcaFlex, various vessel load effects can be incorporated into the analysis to accurately simulate the environmental and operational conditions acting on the vessel. These effects can be selected individually by ticking their corresponding check boxes on the calculation page of the vessel data form [81].

Wave Load (1st Order): This effect models the linear wave-induced loads on the vessel, characterized by RAOs provided on the vessel type form under the load RAOs page. These loads represent the primary wave action on the vessel hull [81]. Beyond displacement RAOs, which indicate how a vessel moves in response to waves, OrcaFlex can utilize **wave load RAOs** to represent the forces and moments exerted on the vessel by wave action. Instead of describing motion amplitudes, these RAOs quantify the magnitude of wave-induced loads in the surge, sway, and heave directions, as well as moments in roll, pitch, and yaw [83]. The amplitude corresponds to the load per unit of wave amplitude, with the phase indicating the relative timing within the wave cycle

It should be emphasized that wave load RAOs by themselves do not fully describe vessel motion. Instead, OrcaFlex combines these wave-induced forces and moments with other vessel loads and the vessel's mass and inertia properties to solve the equations of motion [83].

Wave Drift Load (2nd Order): Representing the nonlinear wave drift forces, these loads are defined using QTFs available on the vessel type form under the wave drift QTFs page. Wave drift loads account for second-order wave effects and are essential for long-period motions and low-frequency responses [81]. Further details about the Newman's approximation method (as in [84]) and the full Quadratic Transfer Functions (QTFs) approach, along with comparative results, can be found in [85].

Wave Drift Damping: This effect accounts for energy dissipation due to wave-induced damping. It does not require separate data input but must be enabled in conjunction with the wave drift load. This damping is described in the time or frequency domain theory of wave-vessel interactions [81].

3.1.4.4 Inertia Compensation

In OrcaFlex, the inertia characteristics of a vessel are determined by the properties defined in the selected vessel type. However, in many simulations, it becomes necessary to refine these values using compensating mass and inertia to account for additional components or to avoid double-counting mass contributions from other elements (e.g., lines or point masses).

The effective mass used in the analysis is computed by subtracting the compensating mass from the original mass defined by the vessel type. This results in a reduced mass with a new centre of mass, which OrcaFlex then uses for dynamic calculations [86].

When dealing with moments of inertia, the subtraction process requires that both the vessel-type inertia tensor and the compensating inertia tensor are referenced to the same coordinate origin.

OrcaFlex automatically adjusts (or shifts) the compensating inertia tensor to ensure this condition is met, thereby enabling a valid and physically consistent subtraction [86].

The influence of the compensating inertia extends beyond dynamic response, it also modifies the hydrostatic restoring stiffness of the vessel. Specifically, OrcaFlex removes moment-arm contributions related to the compensating mass (evaluated at the compensating centre of mass) from the original hydrostatic stiffness [86]. If the vessel type also includes an explicitly defined centre of buoyancy, then an additional adjustment is made to remove further moment-arm contributions, this time evaluated using the reduced vessel mass and its updated centre of mass [86]. These corrections are essential for ensuring accurate hydrostatic stiffness and consistent coupling between mass and buoyancy effects in six degrees of freedom.

3.1.4.5 Hydrostatic Stiffness, Added Mass, and Damping

The **hydrostatic stiffness matrix** quantifies how buoyancy and net weight forces vary with displacement from the equilibrium position. In OrcaFlex, only the heave, roll, and pitch degrees of freedom contribute to this matrix, and it must be defined relative to the vessel's reference origin using the standard axis conventions. Its influence is only included if the vessel's motion is actively calculated (not imposed), particularly when set to 6 degrees of freedom [87].

Added mass and damping can be defined using either constant or frequency-dependent matrices. The constant approach uses single-valued matrices suitable for narrowband motion, typically selecting values that match the dominant wave frequency or low-frequency motion (e.g. slow drift). In contrast, the frequency-dependent method allows for added mass and damping matrices to be defined over a range of frequencies, better capturing dynamic behaviour across the spectrum [87].

To prevent computational inefficiencies in long simulations, OrcaFlex allows control over the convolution integral used to compute frequency-dependent terms. Users can define the integration time step and apply a cutoff time, beyond which the impulse response is neglected. Alternatively, a damping approximation tolerance can be provided, enabling OrcaFlex to automatically estimate a suitable cutoff time [87]. These hydrodynamic coefficients are typically generated via diffraction analysis tools such as OrcaWave, WAMIT, or AQWA, and imported directly into OrcaFlex.

3.1.5 Morison elements

Building on the theoretical formulation of Morison's equation presented before, OrcaFlex implements these hydrodynamic forces through **Morison elements**, which model slender structural components (e.g., braces, risers) attached to a vessel or 6-DOF buoy [88]. These elements consist of discretised cylinders (segments) that capture drag and inertia forces not included in diffraction analysis, effectively translating the theory into a numerical representation.

Key features:

- **Geometry**: Defined by end-points (A to B), segment length L, number of segments N, and orientation (azimuth, declination, local axes).

- **Drag Force**: Quadratic drag based on normal (C_{D_x}, C_{D_y}) and axial (C_{D_z}) drag coefficients and corresponding diameters (d_n, d_a).
- **Added Mass and Inertia**: Specified via coefficients (C_{a_i}) and inertia coefficients (C_{m_i}), with the option to compute C_m automatically as $C_m = 1 + C_a$.
- **Hydrodynamic Load Computation**: For each segment, drag and inertia forces are calculated using the local fluid velocity and acceleration, summed across segments. Partial submergence is accounted for using a segment wetness ratio.
- **Integration with Diffraction Loads**: Morison elements complement diffraction-based hydrodynamic loads (RAOs, QTFs), with their contributions added to the total forces and moments acting on the structure.

Although both Morison elements and Lines in OrcaFlex use **Morison's equation** to calculate hydrodynamic drag and inertia forces, the implementation differs. For Lines, these forces are computed internally for each segment based on the hydrodynamic coefficients defined, without requiring a separate element. Morison elements, on the other hand, are stand-alone objects that can be attached to vessels, buoys, or shapes, and are intended for slender structural components not modelled as lines. Morison elements are often used to capture viscous drag effects that are not adequately represented by diffraction-based hydrodynamic models, providing a more complete load representation for certain geometries.

3.1.6 Turbine Object

The *OrcaFlex* turbine object is designed to model horizontal axis wind turbines in a detailed and flexible manner. The turbine object includes dedicated models for the generator, gearbox, hub, and blades. External functions can be used to implement blade pitch control and generator torque or motion control. Blades may be modelled either as rigid bodies or as flexible structures, allowing aeroelastic coupling effects to be captured. The structural model of a blade is analogous to that used for lines [89].

3.1.6.1 Aerodynamic Load Calculation

Aerodynamic loading is determined using a Blade Element Momentum (BEM) method adapted from AeroDyn [89]. In its standard form, the model assumes quasi-steady conditions, also referred to as equilibrium wake, where induction factors for each blade segment are recalculated at each time step (or solver iteration) based on the instantaneous relative flow [90].

The BEM formulation in *OrcaFlex* offers flexibility: axial induction and/or tangential induction. Additional corrections such as Prandtl tip and hub loss factors and the Pitt and Peters skewed wake correction can be enabled as required. If the skewed wake correction is enabled, it is applied independently from the induction factor calculation. The influence of the turbine tower on local flow conditions may also be considered [91].

The flow conditions for each blade segment are used to compute distributed aerodynamic forces and moments. These are expressed per unit length and then integrated over the blade span. Each segment's load is characterised by dimensionless coefficients: lift coefficient C_L, drag coefficient C_D, and moment coefficient C_M, all functions of the local angle of attack α. The relationships are [92]:

$$C_L(\alpha) = \frac{L}{\frac{1}{2}\rho_a u_{\text{rel}}^2 c} \tag{3.5}$$

$$C_D(\alpha) = \frac{D}{\frac{1}{2}\rho_a u_{\text{rel}}^2 c} \tag{3.6}$$

$$C_M(\alpha) = \frac{M}{\frac{1}{2}\rho_a u_{\text{rel}}^2 c} \tag{3.7}$$

where ρ_a is the air density, u_{rel} is the relative velocity at the section, and c is the chord length.

3.1.6.2 Turbine Structure Definition

In OrcaFlex, a turbine is represented as a dedicated part type, in the same way as vessels or lines. This part comprises the relevant components, whose relative positions and orientations are specified within the model. The turbine frame can be fixed or connected to a parent object but cannot be free. The rotor hub rotates about the turbine's z-axis, with positive rotation defined as clockwise when viewed along the positive z direction. For a conventional turbine, this axis aligns with the wind velocity. Figure 3.2 illustrates the key frames of reference associated with the turbine object.

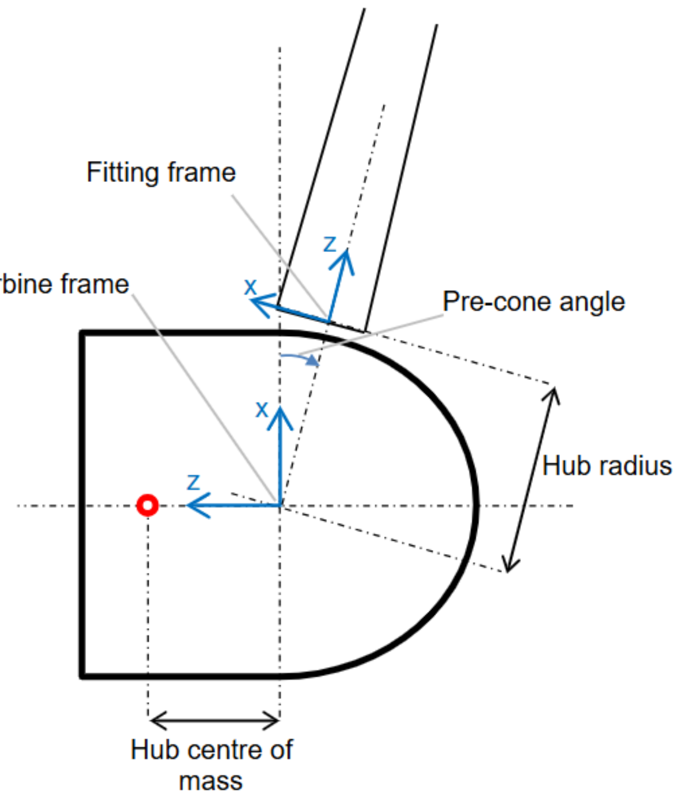

Figure 3.2: Frames of reference for the turbine object in OrcaFlex [89]

Blades are defined relative to the hub through a fitting frame determined by the hub radius, pre-cone angle, and blade count. Each blade is divided into sections, with each section assigned a wing type that specifies aerodynamic coefficients. Structural and geometrical properties are defined at discrete points along the blade span and are interpolated for intermediate positions. All blades share an identical structure, and their positions around the hub are set according to the specified blade count [89].

3.2 Problem Definition

The aim of this study is to determine the coupled frequencies of a floating offshore wind turbine system under different operating conditions. These frequencies will be obtained by analysing the dynamic response of the structure in the frequency domain.

To achieve this objective, two distinct OrcaFlex models were developed. Both models share the same components for the wind turbine, tower, moorings, and environmental conditions. The only difference between them lies in the modelling approach for the semi-submersible platform:

- The first model employs a simplified representation of the semi-submersible, using only line elements connected with infinite stiffness, effectively modelling the platform as a rigid body.
- The second model uses vessel objects with Morison elements to account for viscous drag effects and provide a more realistic hydrodynamic response.

Dynamic simulations will be carried out for a duration of six hundred seconds for each case. This time duration is a well-established practice in wind turbine time-domain analysis, not limited to floating systems. Industry standards, such as IEC 61400-1 Ed.4, prescribe 10-minute intervals for event analysis, particularly in the context of production assessment, as they provide a balance between capturing dynamic effects (e.g. turbulence and wave loading) and ensuring computational feasibility [60]. While longer durations can be used to investigate slow-drift or long-period responses, studies show that shorter simulations, combined with sufficient sampling, can yield accurate and statistically robust load estimations [93, 94]. The displacement time history at the tower top will then be analysed in the frequency domain using a Fast Fourier Transform (FFT). Finally, a band-pass filter can be applied to select the desired frequency range and discard the influence of the *3P* frequency associated with the turbine's rated operating condition.

Additional validation of the results was performed through various independent tests, the calculation of natural frequencies for each structure, conducting free decay tests and performing chirp excitation tests (with null environment conditions).

3.2.1 Location-Dependent External Loading

According to the requirements defined in the Germanischer Lloyd (GL) guidelines [58] and IEC 61400-3 standard [61], the structural analysis of offshore wind turbines must account for the environmental conditions at the intended site. In this study, a location north of the Shetland Islands (61°20'N latitude, 0°00'E longitude; see Figure 3.3) has been selected, as also considered in the NREL reference report [62]. This site is characterised by extreme wind and wave conditions, making it suitable to investigate the coupled frequency response of the floating structure under representative operational loads.

Figure 3.3: Location of the turbine considered for the analysis (adapted from Google Earth).

Table 3.1 presents the normal sea state and turbulence models adopted for this work, which serve as the basis for the definition of the design load cases (DLC). These are based on DLC 1.1 of the GL [58] and IEC 61400-3 [61] standards, which corresponds to the simulation of the turbine's normal operating conditions, with wind speeds ranging from cut-in to cut-out.

Table 3.1: Definition of Wind and Wave Models [61] [62]

Abbr.	Name	Description
NSS	Normal Sea State	Irregular sea state derived from JONSWAP spectrum, reduced to Pierson-Moskowitz in less extreme conditions. Represented by sinusoidal wave components (Airy theory).
NTM	Normal Turbulence Model	Stochastic 3-component wind with 90% quantile turbulence deviation (class B), on a wind profile with $\alpha = 0.14$.

The statistical wind and wave data employed in this study are provided in [62]. It is important to note that, as in most cases, the available wind speed data were not measured at the rotor hub height (90 m).

Instead, the reference height z_{ref} of the measurements was 10 m above mean sea level. Therefore, as explained in Section 2.4.2, the power law was applied with an exponent $\alpha = 0.14$, in accordance with the GL guidelines [58]. In the statistical processing, it was also considered that the wave spectrum to be adopted was the Pierson–Moskowitz spectrum ($\gamma = 1$). The procedure for acquiring and processing both wind and wave data is thoroughly documented in [62]. Figure 3.4 shows the joint probability distribution of significant wave height and the associated peak period intervals, conditioned by the wind speed at rotor height, i.e., $E[H_s|\overline{u}_v]$ and $E[T_p|\overline{u}_v]$, respectively. The corresponding trend lines are also presented. Equations 3.8–3.9 represent the relationships obtained (6th order polynomial) for the data considered.

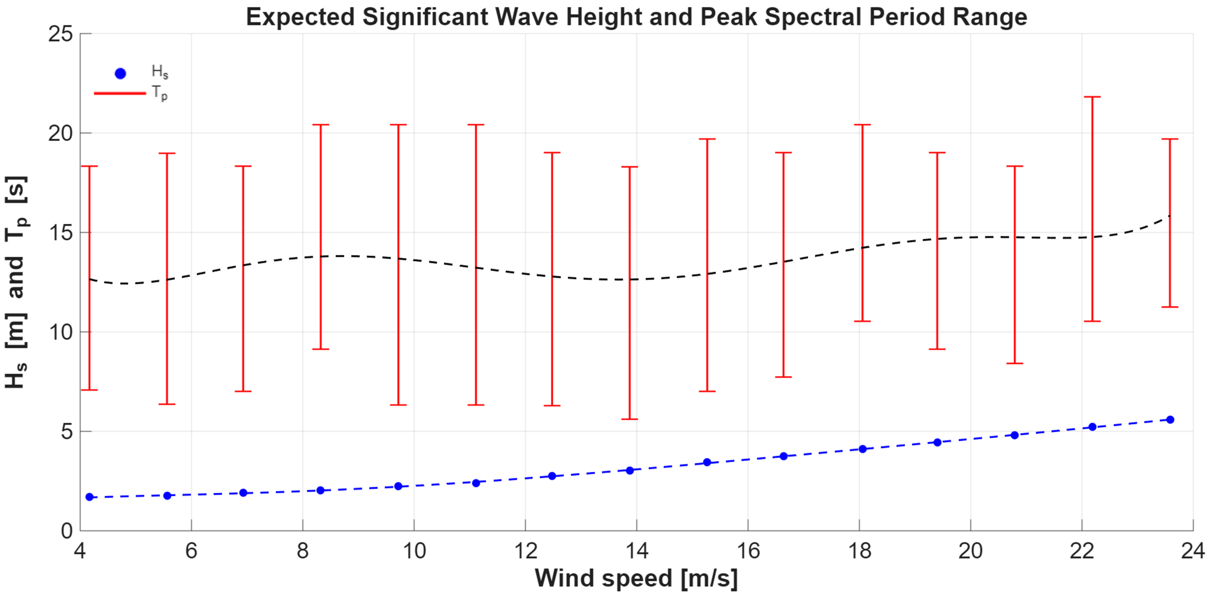

Figure 3.4: Joint probability of sea state conditioned by wind speed and corresponding trend lines (adapted from [62]).

$$\begin{aligned} f_{H_s}(\overline{u}_v) = & -2.12\times10^{-7}\,\overline{u}_v^6 + 2.11\times10^{-5}\,\overline{u}_v^5 - 8.25\times10^{-4}\,\overline{u}_v^4 + 1.57\times10^{-2}\,\overline{u}_v^3 \\ & - 1.43\times10^{-1}\,\overline{u}_v^2 + 6.76\times10^{-1}\,\overline{u}_v + 4.31\times10^{-1} \end{aligned} \tag{3.8}$$

$$\begin{aligned} f_{T_p}(\overline{u}_v) = & \ 1.61\times10^{-5}\,\overline{u}_v^6 - 1.34\times10^{-3}\,\overline{u}_v^5 + 4.39\times10^{-2}\,\overline{u}_v^4 - 7.14\times10^{-1}\,\overline{u}_v^3 \\ & + 6.02\,\overline{u}_v^2 - 24.5\,\overline{u}_v + 50.3 \end{aligned} \tag{3.9}$$

where $\overline{u}_v$ is the 10-m mean wind speed ($\mathrm{m\,s^{-1}}$), $f_{H_s}(\overline{u}_v)$ is the fitted trend function for the significant wave height H_s (m), and $f_{T_p}(\overline{u}_v)$ is the fitted trend function for the spectral peak period T_p (s). The sea state and wind conditions to be used in each analysis are now defined. For the certification of offshore wind turbines, the GL standard [58] specifies nine Design Load Cases (DLCs), some with multiple subcases. This dissertation focuses on DLC 1.1, as it simulates the normal operational condition of the turbine, with wind speeds ranging from cut-in to cut-out. It considers winds with normal turbulence levels (NTM) and no gusts, as well as both regular and irregular waves.

Wind files were generated using the TurbSim code according to the Kaimal spectrum (as discussed in

Section 2.4.2) and the Normal Turbulence Model (NTM). This software is responsible for generating the space–time wind series required for simulations performed with *Orcaflex* or similar codes [95]. It relies on statistical models (as opposed to physical models) to produce turbulent wind time series across all three spatial dimensions (x, y, and z).

Waves were modelled using the Airy wave theory with the Pierson-Moskowitz spectral density. Surface currents, induced by wind shear stresses on the sea surface and defined at a reference height (z_{ref}) of 20 m, were also considered. The standard requires simulations to last at least 10 minutes.

Three independent random seeds are employed for the wind field and three for the wave elevation in each case, when possible. A seed initializes the random phase (and, for wind, the spatial coherence and Fourier coefficients) of a stochastic generator so that each realization preserves the same target statistics (e.g., Kaimal spectrum, Pierson–Moskowitz spectrum, turbulence class) but produces different time histories. Multiple realizations improve the statistical convergence of estimated responses (e.g., mean values, variances, fatigue damage) and reduce sampling bias for a given sea state. In *TurbSim*, the seed determines the random Fourier components that realize the prescribed spectrum and coherence model [95], whereas in the hydrodynamic model the wave seed defines the random phases of spectral components for irregular seas (second-order statistics according to the PM spectrum), yielding distinct surface elevations with identical spectral properties [64, 91]. The use of several seeds per operating point constitutes a standard Monte Carlo practice in aero-hydro-servo simulations to capture the intrinsic variability of turbulent wind and random seas [64, 95]. Consequently, one simulation is obtained for each wind speed in Case A, while three independent realizations are evaluated for each wind speed in Cases B and C.

Table 3.2 summarizes the analysis cases with their respective wind speeds, wave parameters, and current characteristics.

Table 3.2: Cases considered for analysis and their characteristics. Three cases are evaluated at each wind speed: (A) Regular (Airy) waves with laminar, steady wind; (B) ISSC irregular waves with laminar, steady wind; (C) ISSC irregular waves with turbulent wind (Kaimal, NTM, Class B). For case A (regular waves) we use $H = H_s$ and $T = T_p$ to match the irregular-sea parameters.

$\overline{u}_v$ [m s^{-1}]	Case	Wind model	Wave model	H/H_s [m]	T/T_p [s]	$u_c(0)$ [m s^{-1}]
4	A	Laminar (steady)	Regular (Airy)	1.66	12.8	0.0441
4	B	Laminar (steady)	ISSC[1]	1.66	12.8	0.0441
4	C	Kaimal, NTM, Class B	ISSC	1.66	12.8	0.0441
6	A	Laminar (steady)	Regular (Airy)	1.82	12.9	0.0662
6	B	Laminar (steady)	ISSC	1.82	12.9	0.0662
6	C	Kaimal, NTM, Class B	ISSC	1.82	12.9	0.0662
8	A	Laminar (steady)	Regular (Airy)	1.99	13.7	0.0882
8	B	Laminar (steady)	ISSC	1.99	13.7	0.0882
8	C	Kaimal, NTM, Class B	ISSC	1.99	13.7	0.0882
10	A	Laminar (steady)	Regular (Airy)	2.26	13.6	0.1103
10	B	Laminar (steady)	ISSC	2.26	13.6	0.1103
10	C	Kaimal, NTM, Class B	ISSC	2.26	13.6	0.1103
12	A	Laminar (steady)	Regular (Airy)	2.64	12.9	0.1324
12	B	Laminar (steady)	ISSC	2.64	12.9	0.1324
12	C	Kaimal, NTM, Class B	ISSC	2.64	12.9	0.1324
14	A	Laminar (steady)	Regular (Airy)	3.09	12.6	0.1544
14	B	Laminar (steady)	ISSC	3.09	12.6	0.1544
14	C	Kaimal, NTM, Class B	ISSC	3.09	12.6	0.1544
16	A	Laminar (steady)	Regular (Airy)	3.58	13.2	0.1765
16	B	Laminar (steady)	ISSC	3.58	13.2	0.1765
16	C	Kaimal, NTM, Class B	ISSC	3.58	13.2	0.1765
18	A	Laminar (steady)	Regular (Airy)	4.10	14.2	0.1985
18	B	Laminar (steady)	ISSC	4.10	14.2	0.1985
18	C	Kaimal, NTM, Class B	ISSC	4.10	14.2	0.1985
20	A	Laminar (steady)	Regular (Airy)	4.61	14.8	0.2206
20	B	Laminar (steady)	ISSC	4.61	14.8	0.2206
20	C	Kaimal, NTM, Class B	ISSC	4.61	14.8	0.2206
22	A	Laminar (steady)	Regular (Airy)	5.15	14.7	0.2426
22	B	Laminar (steady)	ISSC	5.15	14.7	0.2426
22	C	Kaimal, NTM, Class B	ISSC	5.15	14.7	0.2426
24	A	Laminar (steady)	Regular (Airy)	5.72	16.71	0.2647
24	B	Laminar (steady)	ISSC	5.72	16.71	0.2647
24	C	Kaimal, NTM, Class B	ISSC	5.72	16.71	0.2647

3.2.2 NREL 5 MW Wind Turbine Definition

The floating system employs the NREL 5 MW reference wind turbine mounted on the OC4 semisubmersible floater [29, 41, 96]. The machine is a three-bladed, upwind, variable-speed turbine with collective pitch control. The rotor–nacelle assembly (RNA) is represented as a 6-DOF buoy with prescribed mass properties; the tower is modelled as an *OrcaFlex* line discretised into 78 segments of 1 m, with axial, bending *and* torsional stiffness included. Aerodynamic loads are applied through a turbine object with two active controllers: collective blade pitch and generator torque; other blade DOFs are locked, consistent with the steady-state operating points previously defined.These controllers are provided within OrcaFlex by Orcina for this turbine [97]. No tower-shadow or tower-interference aerodynamic effects are included.

The fundamental rotational (1P) and blade-passing (3P) bands over the operating range 6.9–12.1 rpm are approximately $f_{1P} \in [0.115, 0.202]$ Hz and $f_{3P} \in [0.345, 0.606]$ Hz, respectively, and are used later to assess potential resonance with structural modes [29]. Key turbine characteristics used in the model are summarised in Table 3.3, which defines the operational ranges (e.g., rated speed, drivetrain, control) referenced in the Campbell analysis and controller setup.

Table 3.3: Baseline properties of the NREL 5 MW turbine [29].

Property	**Value**
Rated power	5 MW
Rotor orientation / configuration	Upwind, 3 blades
Control strategy	Variable speed, collective pitch
Drivetrain	High-speed, multi-stage gearbox
Rotor diameter / hub diameter	126 m / 3 m
Hub height	90 m
Cut-in / rated / cut-out wind speed	3 / 11.4 / 25 m s^{-1}
Cut-in / rated rotor speed	6.9 / 12.1 rpm
Rated tip speed	80 m s^{-1}
Precone angle (per blade)	2.5°
Gearbox ratio	97:1
Rated generator speed	1173.7 rpm
Generator efficiency (rated)	94.4%
Generator inertia about HSS	534.116 kg m^2

The nacelle and hub were modelled in *Orcaflex* as a lumped buoy with prescribed mass, inertia, and centre of mass values. The axis system of the nacelle is rotated by 180° about the global z-axis to align with the rotor orientation, while the semisubmersible platform retains the same orientation as the global axes. The tower coordinates are defined relative to the semisubmersible reference frame. The main mass, inertia, and hydrodynamic properties assigned to the nacelle in the *OrcaFlex* implementation are summarised in Table 3.4.

Similarly, the parameters used for the hub and generator, which complement the nacelle properties in

[1] In *OrcaFlex*, the **ISSC spectrum** corresponds to the so-called *modified Pierson–Moskowitz* spectrum. It has the same functional form as the PM spectrum but allows the user to specify significant wave height H_s and peak period T_p directly, rather than enforcing the fully developed wind–wave relation.

Table 3.4: Implemented nacelle properties in *OrcaFlex* (lumped buoy object) [41, 96, 97].

Property	Value
Mass	240 t
Mass moment of inertia (x-axis)	350.024 te·m^2
Mass moment of inertia (y-axis)	5409.87 te·m^2
Mass moment of inertia (z-axis)	2607.89 te·m^2
Centre of mass (x, y, z)	$(-1.9113, 0.0, -0.04616)$ m
Volume	114.294 m^3
Height	3.5 m
Drag area in x-direction	8.0 m^2
Drag area in y-direction	50.0 m^2
Drag area in z-direction	32.656 m^2
Drag coefficient C_d (x)	1.0
Drag coefficient C_d (y)	1.2
Drag coefficient C_d (z)	1.2

the model, are presented in Table 3.5.

Table 3.5: Implemented hub and generator properties in OrcaFlex [41, 96, 97].

Property	Value
Hub	
Hub radius	1.5 m
Hub mass	56.78 t
Hub inertia (axial)	115.926 te·m^2
Generator	
Gear ratio	97:1
Generator inertia (HSS)	0.53412 te·m^2

Figure 3.5 provides a close-up of the implemented nacelle and hub axes, while Figure 3.6 shows the complete tower–nacelle–hub system together with the rotor blades. The tower was discretised into 78 line elements of 1 m length, and the rotor blades were segmented according to their aerofoil distribution (full details in [29]).

Geometric and mass properties of the tower, together with the numerical discretisation adopted in *OrcaFlex*, are compiled in Table 3.6.

Spanwise blade segmentation used in *OrcaFlex* (for geometry/airfoil assignment and sectional property mapping) is listed below; detailed distributed geometric, inertial and structural properties are provided in the full report in [29].

Each blade has a precone of 2.5°, i.e., the blade pitch axis is inclined so that the blade tips sweep a coned surface rather than a plane normal to the shaft. Precone affects effective inflow angle, load distribution and blade–tower clearance [29, 92]. A schematic representation of the precone angle is provided in Figure 3.7.

[2] An elevated effective density is used relative to nominal steel (7850 kg m^{-3}) to account for paint, bolts, welds and flanges not captured by the shell thickness data [29].

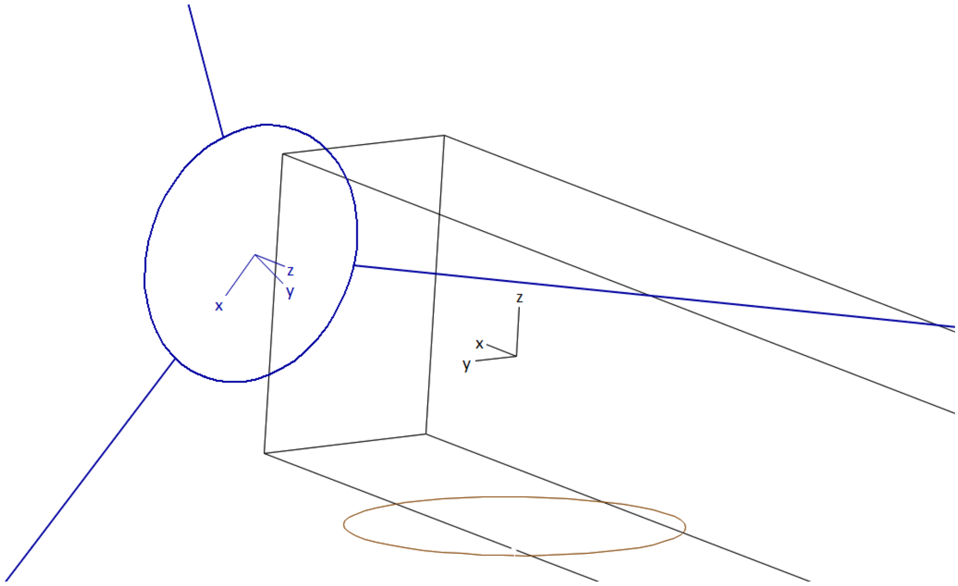

Figure 3.5: Close-up of the modelled nacelle and hub with axis definition (nacelle axes rotated 180° around z).

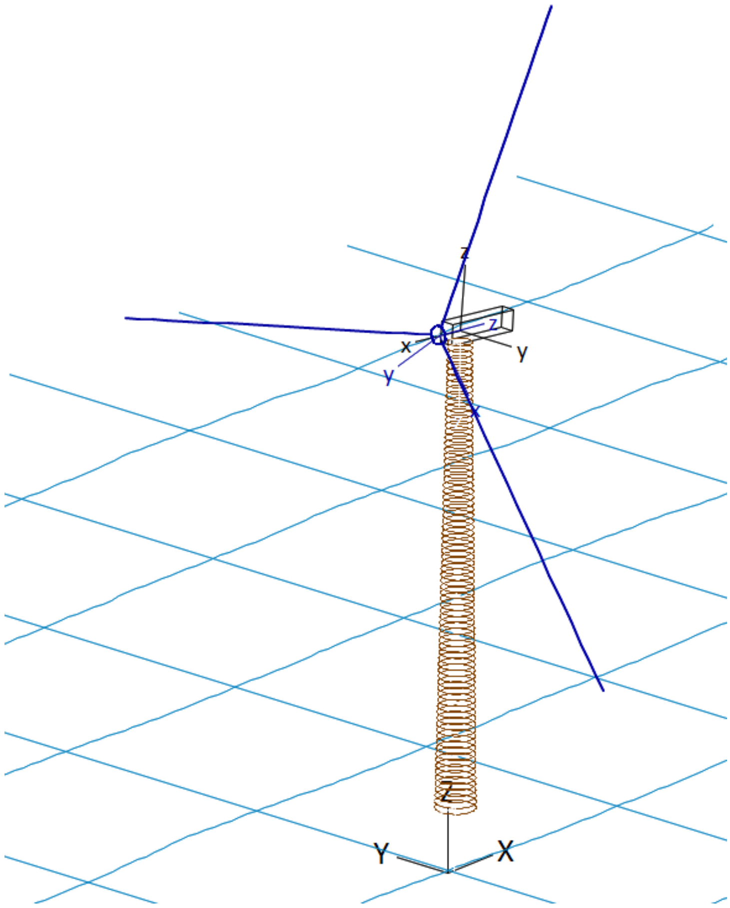

Figure 3.6: Full turbine model in *Orcaflex*, including tower, nacelle, hub, and blades.

Table 3.6: Tower properties [29].

Property	Value
Young's Modulus	210 MPa
Top / base elevation above SWL	87.6 m / 10 m
Tower length	75.6 m
Top diameter / thickness	3.87 m / 0.019 m
Base diameter / thickness	6.50 m / 0.027 m
Steel density (effective)[2]	8500 $\mathrm{kg\,m^{-3}}$
Total tower mass	2.497×10^5 kg
Tower CM above SWL	43.4 m
Discretisation in model	78 segments of 1 m (torsion included)

Table 3.7: Blade spanwise segmentation and airfoil families [29].

No.	Section length (m)	# segments	Wing type	Cumulative length (m)
1	5.467	2	Cylinder	5.467
2	2.733	1	Cylinder	8.200
3	4.1	1	DU40	12.3
4	8.2	2	DU35	20.5
5	4.1	1	DU30	24.6
6	8.2	2	DU25	32.8
7	8.2	2	DU21	41.0
8	12.3	3	NACA64	53.3
9	8.2	3	NACA64	61.5

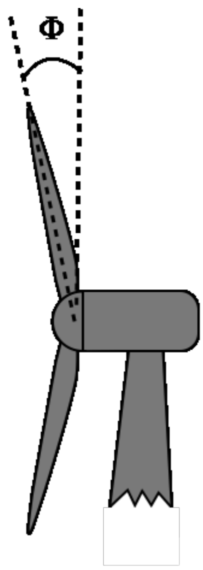

Figure 3.7: Schematic illustration of blade precone angle Φ. Adapted from [98].

3.2.3 Mooring System Definition

The floating foundation is anchored to the seabed using a three-line catenary mooring system, with each line, made of studless steel, spaced 120° apart. The mooring fairleads are positioned on the outer columns (BCs), at a radial distance of 40.85 m from the central column (MC). In order to remain consistent with the original OC4 configuration and the chosen site, the water depth was defined as 200 m. Consequently, the anchors are placed at a depth of 200 m and at a horizontal distance of 837.6 m from the platform's centre, assuming it remains in its undisplaced position. One of the mooring lines is aligned with the negative x-direction within the xz-plane. The overall characteristics of the mooring system are summarised in Table 3.8 [41].

Table 3.8: Mooring System Properties [41]

Property	**Value**
Number of mooring lines	3
Angle between adjacent lines	120°
Depth to anchors below SWL	200 m
Depth to fairleads below SWL	14 m
Radius to anchors from platform centreline	837.6 m
Radius to fairleads from platform centreline	40.868 m
Unstretched mooring line length	835.5 m
Mooring line diameter	0.0766 m
Equivalent mooring line mass density	113.35 kg/m
Equivalent mooring line mass in water	108.63 kg/m
Equivalent mooring line extensional stiffness	753.6 MN
Hydrodynamic drag coefficient for mooring lines	1.1
Hydrodynamic added-mass coefficient for mooring lines	1.0
Seabed drag coefficient for mooring lines	1.0
Structural damping of mooring lines	2.0%

In this configuration, the mooring lines are initially slack at equilibrium, implying that dynamic offsets will occur in response to environmental loading. In OrcaFlex, these lines are modelled using Line elements, discretised into segments of 10 m to accurately capture the behaviour of the mooring system throughout the simulation. The mooring layout in the basin is shown in Figure 3.8.

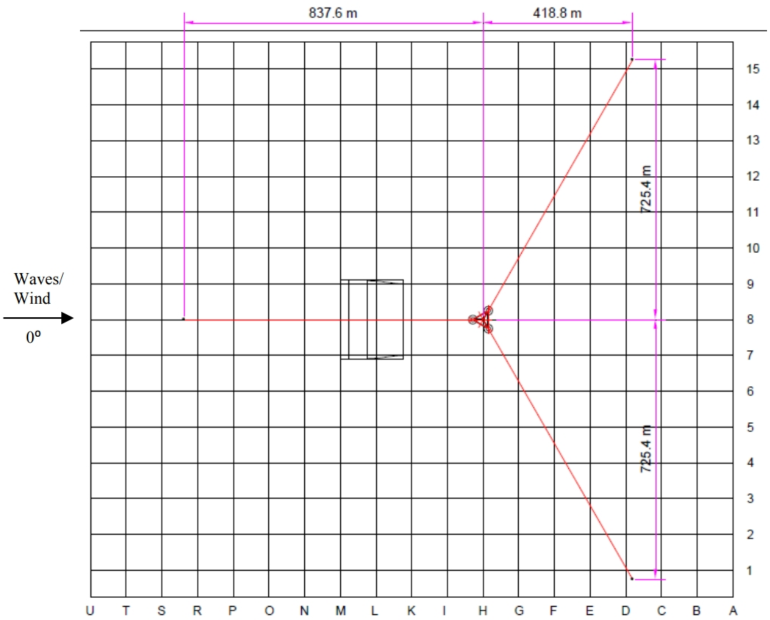

Figure 3.8: Mooring line arrangement [41]

3.2.4 DeepCWind Semisubmersible Definition

Defined in [41], the semisubmersible platform considered in this work is based on the DeepCWind foundation design, developed within the DeepCWind consortium. The structure consists of a central main column (MC) surrounded by three outer columns, each divided into two cylindrical segments: the upper column (UC) and the bottom column (BC). The three outer columns are located at the vertices of an equilateral triangle and are connected by a system of slender pontoons and braces. This geometry provides both buoyancy and stability, while the large-diameter bottom columns act as heave plates, enhancing hydrodynamic resistance in heave, pitch, and roll motions. A schematic representation of the structural layout and the ballast configuration is shown in Figures 3.9 and 3.10, while the main member dimensions are summarised in Table 3.9.

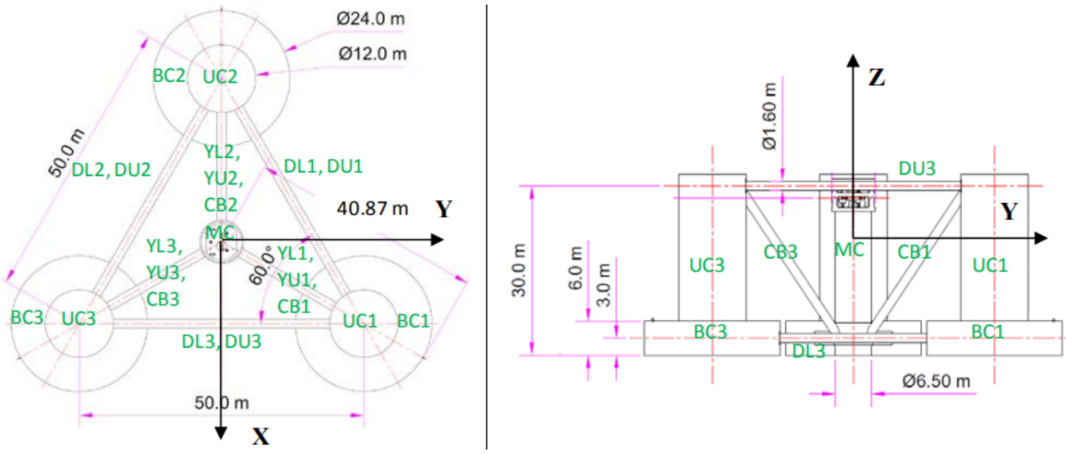

Figure 3.9: Main dimensions and structural layout of the OC4 semisubmersible platform [41].

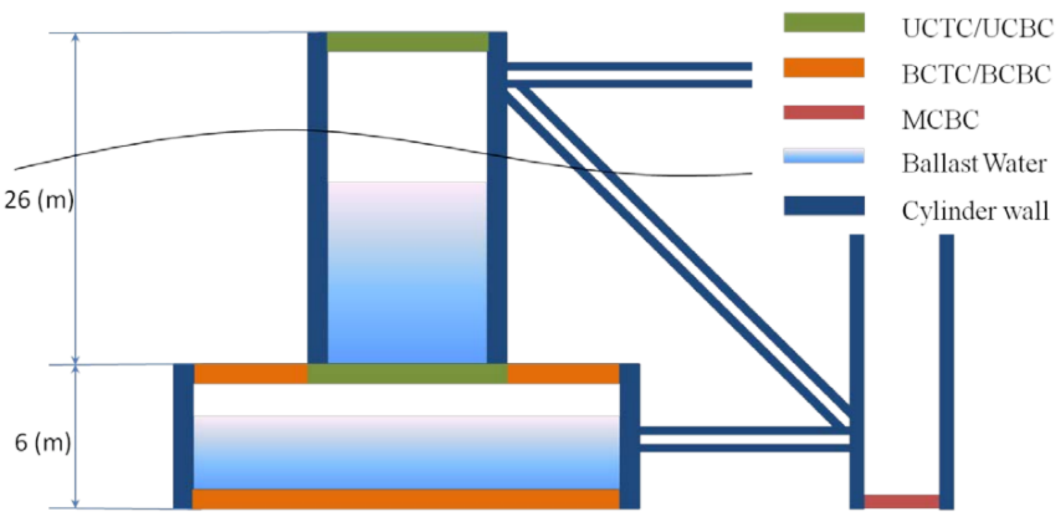

Figure 3.10: Ballast configuration of the OC4 semisubmersible platform [41].

Table 3.9: Members dimensions [41]

Member Identification	Diameter [m]	Length [m]	Wall Thickness [mm]
MC	6.5	32	30
UC	12	26	60
BC	24	6	60
DU	1.6	38	17.5
DL	1.6	26	17.5
YU	1.6	19.6	17.5
YL	1.6	13.6	17.5
CB	1.6	32	17.5

The pontoons interconnecting the main and outer columns are classified according to their location: upper and lower horizontal members (YU and YL), upper and lower diagonal braces (DU and DL), and centre beams (CB). These members provide structural stiffness and constrain the relative motions of the columns. Independent ballast tanks are incorporated in each column, enabling adjustments of the vertical position of the centre of mass (CM), which is critical for platform stability.

The ballast was explicitly modelled to account for the total water mass of 9.6208×10^6 kg (as given in [41]), distributed evenly among the three outer columns. Each UC is filled with water from its bottom up to 6.17 m below the still water level (SWL), while each BC is filled from the platform draft up to 5.11 m above the draft. To represent this ballast in the numerical model, point loads were applied at the calculated centres of mass of the flooded volumes. The CM of each outer column, including the cap and ballast weight, is located 6.19 m above the bottom end, while the CM of the central column is located 14.24 m above its base.

The global structural properties of the platform, including ballast, are summarised in Table 3.12, while the detailed mechanical properties of individual members (metallic mass, mass per unit length, and stiffness parameters) are presented in Table 3.10. Hydrodynamic properties, including hydrostatic restoring coefficients[3], added-mass and drag coefficients, and quadratic damping terms, are listed in Table 3.11.

Table 3.10: Properties of structural members [41].

Member	Metal mass [kg]	Mass/length [kg/m]	EI [N·m^2]	GJ [N·m^2]	EA [N]
MC	1.436E+05	4.787E+03	6.701E+13	5.038E+13	1.281E+13
UC	4.594E+05	1.767E+04	8.423E+14	6.333E+14	4.726E+13
BC	2.125E+05	3.542E+04	6.789E+15	5.105E+15	9.476E+13
DU	2.599E+04	6.830E+02	5.720E+11	4.301E+11	1.827E+12
DL	1.778E+04	6.830E+02	5.720E+11	4.301E+11	1.827E+12
YU	1.329E+04	6.830E+02	5.720E+11	4.301E+11	1.827E+12
YL	9.164E+03	6.830E+02	5.720E+11	4.301E+11	1.827E+12
CB	2.142E+04	6.830E+02	5.720E+11	4.301E+11	1.827E+12

[3] Positive entries (e.g., C_{33} in heave) indicate that a positive displacement generates an opposing restoring force. Negative entries (e.g., C_{44}, C_{55} in roll and pitch) arise from the sign convention for restoring moments and do not imply negative stiffness or instability.

Table 3.11: Hydrodynamic properties of the floating platform [41].

Property	Value
Water density	$1025\ \mathrm{kg/m^3}$
Water depth	200 m
Displaced volume (undisplaced pos.)	$1.3917 \times 10^4\ \mathrm{m^3}$
Centre of buoyancy below SWL	13.15 m
Buoyancy force	1.3989×10^8 N
Hydrostatic restoring in heave (C_{33})	3.836×10^6 N/m
Hydrostatic restoring in roll (C_{44})	-3.776×10^8 N·m/rad
Hydrostatic restoring in pitch (C_{55})	-3.776×10^8 N·m/rad
Added-mass coefficient (C_a)	0.63
Added-mass coefficient for BC in z (C_{az})	1.0
Drag coefficient (C_d) MC	0.56
Drag coefficient (C_d) UC	0.61
Drag coefficient (C_d) BC	0.68
Drag coefficient (C_d) pontoons	0.63
Drag coefficient (C_{dz}) BC in z	4.8

Table 3.12: Floating platform structural properties (including ballast) [41].

Property	Value
Platform mass (incl. ballast)	1.3473×10^7 kg
CM location below SWL	13.46 m
Roll inertia about CM	6.827×10^9 kg·m^2
Pitch inertia about CM	6.827×10^9 kg·m^2
Yaw inertia about CM	1.226×10^{10} kg·m^2

3.2.4.1 Beam-Based Modelling of the Semisubmersible

The semisubmersible structure was represented in OrcaFlex using beam elements. The geometry was first defined according to the reference coordinates provided in [41], ensuring correct placement of all main columns, base columns, and pontoons. Each structural member was discretised into 1 m segments to allow for a sufficiently fine representation of the platform's stiffness and hydrodynamic behaviour.

Different line types were assigned to represent the structural members, with each type defined by its corresponding properties: diameter; axial, bending, and torsional stiffness; mass per unit length; drag coefficients in the global x, y, and z directions; and added-mass coefficients in the same directions. To enforce rigid connectivity between members (as well as with the tower), the lines were joined via negligible-mass 6D buoys set with infinite stiffness, effectively ensuring that the full assembly behaves as a rigid body.

The ballast and column caps were modelled using point loads applied through OrcaFlex attachments (clumps). These were located at the calculated centres of mass of each column, allowing the additional weight contribution of the ballast and caps to be properly included in the global mass distribution.

It was considered appropriate to begin with a beam-based model due to its relative simplicity and computational efficiency. This also provides a useful baseline for later comparison with a diffraction-based model, allowing the accuracy and limitations of the beam approach to be assessed in the context of the hydrodynamic response of the semisubmersible.

Figure 3.11 illustrates the final semisubmersible beam model, with its structural elements, connections, and ballast loads.

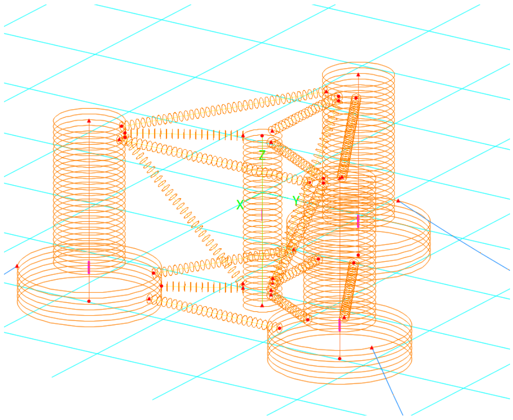

Figure 3.11: Beam-based semisubmersible model implemented in OrcaFlex.

3.2.4.2 Vessel Modelling of the Semisubmersible

The vessel-type model was built following the OrcaFlex example *L02 OC4 Semi* (for workflow consistency) and the OC4 definition of the floater [41, 82, 97]. A diffraction/radiation analysis requires a surface mesh of the wetted geometry and since OrcaWave/OrcaFlex do not include a native mesh editor and due to licensing constraints, an existing OC4 mesh was used, shown in Figure 3.12. The imported hydrodynamics comprise: (i) first-order wave-load RAOs, (ii) second-order difference-frequency (wave-drift) loads via QTFs, and (iii) hydrostatic stiffness and frequency-dependent added mass and radiation damping. Pontoons are small-diameter members; they were therefore modelled with Morison elements (drag only) rather than as diffraction bodies. In addition, viscous drag for the main and outer columns was represented together with Morison drag accounting for separation and flow-induced losses at realistic amplitudes [59, 97].

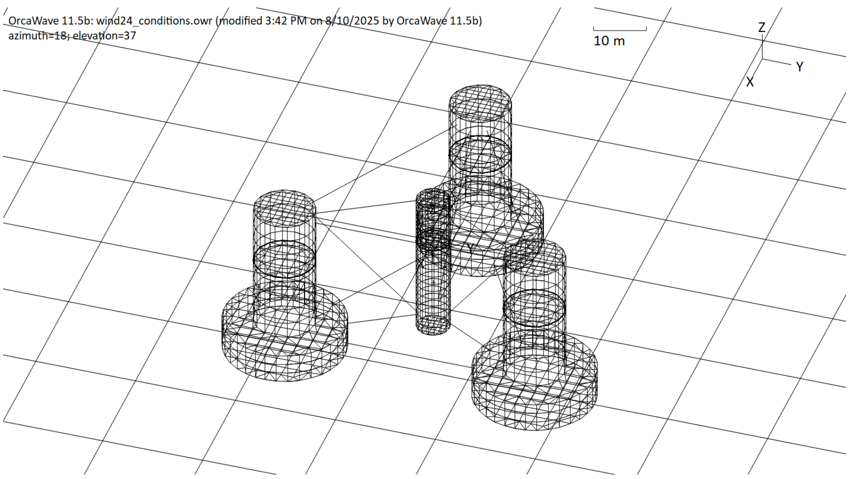

Figure 3.12: OC4 semisubmersible hydrodynamic mesh used for diffraction/radiation analysis

In OrcaWave, all hydrodynamic coefficients (added mass, radiation damping, RAOs, QTFs) are referenced to the inertia of the body under analysis. This means that even if only the semisubmersible hull is meshed and analysed as a vessel object, the subsequent hydrodynamic database implicitly assumes the full system inertia. Neglecting the contributions of the tower, nacelle, and rotor would therefore lead to incorrect natural frequencies and dynamic responses.

To address this, the complete system inertia was first calculated in OrcaFlex using *Coumpound Properties*, which combines the mass and inertia of all attached components (tower, nacelle, rotor) relative to the platform reference axes. After importing the hydrodynamic results from OrcaWave, the total system inertia must not be double-counted. Hence, the compound properties were introduced in the *Vessel → Inertia compensation* menu of OrcaFlex, so that the inertia already included in the vessel hydrodynamic file is correctly adjusted against the explicitly modelled objects [82].

The mass and centre of mass (CoM) positions of the platform and its components are summarised in Table 3.13. The corresponding mass moments of inertia about each component's CoM are listed in Table 3.14.Finally, the assembled 3×3 inertia matrix of the complete system, expressed about the global origin, is given in Table 3.15, while Figure 3.13 illustrates the compound-properties report used for the compensation step.

Table 3.13: Mass and centre of mass (CoM) properties [97].

Item	**Mass [t]**	x [m]	y [m]	z [m]
Platform	13473	0.000	0.000	-13.460
Tower	249.718	0.000	0.000	43.322
Nacelle	240	1.900	0.000	89.343
Rotor (inc hub)	110	-5.452	0.000	90.040
Total	14072.718	-0.010	0.000	-9.890

Table 3.14: Mass moments of inertia about each component's CoM [97].

Item	I_{xx} [t·m^2]	I_{yy} [t·m^2]	I_{zz} [t·m^2]
Platform	6.827E+06	6.827E+06	1.226E+07
Tower	1.206E+05	1.206E+05	1.818E+03
Nacelle	3.500E+02	5.410E+03	2.608E+03
Rotor (inc hub)	1.955E+04	1.955E+04	3.906E+04
Total	1.133E+07	1.132E+07	1.229E+07

Table 3.15: Global 3×3 inertia matrix [t·m^2] of the complete system about the global origin [97].

	x	y	z
x	$1.133E+07$	0	$1.318E+04$
y	0	$1.132E+07$	0
z	$1.318E+04$	0	$1.229E+07$

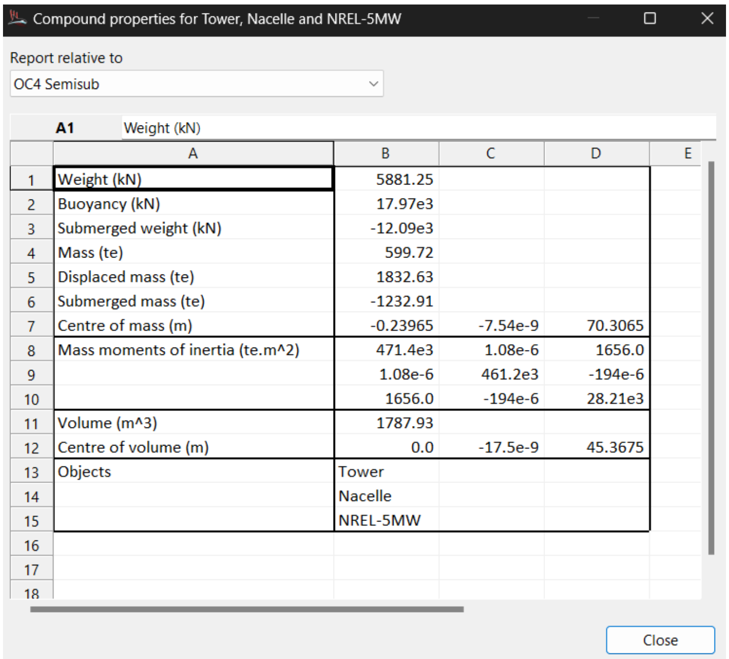

	A	B	C	D	E
1	Weight (kN)	5881.25			
2	Buoyancy (kN)	17.97e3			
3	Submerged weight (kN)	-12.09e3			
4	Mass (te)	599.72			
5	Displaced mass (te)	1832.63			
6	Submerged mass (te)	-1232.91			
7	Centre of mass (m)	-0.23965	-7.54e-9	70.3065	
8	Mass moments of inertia (te.m^2)	471.4e3	1.08e-6	1656.0	
9		1.08e-6	461.2e3	-194e-6	
10		1656.0	-194e-6	28.21e3	
11	Volume (m^3)	1787.93			
12	Centre of volume (m)	0.0	-17.5e-9	45.3675	
13	Objects	Tower			
14		Nacelle			
15		NREL-5MW			
16					
17					
18					

Figure 3.13: Compound mass and inertia report used for *Inertia compensation* (placeholder).

Twelve wave periods were analysed (10–21 s in 1 s steps). Two headings (0° and 180°) were included to satisfy software requirements; results shown later use 0° only. In the OrcaWave analysis, the mooring system is represented as an external stiffness matrix, consistent with the OC4 definition [41]. This approach allows the hydrodynamic problem to be solved without explicitly modelling the nonlinear catenary dynamics. Further implementation details are provided in the *L02 OC4 Semi* example [97].

Morison drag is proportional to the square of the relative velocity between the water particles and the structure, which makes the resulting force quadratic.[4] In OrcaFlex, this quadratic nature prevents its direct use in frequency-domain analysis, where linear relations are required. To overcome this, the drag is linearised into an equivalent damping term that depends on the representative velocity amplitude derived from the wave spectrum. Because this linearisation must be performed separately for each irregular sea state, and since OrcaWave does not allow regular waves to be specified, scenario A (regular-wave case) was not evaluated with the vessel model. The difference-frequency (slow-drift) loads were included via Newman's approximation to the second-order QTFs [85], while first-order load RAOs and radiation terms follow the standard linear potential-flow formulation [55, 56].

After importing the diffraction database from *OrcaWave*, the OC4 semisubmersible was instantiated as a *Vessel* in *OrcaFlex*, connected to the three catenary lines, and the displaced volume at equilibrium was set to 13,917 m^3. A fully coupled analysis was enforced by setting *Included in statics* = 6 DOF and *Primary motion* = 6 DOF, with *Superimposed motion* = None. The following hydrodynamic effects were enabled: first-order wave load (load RAOs), second-order wave-drift load, wave-drift damping, and frequency-dependent added mass & radiation damping.

Since *Primary motion* contains both components, a dividing period was defined so effects that depend

[4]This quadratic form arises because the drag term is proportional to dynamic pressure, $\frac{1}{2}\rho u^2$, and therefore scales with the square of velocity. In offshore hydrodynamics it is standard practice to linearise this effect for frequency-domain analysis, as recommended in sources such as [55, 59].

only on low-frequency motion (wave-drift load and wave-drift damping) use the low-frequency part of the response. A modal analysis of the moored system gave the lowest horizontal natural period in yaw, $T_{\text{yaw}} \approx 64$ s (Table 3.16). For the highest-period sea state considered (ISSC, $H_s = 5.72$ m, $T_p = 16.7$ s), the wave spectrum still concentrates energy at $f \gtrsim 0.05$ Hz ($T \lesssim 20$ s), see Fig. 3.14. Hence a dividing period of 40 s, well above the dominant wave-frequency band and well below the slow-drift modes, was adopted.

Table 3.16: First three low-frequency modes of the moored platform (from OrcaFlex modal analysis).

Mode	Period T [s]	Frequency f [Hz]
Yaw	64.173	0.01558
Sway	81.203	0.01231
Surge	96.856	0.01032

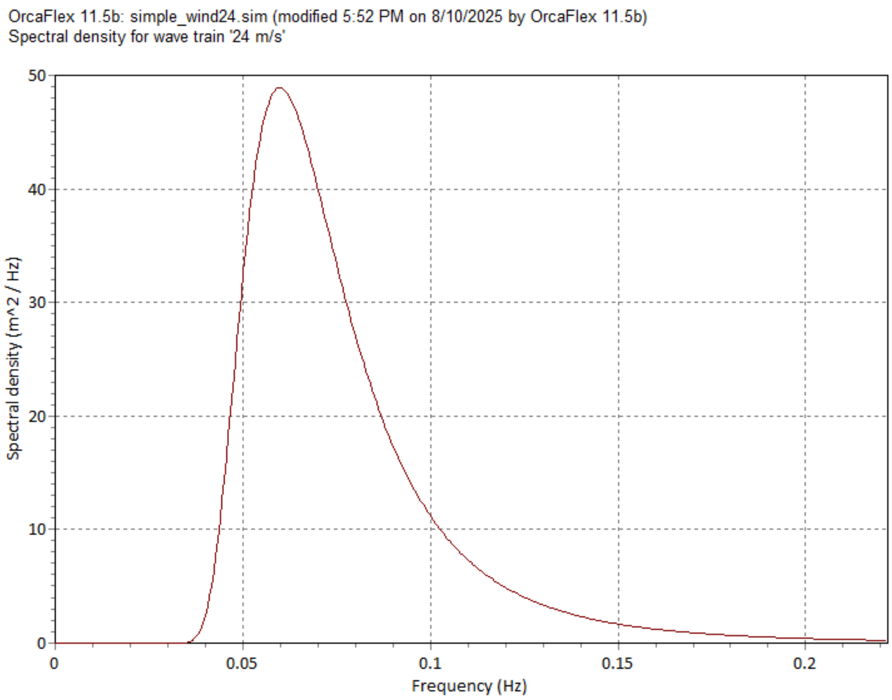

Figure 3.14: ISSC spectrum example ($H_s = 5.72$ m, $T_p = 16.7$ s).

3.3 Post-Processing of Tower-Top Response

The post-processing of numerical results follows an analogous workflow for both models (beam-based and diffraction-based). Tower-top accelerations in the global x and y directions are exported from *OrcaFlex* and transformed into the frequency domain using a Fast Fourier Transform (FFT). The FFT provides the spectral density of the response and allows the identification of dominant peaks associated with structural modes and harmonic excitations (e.g. 1P/3P). This step is standard in operational modal analysis (OMA) practice, as emphasised by Devriendt et al. [54] and Zahid et al. [51], where frequency-domain decomposition is a first tool for mode identification under ambient excitation.

To refine the spectral estimate and remove harmonic interference, the acceleration outputs are then passed into a dedicated MATLAB filtering routine (see Appendix X). This function applies a band-pass filter between user-defined bounds. The filter implements the strategy recommended in OMA literature [48], where selective frequency-windowing is considered essential to isolate structural peaks from periodic turbine harmonics.

In this work, a 10% frequency band was chosen around each identified mode. This band is sufficiently narrow to exclude the broad 3P harmonic content while retaining stochastic excitation of the structural mode. However, in cases where a mode frequency is too close to the 3P harmonic band, the peak cannot be unambiguously distinguished. Following the approach discussed by Kim et al. [52], the next available structural mode was then selected instead. This ensures that resonance interaction with harmonics is not misinterpreted as a structural property.

The adopted procedure thus combines the basic FFT approach with targeted band-pass filtering to remove harmonic content. As noted in advanced OMA reviews [48, 51], such filtering is a prerequisite before applying more sophisticated techniques (e.g. stochastic subspace identification) and provides a robust estimate.

Example workflow: Obtaining the fore–aft coupled frequency

To illustrate the modelling procedure, consider the case of the vessel model in scenario C (seed 1) with a wind speed of 14 m/s. Once the *OrcaWave* setup is complete (application of the external stiffness matrix, global inertia properties, and hydrodynamic parameters), the selected sea state is defined by the prescribed wave spectrum. Running the frequency-domain analysis produces the following hydrodynamic outputs:

- **Load RAOs** — amplitude and phase for each of the six degrees of freedom (DOFs), at each analysed wave period;
- **Displacement RAOs** — motion response amplitude and phase per DOF, again as a function of period;
- **Wave drift QTFs** — second-order transfer functions, providing one value per DOF per period analysed;
- **Added-mass and radiation-damping coefficients** — a 6×6 matrix for each period analysed.

These results are typically exported as tables but can also be visualised directly within the software. Representative graphical outputs are shown in Figures 3.15–3.17, displaying the evolution of RAOs, drift forces, and hydrodynamic coefficients across the wave periods analysed.

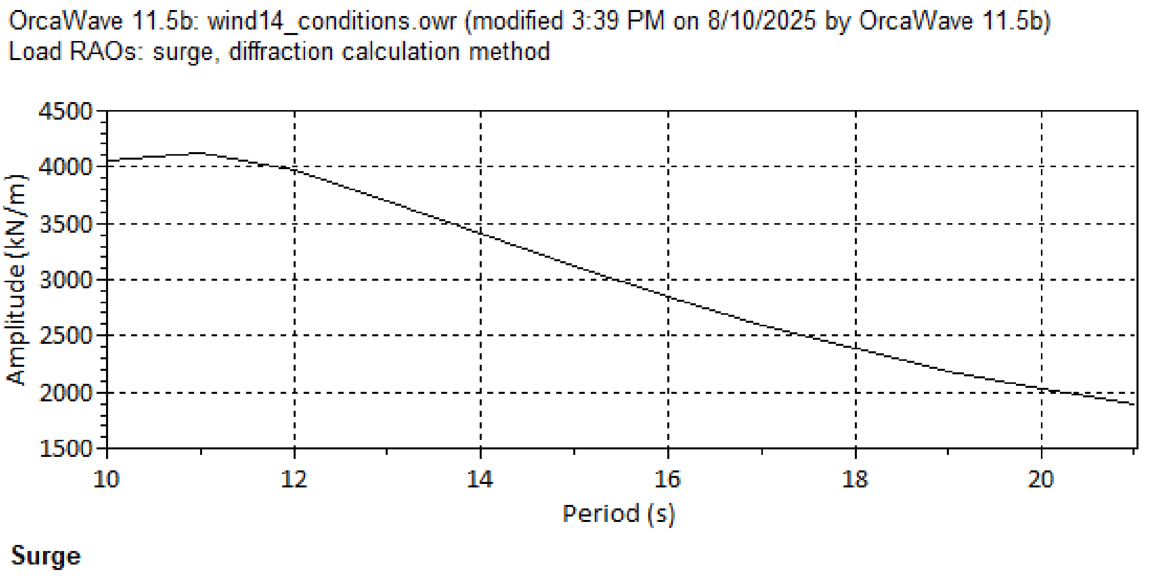

Figure 3.15: Example load RAO amplitude output for the vessel model (Surge).

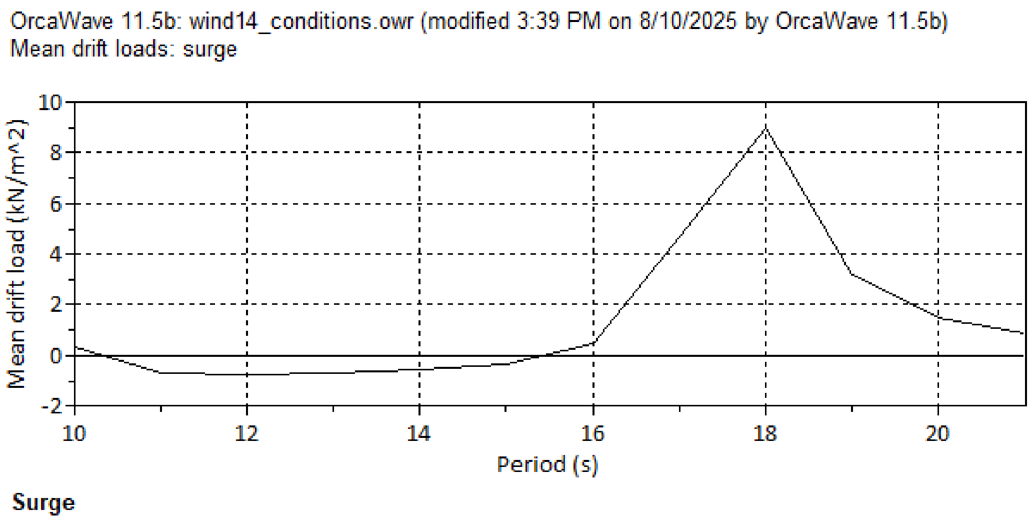

Figure 3.16: Example wave drift QTFs from *OrcaWave* (Surge).

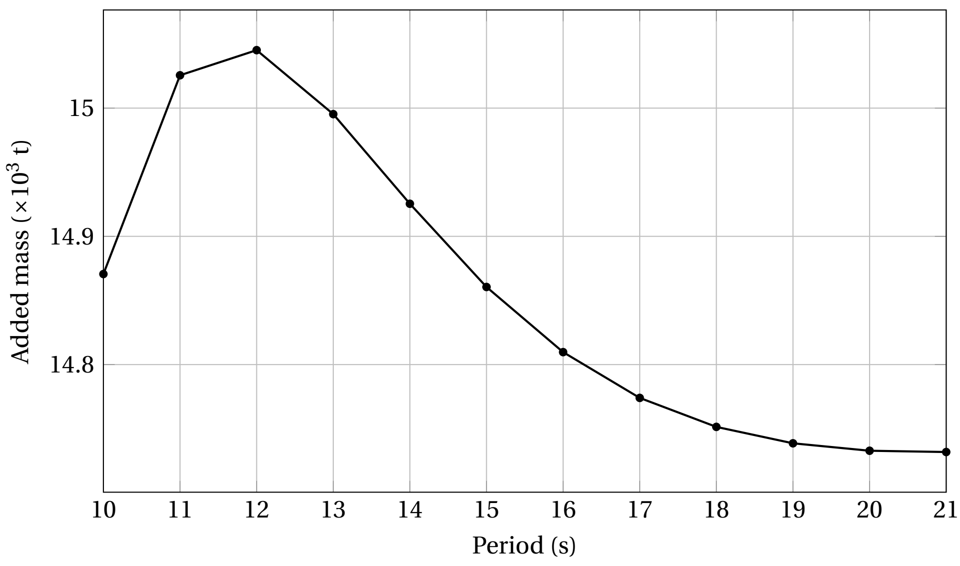

Figure 3.17: Example added-mass coefficients across wave periods (Heave–Heave).

The hydrodynamic results from *OrcaWave* are then imported into the vessel object in *OrcaFlex*, completing the setup of the vessel model. At this point, the model is ready for coupled analysis. For the beam-based model, this is the stage where the workflow begins, since its hydrodynamic description is directly defined through Morison elements.

The first step in *OrcaFlex* is to run a **statics analysis**, ensuring equilibrium of the mooring system and hydrostatics before proceeding. Once the static solution is verified, a **dynamic analysis** is performed to capture the platform–tower–rotor response under combined wind and wave loading.

From this simulation, both time-domain and frequency-domain outputs can be collected. In particular, the tower-top accelerations in the fore–aft direction (x) are recorded, and their evolution is shown in Figures 3.18 and 3.19.

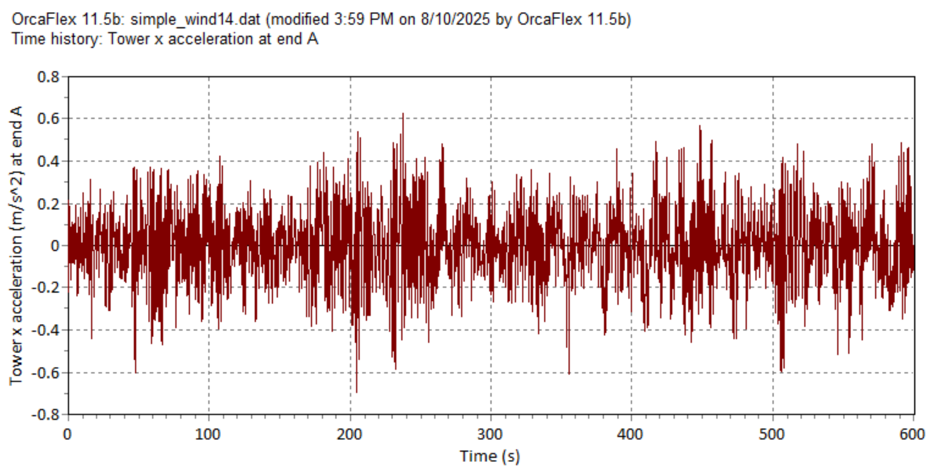

Figure 3.18: Time-domain response of tower-top fore–aft acceleration.

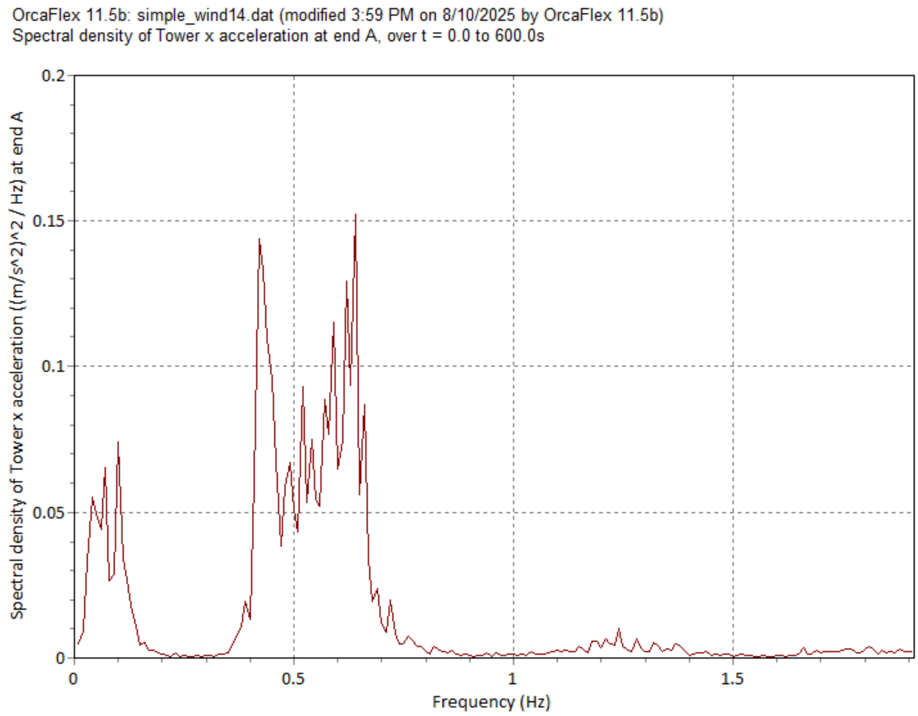

Figure 3.19: Frequency-domain response (FFT) of tower-top fore–aft acceleration.

The spectral density of the tower-top acceleration in the x-direction (fore–aft) for Scenario C at $U = 14\mathrm{m/s}$ (seed1) exhibits three dominant peaks. The first peak appears at very low frequencies ($f < 0.1$ Hz). This response is attributed to slow-drift motions of the semisubmersible platform, driven by second-order difference-frequency wave drift forces. Although the tower top motion is measured, these slow oscillations are primarily platform-dominated and reflect the coupling between the floater and the tower response. Such components are expected from the QTF-based loads included in the vessel model and are consistent with the natural periods of surge, sway, and yaw previously identified in modal analysis.

The second peak, located near $f \approx 0.4$ Hz, corresponds to the first tower fore–aft bending mode. This frequency falls within the range predicted by the Campbell diagram for the OC4 semisubmersible, where the fundamental tower mode lies around 0.40–0.43 Hz under coupled conditions. The detection of this peak demonstrates the ability of the post-processing pipeline to recover the structural dynamics of interest directly from operational response data, despite the coexistence of aerodynamic and hydrodynamic excitations.

Finally, the third peak is found at approximately $f \approx 0.6$ Hz. This is consistent with the expected 3P rotor harmonic, arising from the periodic passage of the three blades past the tower. At this wind speed, the rotor operates at about 11–12rpm, which translates to a 3P excitation in the range 0.55–0.60 Hz. This harmonic is well documented in the literature as a critical source of forced vibration in floating wind turbines, and its presence here highlights the importance of filtering procedures. As discussed earlier, if the tower mode is too close to the 3P excitation, identification becomes challenging; in such cases, either filtering techniques or selecting the next available mode becomes necessary to ensure accurate modal parameter estimation.

In addition to the tower-top response, Figures 3.20, 3.21, and 3.22 illustrate the behaviour of the main shaft rotational speed, the blade pitch angle, and the generated electrical power for Scenario C at $U = 14$ m/s (seed 1). These quantities are mainly governed by the turbine's control systems and the variability of the turbulent inflow. The shaft speed reflects the generator torque control, the pitch angle shows the activity of the blade pitch regulation, and the power output provides a global indicator of the aerodynamic–hydrodynamic coupling under operational conditions.

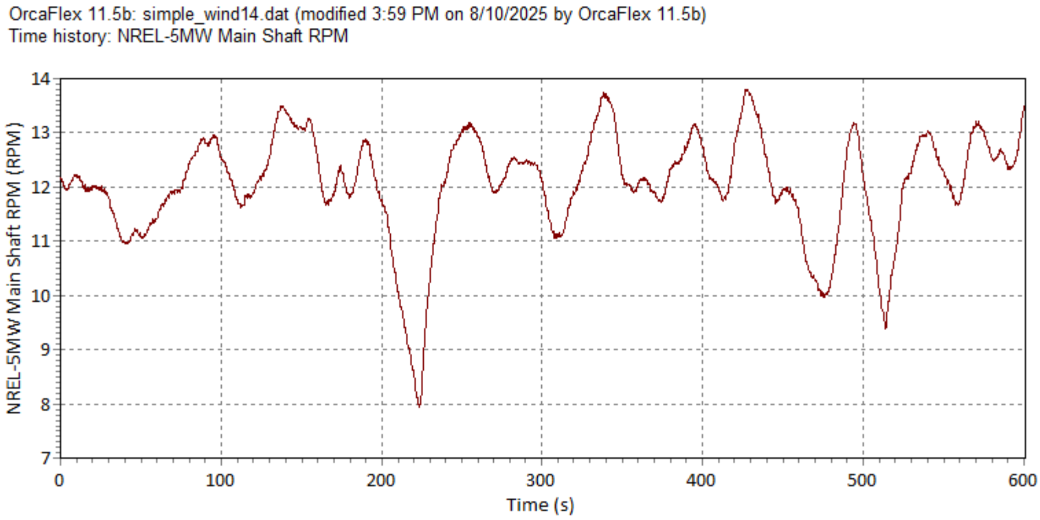

Figure 3.20: Main shaft rotational speed for Scenario C at $U = 14$ m/s (seed 1).

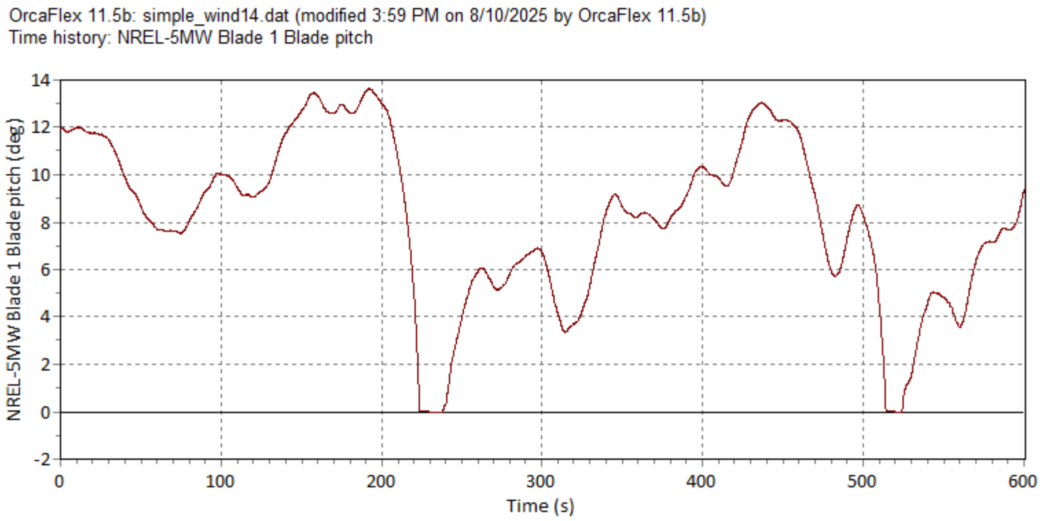

Figure 3.21: Blade pitch angle for Scenario C at $U = 14$ m/s (seed 1).

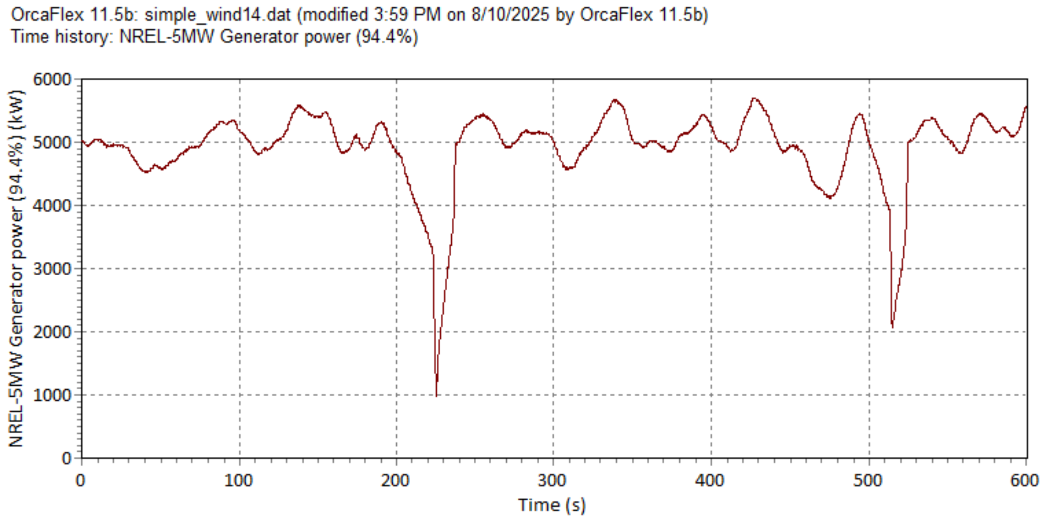

Figure 3.22: Electrical power output for Scenario C at $U = 14$ m/s (seed 1).

As expected, these signals exhibit large variance due to turbulence, and consistent modal features are not usually extracted from them. Nonetheless, they provide useful qualitative context: the rotational speed plot indicates the frequency range in which 1P and 3P harmonics may appear, the pitch response shows how the controller reacts to wind fluctuations, and the power output demonstrates the combined effect of these dynamics on overall turbine performance.

Moving into the 10% band–filter around the identified peak at approximately 0.42 Hz, the MATLAB filtering procedure was applied to isolate the response of interest. Figure 3.23 illustrates the frequency-domain signal after filtering, from which the fore–aft tower mode is established.

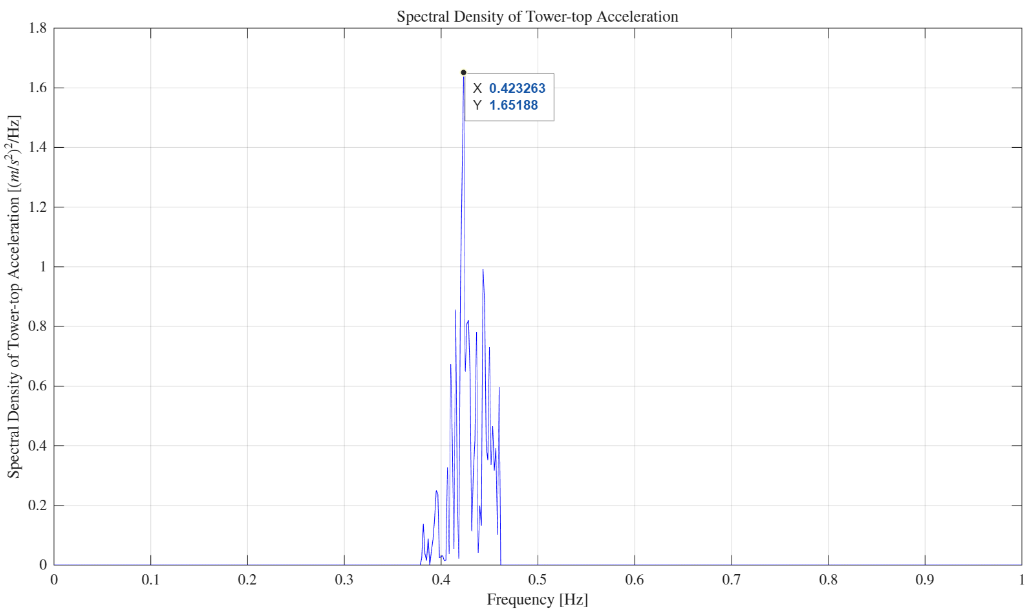

Figure 3.23: Example of 10% band-pass filtering around 0.42 Hz applied to the tower-top fore–aft acceleration. The filtered peak allows the identification of the corresponding structural mode.

This workflow was repeated for all identified frequencies. For side–side motion, the same process was applied using the y-direction tower-top acceleration as input to the filter.

3.3.1 HAWC2 Reference Simulations

To provide an industry benchmark, the aeroelastic code HAWC2 (Horizontal Axis Wind turbine simulation Code 2) was employed. HAWC2 is widely used in both research and certification contexts for modelling the aero–hydro–servo–elastic response of wind turbines. It solves the nonlinear, coupled equations of motion in the time domain, using a multibody representation of the turbine and incorporating blade element momentum (BEM) aerodynamics, dynamic stall models, structural flexibility, and user-defined control systems. Hydrodynamic loads can be included for floating platforms, along with mooring models, enabling a full-system representation [99].

The hydrodynamic formulation in HAWC2 is based on Morison-type load models applied to slender elements. Each column, pontoon, or mooring segment is represented as a beam element, and the hydrodynamic loads are computed as distributed forces per unit length using added-mass and quadratic drag terms [100]. This is analogous to the line elements used in OrcaFlex, where the Morison equation is also applied to represent viscous and inertial forces. Hydrostatic restoring is included through buoyancy on the wetted elements, while second-order wave loads (e.g., drift) can be approximated but are less commonly treated in standard HAWC2 workflows compared to diffraction-based tools like OrcaWave.

In this work, HAWC2 was used to simulate the NREL 5 MW turbine on the OC4 semisubmersible, under the same environmental conditions as Scenario C. The objective is not to reproduce every modelling detail within HAWC2, but rather to use its results as a reference for comparison with the OrcaFlex-based beam and vessel models. The Campbell diagrams extracted from HAWC2 allow direct comparison of modal trends with wind speed, providing additional validation of the operational modal analysis procedure.

Chapter 4

Discussion of Results

The analysis begins with the fundamental dynamic properties of the structure. Two complementary approaches are considered: the free decay tests, and the chirp excitation tests. In this work, the free decay procedure consists of attaching a winch at the tower top, imposing a prescribed offset, and releasing the structure from rest. The subsequent unforced motion is recorded to identify natural frequencies in the active degrees of freedom.

The chirp excitation explores the structural response under a broadband external forcing, mapping out the frequency response and highlighting resonance modes. The results of these approaches are compared with each other to ensure internal consistency of the model. Subsequently, the obtained natural frequencies are placed in context with values reported in the literature for floating semisubmersible wind platforms, thereby establishing both validation and relevance for the following environmental load analyses.

4.1 Under linear chirp excitation

A linear chirp provides a broadband probe of the structure's lateral dynamics. It sweeps the forcing frequency from f_1 to f_2 in a single test, exposing resonances and nonlinear behaviour. This makes it a practical preliminary step before environmental load cases.

The input force was implemented as a discretised linear chirp with 5000 steps between $t = 50$ s and $t = 550$ s. The excitation amplitude was set to 20 kN, and the instantaneous frequency swept linearly from $f_1 = 0.3$ Hz to $f_2 = 0.8$ Hz. Figure 4.1 shows the imposed force profile in OrcaFlex, where the increasing density of oscillations with time reflects the frequency rise across the sweep.

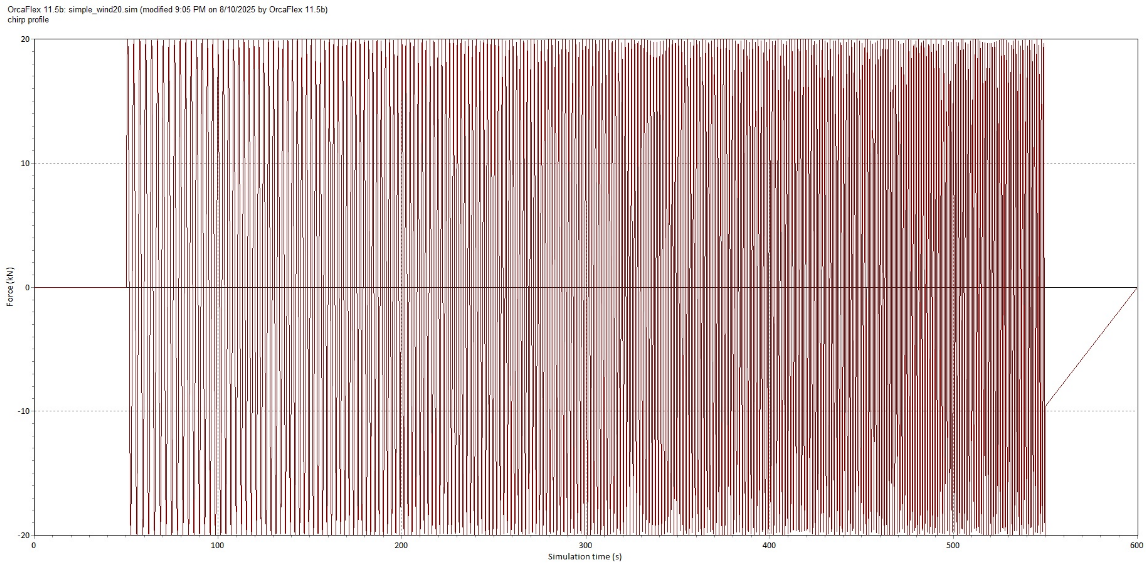

Figure 4.1: Chirp load profile applied in OrcaFlex, discretised in 5000 steps from 50 s to 550 s with amplitude 200 kN.

4.1.1 Chirp excitation results

The chirp excitation was applied at the nacelle in the global x-direction, corresponding to the fore–aft response of the tower. The structural response was monitored through the top-tower accelerations. Figures 4.2 and 4.3 present the x-acceleration time histories for the beam model and the vessel model, respectively, illustrating the build-up and resonance response as the excitation frequency swept from 0.3 Hz to 0.8 Hz.

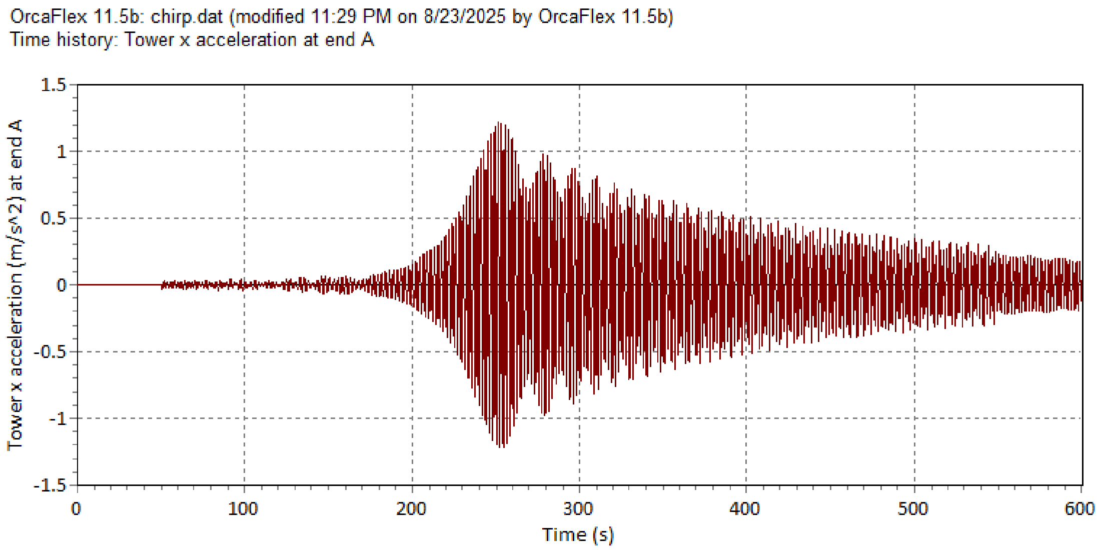

Figure 4.2: x-acceleration response at top tower for the beam model under chirp excitation.

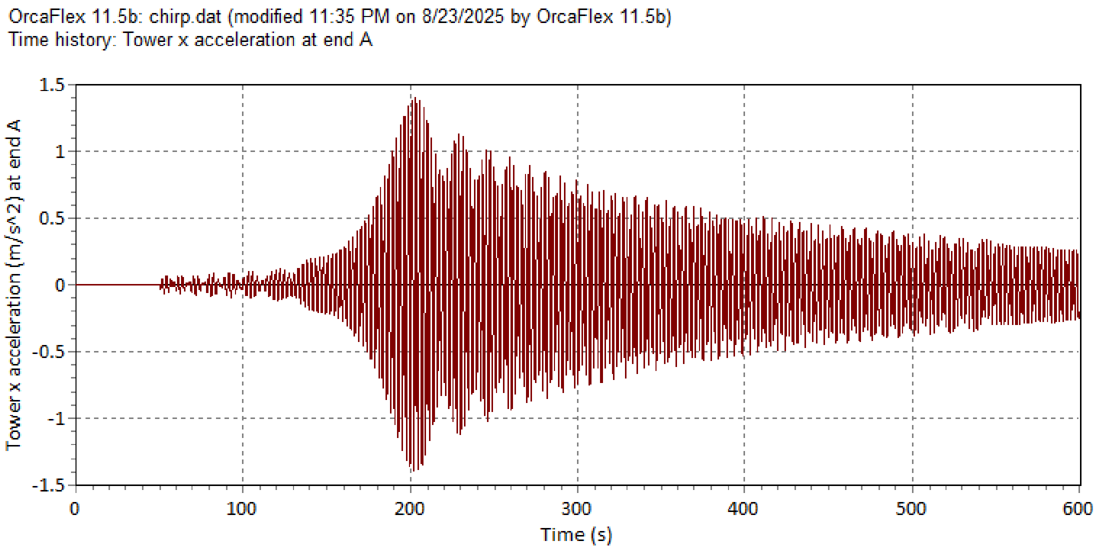

Figure 4.3: x-acceleration response at top tower for the vessel model under chirp excitation.

Peak identification in the frequency domain provides the estimates of the first fore–aft (FA) and side-to-side (SS) natural frequencies. These are summarised in Table 4.1, alongside values reported in the literature for semisubmersible floating wind turbines. The relative error with respect to literature values is also included, confirming that both models fall within the expected range.

Table 4.1: First FA and SS natural frequencies from chirp excitation compared with literature values for the OC4 DeepCWind semisubmersible.

Mode	Beam model [Hz]	Vessel model [Hz]	Literature [Hz] [52, 101]
Fore–aft (FA)	0.480	0.428	0.40–0.44
Side-to-side (SS)	0.480	0.430	0.40–0.44

The spectral density of the nacelle x-acceleration under chirp excitation is shown in Figure 4.4. A distinct and sharp resonance peak is observed at approximately 0.43 Hz, which corresponds to the first fore–aft bending mode. The absence of environmental loading (no waves, current, or turbulent wind) results in an exceptionally clean frequency response, with a single narrowband peak and negligible background energy across the spectrum. This clarity confirms the robustness of the chirp method for isolating natural frequencies prior to introducing stochastic excitations.

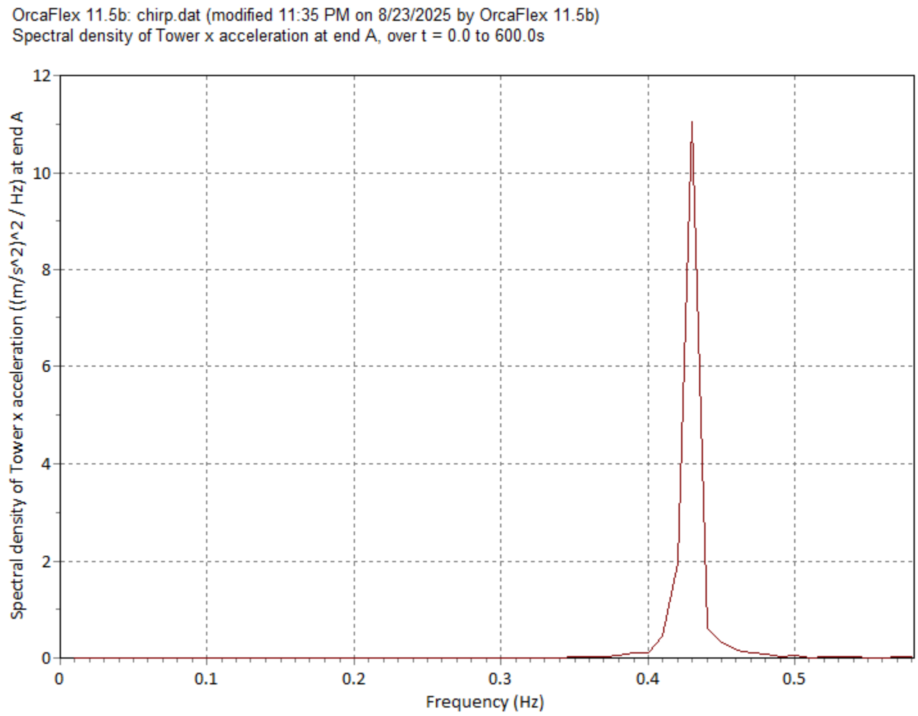

Figure 4.4: Spectral density of nacelle x-acceleration under chirp excitation (vessel model). The clean peak at ~0.43 Hz reflects the first fore–aft bending mode, facilitated by the absence of waves, current, and wind.

4.2 Winch release test: purpose and setup

The winch release procedure was implemented as a means to excite the fundamental lateral modes of the tower through a prescribed displacement. A winch element was connected between the nacelle and a fixed point, and a pre-tension was applied during the static stage to impose a horizontal offset of the tower top (Figure 4.5). At the start of the dynamic stage, the winch was released, removing all external forcing and allowing the structure to oscillate freely. This corresponds to a free-decay test, in which the system response is governed only by its stiffness and damping properties.

The advantage of this approach is that it yields direct estimates of the natural frequencies in the fore–aft and side-to-side directions. In principle, effective damping ratios could also be extracted from the decay of successive oscillations using the logarithmic decrement method [102]:

$$\delta = \frac{1}{n}\ln\left(\frac{x_0}{x_n}\right), \qquad \zeta = \frac{\delta}{\sqrt{4\pi^2+\delta^2}}, \tag{4.1}$$

where x_0 and x_n are amplitudes of oscillation separated by n cycles. However, damping estimation was not an objective of this work, and therefore the focus here remains solely on the identification of the natural frequencies.

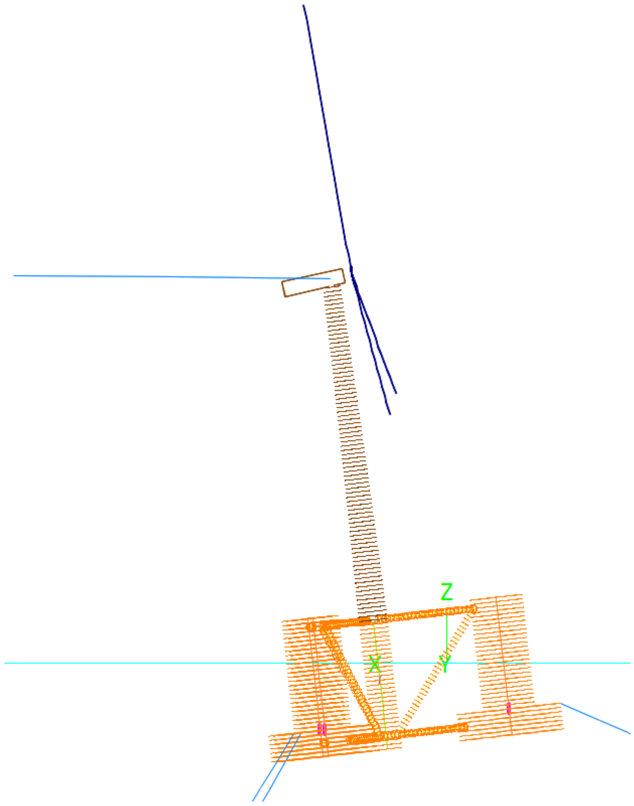

Figure 4.5: Implementation of the winch release test. The tower is offset by pre-tension during the static stage and released at the start of the dynamic analysis, producing a free-decay response.

The dynamic x displacement at the nacelle for the winch release test is presented in Figure 4.6. In OrcaFlex, the *dynamic* coordinate represents the motion relative to the initial static equilibrium configuration, excluding rigid offsets and gravity contributions. This isolates the oscillatory displacement induced by the release.

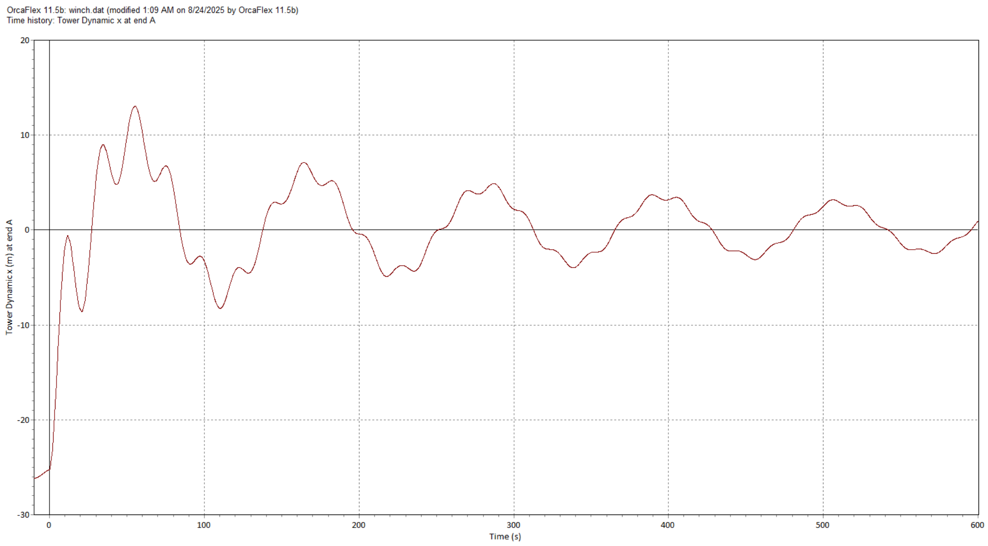

Figure 4.6: Dynamic x displacement of the nacelle during the winch release test (beam model).

During the static stage ($t < 0$), the tower top is held in an offset position by the pre-tensioned winch. At $t = 0$ s the winch is released, after which the tower undergoes free oscillations around its equilibrium. The response is characterised by large initial amplitudes that gradually decay, illustrating the combined effect of hydrodynamic and structural damping. The oscillation period is consistent with the first lateral natural frequency identified in the chirp test (~ 0.43 Hz). After approximately 600 s, the motion has nearly decayed to equilibrium, confirming that the system dissipates the initial disturbance as expected.

The natural frequencies obtained from the winch release tests are summarised in Table 4.2. Both the beam and vessel models yield clear estimates of the first fore–aft and side–to–side modes, which are compared against literature values for the OC4 DeepCWind semisubmersible. The results are consistent with those obtained in the chirp excitation test, as expected since both approaches are designed to capture the same fundamental structural modes.

Table 4.2: First FA and SS natural frequencies obtained from winch release tests compared with literature values for the OC4 DeepCWind semisubmersible [52, 101].

Mode	Beam model [Hz]	Vessel model [Hz]	Literature [Hz]
Fore–aft (FA)	0.479	0.430	0.40–0.44
Side–to–side (SS)	0.480	0.430	0.40–0.44

4.3 Environmental conditions: Scenario A

The first coupled fore–aft (FA) and side–to–side (SS) frequencies under turbulent wind excitation are shown in Figures 4.7 and 4.8, alongside the rotor 3P frequency. The corresponding numerical values are summarised in Table 4.3.

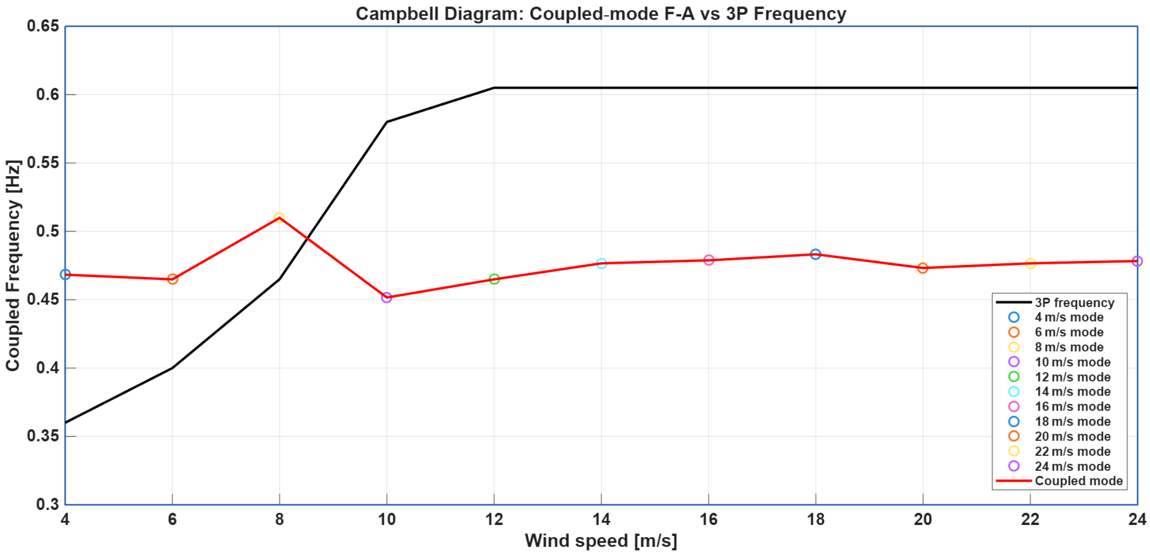

Figure 4.7: Campbell diagram for fore–aft mode under Scenario A. Coupled mode frequency compared against rotor 3P.

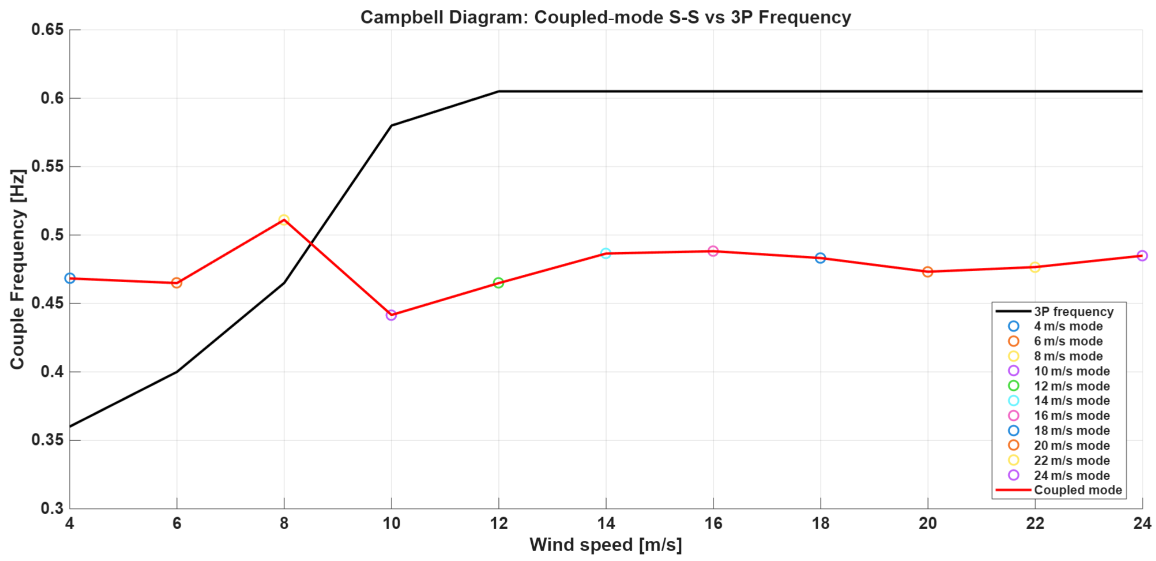

Figure 4.8: Campbell diagram for side–to–side mode under Scenario A. Coupled mode frequency compared against rotor 3P.

Table 4.3: Coupled FA and SS frequencies obtained under Scenario A, compared with rotor 3P frequency.

Wind Speed [m/s]	FA [Hz]	SS [Hz]	3P [Hz]
4	0.4683	0.4683	0.36
6	0.4649	0.4649	0.40
8	0.5099	0.5111	0.465
10	0.4516	0.4416	0.58
12	0.4649	0.4649	0.605
14	0.4766	0.4865	0.605
16	0.4788	0.4882	0.605
18	0.4832	0.4832	0.605
20	0.4732	0.4732	0.605
22	0.4766	0.4766	0.605
24	0.4783	0.4849	0.605

The Campbell diagrams show that the first lateral frequencies remain broadly stable across the wind speed range, with values mostly centred near 0.47–0.49 Hz (except at 8 and 10 m/s). A noticeable shift occurs at 8 m/s, where both FA and SS frequencies increase to approximately 0.51 Hz. The proximity between the structural frequencies and the 3P excitation is most critical around this region, where the 3P line crosses through the coupled mode. Beyond 10 m/s, the 3P frequency stabilises around 0.605 Hz, remaining above the first lateral frequencies and thus reducing the risk of direct resonance. The results are consistent between FA and SS, as expected for the nearly symmetric tower geometry.

A notable deviation is observed at 8 m/s, where both the FA and SS coupled frequencies rise above the trend to approximately 0.51 Hz. This shift is not interpreted as a physical change in the structural dynamics, but rather as an artefact of the frequency identification process. At this operating point the structural modes lie very close to the rotor 3P frequency, and the filtering applied during the post-processing likely suppressed or distorted the true peak, leading to the apparent offset. While this effect could in principle be reduced with case-specific adjustments, the methodology of this work applies a uniform filtering and identification procedure across all wind speeds in order to ensure consistency. The important outcome is therefore the overall stability of the coupled FA and SS frequencies around 0.47–0.49 Hz, with the 8 m/s deviation regarded as a local artefact rather than a genuine modal shift.

For each wind case in Scenario A, the rotor speed was obtained from a post-processed channel that converts the nacelle main shaft angular velocity (an OrcaFlex output) into shaft revolutions per minute (RPM). This was implemented with a simple script that calculates RPM = $60\omega/2\pi$, where ω is the angular velocity in rad/s. The corresponding 3P frequency is then

$$f_{3P} = 3 \times \frac{\text{RPM}}{60}. \tag{4.2}$$

Figure 4.9 shows the processed shaft speed at 8 m/s, where the response settles around 9.3 RPM with only small amplitude fluctuations. This corresponds to a 3P frequency of approximately 0.465 Hz, consistent with the values used in the Campbell diagrams. In contrast, other cases (e.g. Fig. 3.20) exhibit higher variability in the RPM signal, which broadens the apparent 3P content.

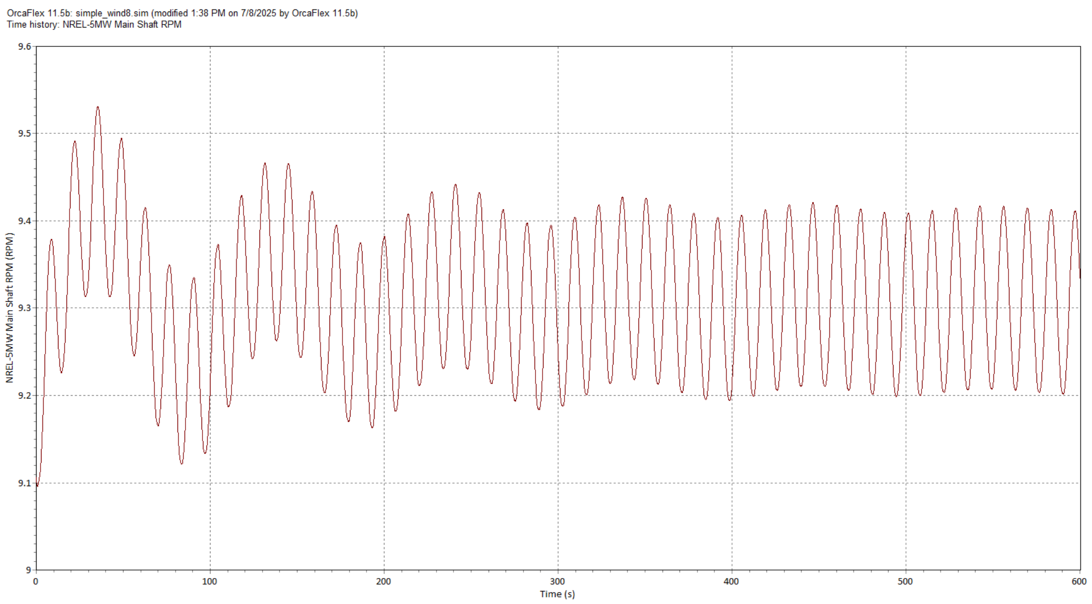

Figure 4.9: Main shaft rotational speed at 8 m/s wind case, post-processed from shaft angular velocity. The signal stabilises around 9.3 RPM, corresponding to a 3P frequency of 0.465 Hz. Vertical axis: main shaft rotational speed [RPM], range 9-9.6. Horizontal axis: time [s], range 0–600.

For consistency, the mean values obtained in Scenario A were adopted as the reference 3P frequencies in Scenarios B and C as well, since the steady rotor speed is set primarily by the controller and is only weakly affected by waves or currents.

4.4 Environmental conditions: Scenario B

Scenario B corresponds to the condition of laminar wind combined with irregular waves. The Campbell diagram for the fore–aft (FA) coupled mode is shown in Figure 4.10, where both the beam and vessel models are compared for three turbulence seeds across the full wind speed range. The rotor 3P frequency is included for reference. The corresponding numerical values are compiled in Tables 4.4 and 4.5.

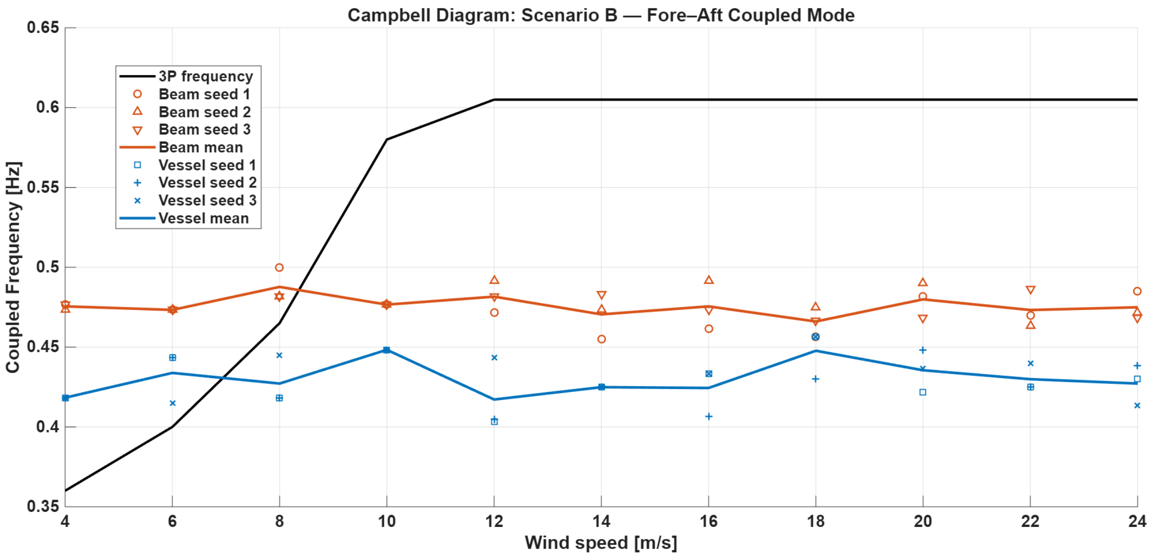

Figure 4.10: Campbell diagram for Scenario B showing fore–aft coupled mode frequencies. Markers correspond to three seeds per wind speed; solid lines indicate mean values for the beam and vessel models. The black line denotes the rotor 3P frequency.

Table 4.4: Fore–aft (FA) coupled frequencies obtained with the beam model for Scenario B (laminar wind with irregular waves). Results are shown for three turbulence seeds per wind speed, including the mean (μ) and standard deviation (σ).

Wind [m/s]	Seed 1 [Hz]	Seed 2 [Hz]	Seed 3 [Hz]	Beam μ [Hz]	Beam σ
4	0.4766	0.4733	0.4766	0.4755	0.0016
6	0.4733	0.4733	0.4733	0.4733	0.0000
8	0.4999	0.4816	0.4816	0.4877	0.0085
10	0.4766	0.4766	0.4766	0.4766	0.0000
12	0.4716	0.4916	0.4816	0.4816	0.0082
14	0.4549	0.4733	0.4833	0.4705	0.0117
16	0.4616	0.4916	0.4733	0.4755	0.0123
18	0.4566	0.4749	0.4666	0.4660	0.0075
20	0.4816	0.4899	0.4682	0.4799	0.0089
22	0.4699	0.4632	0.4866	0.4732	0.0096
24	0.4849	0.4716	0.4683	0.4749	0.0071

Table 4.5: Fore–aft (FA) coupled frequencies obtained with the vessel model for Scenario B (laminar wind with irregular waves). Results are shown for three turbulence seeds per wind speed, including the mean (μ), standard deviation (σ), and the mean difference $\Delta\mu$ relative to the beam model.

Wind [m/s]	Seed 1 [Hz]	Seed 2 [Hz]	Seed 3 [Hz]	Vessel μ [Hz]	Vessel σ	$\Delta\mu$ [Hz]
4	0.4183	0.4183	0.4183	0.4183	0.0000	0.0572
6	0.4433	0.4433	0.4149	0.4338	0.0134	0.0395
8	0.4183	0.4183	0.4449	0.4272	0.0126	0.0605
10	0.4483	0.4483	0.4483	0.4483	0.0000	0.0283
12	0.4033	0.4049	0.4433	0.4172	0.0185	0.0644
14	0.4249	0.4249	0.4249	0.4249	0.0000	0.0456
16	0.4333	0.4066	0.4333	0.4244	0.0128	0.0511
18	0.4566	0.4299	0.4566	0.4477	0.0127	0.0183
20	0.4216	0.4483	0.4366	0.4355	0.0110	0.0444
22	0.4249	0.4249	0.4399	0.4299	0.0067	0.0433
24	0.4299	0.4383	0.4133	0.4272	0.0103	0.0477

Several consistent trends can be observed from these results:

- **Beam vs. vessel:** The vessel model systematically predicts lower FA coupled frequencies than the beam model, with an average difference of approximately 0.046 Hz (about 9–10%). This behaviour reflects the additional compliance and hydrodynamic added mass introduced by the floating support structure.

- **Seed variability:** The beam model shows minimal scatter across seeds ($\sigma < 0.01$ Hz in most cases), whereas the vessel model exhibits higher variability (σ up to 0.018 Hz). This suggests that wave excitation introduces additional uncertainty in mode identification, especially around 12 m/s.

- **Wind-speed trend:** The beam frequencies remain in a narrow band (0.466–0.488 Hz), confirming their independence from operating conditions. The vessel values span 0.417–0.448 Hz, also without a strong monotonic trend, but showed higher deviations.

- **3P crossing region:** Around 6 to 12 m/s the behaviour of the coupled modes is strongly influenced by the proximity to the rotor 3P frequency. At 8 and 12 m/s the difference between beam and vessel reaches about 0.06 Hz, while at 10 m/s it is smaller (around 0.03 Hz), showing that the offset is not uniform. The shaft speed analysis indicates that the 3P line is expected to intersect the vessel mode near 7 m/s and the beam mode closer to 8 m/s. Since 7 m/s was not simulated, the vessel identification is already challenged at 8 m/s, where 3P and the structural frequency remain close. Importantly, 3P is not a single fixed value but spans a range due to operational variability, so the notion of "intersection" should not be seen as a black-and-white condition. Although larger absolute differences between beam and vessel means are observed at higher wind speeds (14 to 24 m/s), the interaction with 3P in this lower range provides additional context for interpreting the scatter in the results.

The Campbell diagram for the side–side (SS) coupled mode is now shown in Figure 4.11. The corresponding numerical values are compiled in Tables 4.6 and 4.7.

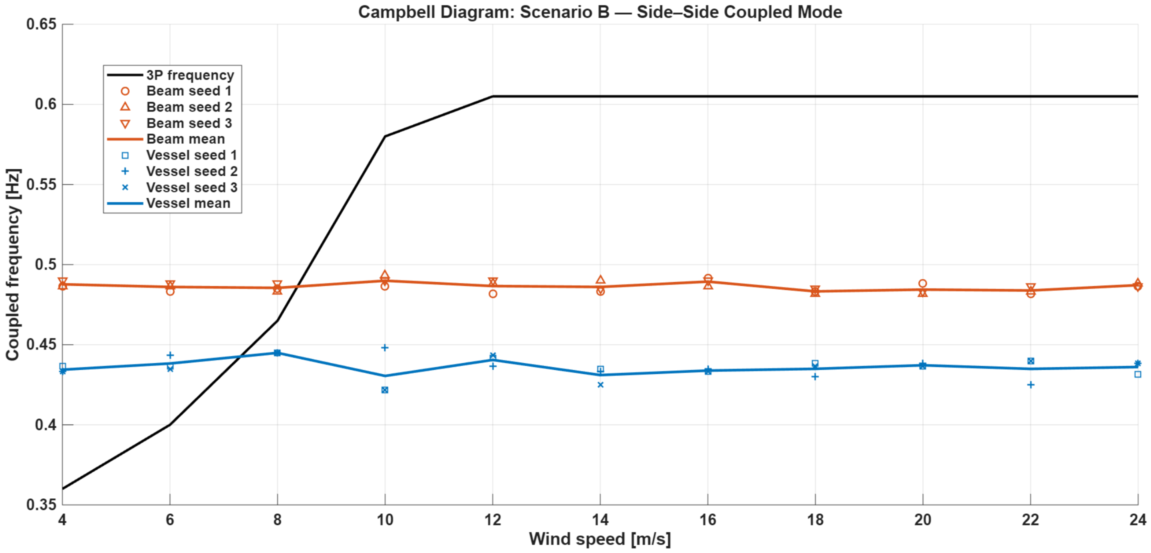

Figure 4.11: Campbell diagram for Scenario B showing side–side coupled mode frequencies.

Table 4.6: Side–side (SS) coupled frequencies obtained with the beam model for Scenario B (laminar wind with irregular waves). Results are shown for three turbulence seeds per wind speed, including the mean (μ) and standard deviation (σ).

Wind [m/s]	Seed 1 [Hz]	Seed 2 [Hz]	Seed 3 [Hz]	Beam μ [Hz]	Beam σ
4	0.4866	0.4866	0.4899	0.4877	0.0019
6	0.4833	0.4866	0.4882	0.4860	0.0025
8	0.4849	0.4832	0.4883	0.4855	0.0026
10	0.4866	0.4933	0.4899	0.4899	0.0034
12	0.4816	0.4883	0.4899	0.4866	0.0044
14	0.4833	0.4899	0.4849	0.4860	0.0036
16	0.4916	0.4866	0.4899	0.4894	0.0020
18	0.4833	0.4816	0.4849	0.4833	0.0014
20	0.4883	0.4816	0.4833	0.4844	0.0035
22	0.4816	0.4833	0.4866	0.4838	0.0025
24	0.4866	0.4883	0.4866	0.4872	0.0010

Table 4.7: Side–side (SS) coupled frequencies obtained with the vessel model for Scenario B (laminar wind with irregular waves). Results are shown for three turbulence seeds per wind speed, including the mean (μ), standard deviation (σ), and the mean difference $\Delta\mu$ relative to the beam model.

Wind [m/s]	Seed 1 [Hz]	Seed 2 [Hz]	Seed 3 [Hz]	Vessel μ [Hz]	Vessel σ	$\Delta\mu$ [Hz]
4	0.4366	0.4333	0.4333	0.4344	0.0019	0.0533
6	0.4366	0.4433	0.4349	0.4383	0.0036	0.0477
8	0.4449	0.4449	0.4449	0.4449	0.0000	0.0406
10	0.4216	0.4483	0.4216	0.4305	0.0129	0.0594
12	0.4416	0.4366	0.4433	0.4405	0.0028	0.0461
14	0.4349	0.4333	0.4249	0.4310	0.0044	0.0550
16	0.4333	0.4349	0.4333	0.4338	0.0007	0.0556
18	0.4383	0.4299	0.4366	0.4349	0.0035	0.0484
20	0.4366	0.4383	0.4366	0.4372	0.0008	0.0472
22	0.4399	0.4249	0.4399	0.4349	0.0071	0.0489
24	0.4316	0.4383	0.4383	0.4361	0.0031	0.0511

The side–side behaviour does not fully mirror the fore–aft response. Because the wave direction is aligned with 0°, the loading acts predominantly in the fore–aft direction and the side–side response shows less dependence on wind speed. The beam frequencies remain stable around 0.48–0.49 Hz with reduced scatter, while the vessel frequencies are consistently lower, around 0.43–0.44 Hz, with $\Delta\mu$ values in the 0.04–0.06 Hz range. Interestingly, in the vessel model the 10 m/s case exhibits the highest standard deviation, whereas in the fore–aft mode this was the point of lowest variability, highlighting how the two lateral directions respond differently to the same operating condition.

The most relevant feature in this case, however, is the very small separation between seeds for both models. This result is fully expected given that both the wind and wave excitations act primarily in the x–axis, leaving the side–side response less perturbed by environmental variability. It is nevertheless noteworthy that, despite the different excitation mechanisms, the mean values obtained for side–side remain very close to those of the fore–aft mode.

4.5 Environmental conditions: Scenario C

Scenario C combines turbulent wind with irregular waves, representing the most realistic operating condition in this study. For consistency with the previous sections, the 3P reference employed in the Campbell diagrams is the one derived from Scenario A (mean shaft-speed values), acknowledging that turbulence broadens the effective 3P band.

Figure 4.12 presents the FA Campbell diagram comparing the beam and vessel models across the full wind-speed range and three seeds per case (solid lines denote seed-wise means). Tables 4.8–4.9 compile the FA coupled-mode frequencies for the beam and vessel models (three seeds per wind speed). The vessel table also reports the mean difference $\Delta\mu$ relative to the beam.

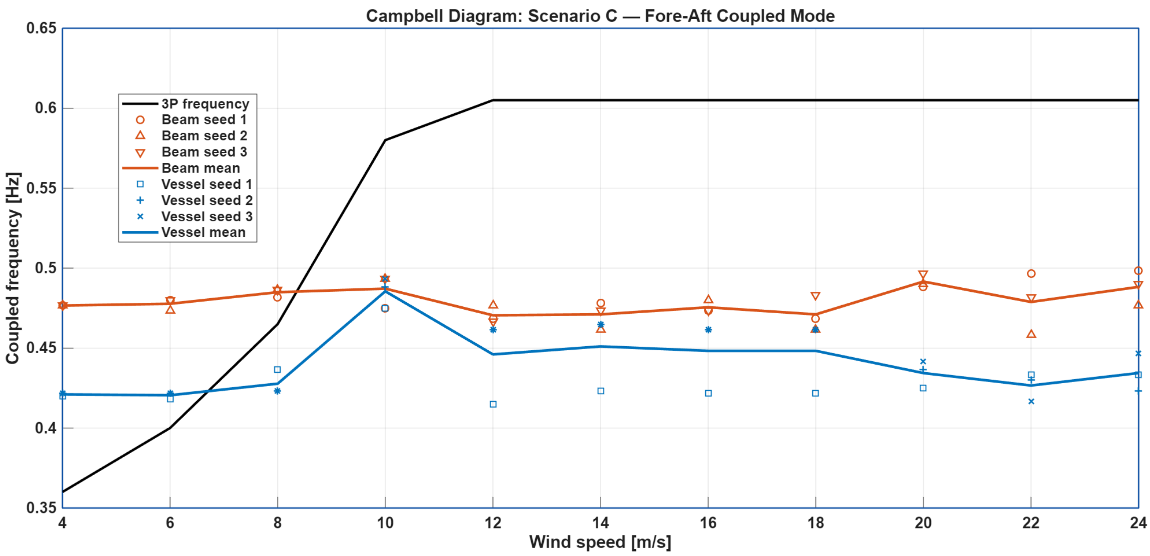

Figure 4.12: Campbell diagram for Scenario C showing fore–aft (FA) coupled mode frequencies.

Table 4.8: Scenario C — FA coupled frequencies (beam model): three seeds per wind speed, with mean (μ) and standard deviation (σ).

Wind [m/s]	Seed 1 [Hz]	Seed 2 [Hz]	Seed 3 [Hz]	Beam μ [Hz]	Beam σ
4	0.4766	0.4766	0.4766	0.4766	0.0000
6	0.4799	0.4733	0.4799	0.4777	0.0038
8	0.4816	0.4866	0.4866	0.4849	0.0029
10	0.4749	0.4933	0.4933	0.4872	0.0106
12	0.4683	0.4766	0.4666	0.4705	0.0044
14	0.4783	0.4616	0.4733	0.4711	0.0083
16	0.4733	0.4799	0.4733	0.4755	0.0032
18	0.4683	0.4616	0.4833	0.4711	0.0110
20	0.4883	0.4899	0.4966	0.4916	0.0035
22	0.4966	0.4583	0.4816	0.4788	0.0154
24	0.4983	0.4766	0.4899	0.4883	0.0087

Table 4.9: Scenario C — FA coupled frequencies (vessel model): three seeds per wind speed, with mean (μ), standard deviation (σ), and mean difference $\Delta\mu$ to the beam.

Wind [m/s]	Seed 1 [Hz]	Seed 2 [Hz]	Seed 3 [Hz]	Vessel μ [Hz]	Vessel σ	$\Delta\mu$ [Hz]
4	0.4199	0.4216	0.4216	0.4210	0.0010	0.0556
6	0.4183	0.4216	0.4216	0.4205	0.0019	0.0572
8	0.4366	0.4233	0.4233	0.4277	0.0077	0.0572
10	0.4749	0.4883	0.4933	0.4855	0.0092	0.0017
12	0.4149	0.4616	0.4616	0.4460	0.0270	0.0245
14	0.4233	0.4649	0.4649	0.4510	0.0241	0.0201
16	0.4216	0.4616	0.4616	0.4483	0.0231	0.0272
18	0.4216	0.4616	0.4616	0.4483	0.0231	0.0228
20	0.4249	0.4366	0.4416	0.4344	0.0084	0.0572
22	0.4333	0.4299	0.4166	0.4266	0.0084	0.0522
24	0.4333	0.4233	0.4466	0.4344	0.0118	0.0539

- **Beam.** The beam frequencies remain clustered around 0.48–0.49 Hz with low seed scatter, consistent with Scenarios A and B. Increased variability is observed at a few high-wind cases (e.g. 18–24 m/s), attributable to the joint action of waves and turbulence on the identification bandwidth.

- **Vessel.** The vessel frequencies are consistently lower (typically 0.42–0.45 Hz), reflecting hydrodynamic added mass and mooring compliance. Local excursions near 8–12 m/s occur when the structural mode approaches the 3P band; under turbulent inflow this interaction is broader than in Scenario B, which can transiently bias peak picking despite the uniform filtering adopted in this work.

- **Beam–vessel gap.** The mean difference $\Delta\mu$ generally lies in the 0.04–0.06 Hz range, narrowing intermittently at wind speeds where the vessel peak hardens (or the beam softens) due to wave–wind coupling. The overall offset is in line with Scenarios A and B, confirming the systematic softening introduced by the floating support.

- **3P interaction.** The 3P crossing region (around 8–10 m/s) remains the most sensitive, but turbulence spreads the rotor-harmonic content over a wider band. This explains the occasional upward/downward shifts in the identified vessel frequency without implying a permanent modal change.

An interesting behaviour is observed at 10 m/s for the vessel model, where the identified FA frequency rises significantly above the surrounding values before returning to the expected band at higher wind speeds. While the proximity to the 3P frequency can partly explain this deviation, other effects may also contribute. The increase in mean platform offset with wind speed changes the tangent stiffness of the mooring system and can temporarily raise the apparent fore–aft stiffness. However, this alone would be expected to keep the frequency higher at stronger winds, which is not observed. Instead, the effect is likely combined with the controller transition occurring around this operating point and the influence of irregular wave excitation, which together produce a local spike in the identified frequency rather than a sustained shift.

Figure 4.13 shows the SS Campbell diagram for Scenario C with the same layout. Tables 4.10–4.11 present the SS results in the same format.

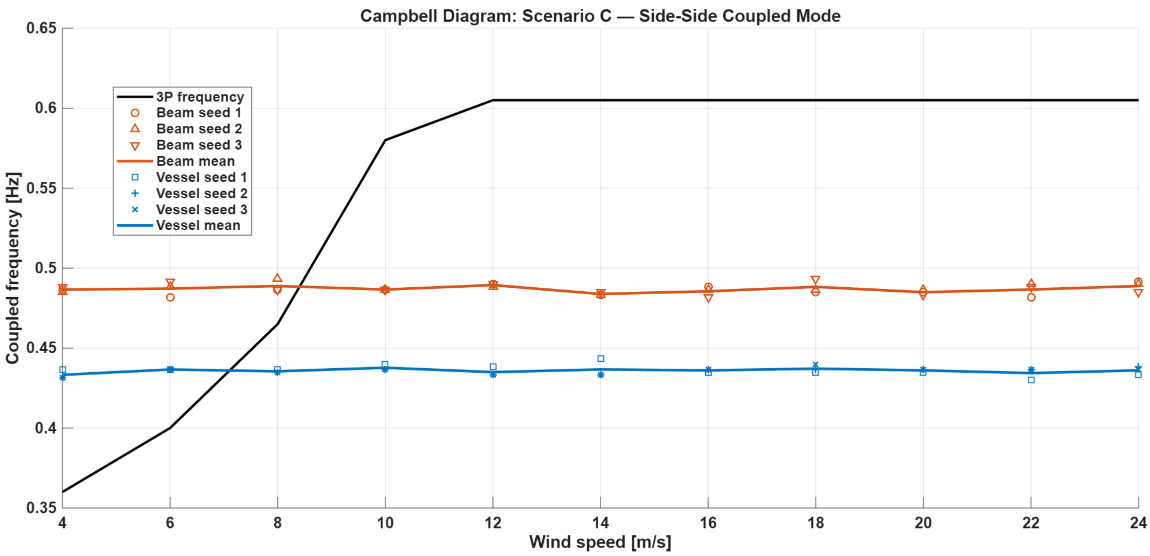

Figure 4.13: Campbell diagram for Scenario C showing side–side (SS) coupled mode frequencies. Markers correspond to three seeds per wind speed; solid lines indicate mean values for the beam and vessel models. The black line denotes the rotor 3P frequency.

The side–side behaviour in Scenario C follows the same trends already observed in Scenario B and in the fore–aft direction. The beam model remains stable around 0.48–0.49 Hz with negligible seed-to-seed scatter, while the vessel model is consistently lower, near 0.43–0.44 Hz, with similar variability. The mean offset between models stays close to 0.05 Hz, confirming the systematic softening introduced by the floating platform. Unlike the fore–aft case, no isolated anomalies appear, and the side–side frequencies evolve smoothly across the wind-speed range.

Table 4.10: Scenario C — SS coupled frequencies (beam model): three seeds per wind speed, with mean (μ) and standard deviation (σ).

Wind [m/s]	Seed 1 [Hz]	Seed 2 [Hz]	Seed 3 [Hz]	Beam μ [Hz]	Beam σ
4	0.4866	0.4849	0.4883	0.4866	0.0017
6	0.4816	0.4883	0.4916	0.4872	0.0051
8	0.4866	0.4933	0.4866	0.4888	0.0039
10	0.4866	0.4866	0.4866	0.4866	0.0000
12	0.4899	0.4883	0.4899	0.4894	0.0009
14	0.4833	0.4833	0.4849	0.4838	0.0010
16	0.4883	0.4866	0.4816	0.4855	0.0034
18	0.4849	0.4866	0.4933	0.4883	0.0043
20	0.4849	0.4866	0.4833	0.4850	0.0017
22	0.4816	0.4899	0.4883	0.4866	0.0035
24	0.4916	0.4899	0.4849	0.4888	0.0034

Table 4.11: Scenario C — SS coupled frequencies (vessel model): three seeds per wind speed, with mean (μ), standard deviation (σ), and mean difference $\Delta\mu$ to the beam.

Wind [m/s]	Seed 1 [Hz]	Seed 2 [Hz]	Seed 3 [Hz]	Vessel μ [Hz]	Vessel σ	$\Delta\mu$ [Hz]
4	0.4366	0.4316	0.4316	0.4333	0.0029	0.0533
6	0.4366	0.4366	0.4366	0.4366	0.0000	0.0506
8	0.4366	0.4349	0.4349	0.4355	0.0010	0.0533
10	0.4399	0.4366	0.4366	0.4377	0.0019	0.0489
12	0.4383	0.4333	0.4333	0.4350	0.0029	0.0544
14	0.4433	0.4333	0.4333	0.4366	0.0058	0.0472
16	0.4349	0.4366	0.4366	0.4360	0.0010	0.0495
18	0.4349	0.4366	0.4399	0.4371	0.0025	0.0512
20	0.4349	0.4366	0.4366	0.4360	0.0010	0.0490
22	0.4299	0.4366	0.4366	0.4344	0.0039	0.0522
24	0.4333	0.4383	0.4366	0.4361	0.0025	0.0527

4.5.1 Comparison with HAWC2

The fore–aft (FA) coupled mode frequencies obtained for Scenario C are shown in Figure 4.14. The results include the beam and vessel models across three turbulence seeds per wind speed, as well as the HAWC2 reference. As before, the rotor 3P frequency is overlaid for context. The corresponding HAWC2 values are compiled in Table 4.12.

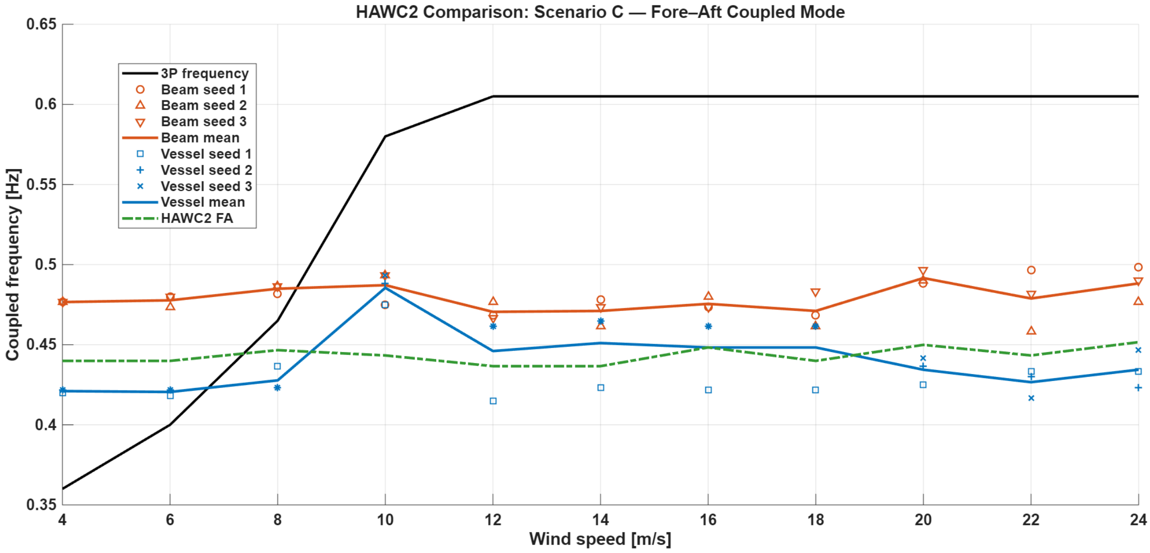

Figure 4.14: Campbell diagram for Scenario C showing fore–aft (FA) coupled mode frequencies. Seed results and mean curves are shown for both the beam and vessel models, while the HAWC2 reference is included as an additional line.

Table 4.12: Scenario C — HAWC2 fore–aft (FA) coupled frequencies across wind speeds.

Wind [m/s]	HAWC2 FA [Hz]
4	0.4399
6	0.4399
8	0.4466
10	0.4433
12	0.4366
14	0.4366
16	0.4483
18	0.4399
20	0.4499
22	0.4433
24	0.4516

Several mechanisms may explain the slope observed in HAWC2 and its difference relative to the counterparts:

- **Blade DOFs unlocked:** In HAWC2 the blade degrees of freedom are active, which can introduce additional dynamics into the signal. This may add noise or mode interaction such that the identified peak does not correspond purely to the tower fore–aft mode, contributing to the observed upward trend.
- **Hydro–moor compliance:** The vessel model includes added mass and nonlinear mooring stiffness, which can counteract or mask any aerodynamic stiffening, explaining the flatter trend relative to beam and HAWC2.
- **Model input discrepancies:** Minor structural/aero databases (airfoil polars, tower/blade properties) not being perfectly matched between codes.

- **Seed variability:** Only one HAWC2 seed was simulated; additional seeds would likely broaden the range around the current trend and provide a more representative mean.

The side–side (SS) coupled mode for Scenario C is shown in Figure 4.15, including the beam, vessel, and HAWC2 results. The beam and vessel values were presented previously; the HAWC2 frequencies are now included in Table 4.13 for direct comparison.

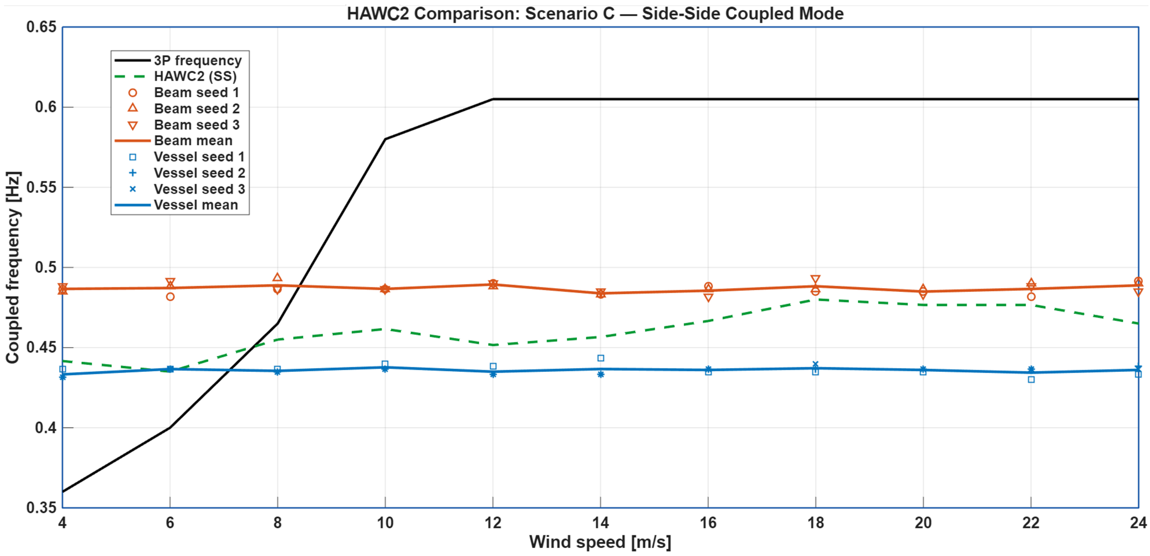

Figure 4.15: Campbell diagram for Scenario C showing side–side (SS) coupled mode frequencies. Seed results and mean curves are shown for both the beam and vessel models, while the HAWC2 reference is included as an additional line.

Table 4.13: Scenario C — HAWC2 side–side (SS) coupled frequencies across wind speeds.

Wind [m/s]	HAWC2 SS [Hz]
4	0.4416
6	0.4350
8	0.4550
10	0.4616
12	0.4516
14	0.4566
16	0.4666
18	0.4800
20	0.4766
22	0.4766
24	0.4650

The HAWC2 results, show a distinct trend from the previous Scenario C ones: the SS frequency begins near 0.44 Hz at low wind speeds and gradually increases to nearly 0.48 Hz by 18–20 m/s before softening slightly at 24 m/s. This mild upward slope with wind speed is not clearly visible in either the beam or vessel results, which remain essentially flat. A plausible explanation, adding to some of the differences already mentioned in the fore-aft analysis, is that HAWC2 captures more of the aerodynamic stiffening mechanisms as the effective wind loading increases, especially through the tower–blade–pitch interactions, whereas the OrcaFlex implementations (beam and vessel) may not represent these effects with the same fidelity.

This divergence highlights that while both OrcaFlex models are consistent and internally stable, their lateral modes do not exhibit the same sensitivity to mean aerodynamic loading as HAWC2. The comparison reinforces the expectation that different modelling tools capture different aspects of the coupled aero-hydro-servo-elastic response, and that systematic offsets should be interpreted in light of these modelling assumptions.

Chapter 5

Conclusions and Future Work

5.1 Conclusions

This thesis investigated the coupled dynamic response of a semisubmersible FOWT using two modelling strategies: a simplified beam model and a diffraction-based vessel model. The comparative analysis across all scenarios consistently showed that the vessel model predicts a slightly *softer* first tower-bending mode, yielding frequencies in the 0.43–0.44 Hz band, compared to the 0.48–0.49 Hz band of the beam model. This systematic offset reflects the added hydrodynamic compliance captured by the vessel model, including radiation damping and added mass effects, which are absent in the beam formulation. Three environmental scenarios were considered: A (regular waves with steady wind), B (irregular waves with steady wind), and C (irregular waves with turbulent wind), representing increasing excitation complexity.

Despite this difference, both models produced consistent results across the three scenarios. The identified frequency bands remained relatively tight, with the beam model showing very little scatter between different seeds, while the vessel model was more sensitive to stochastic variability. The robustness of the beam model thus makes it attractive for studies where repeatability is important and detailed hydrodynamic data are not available.

Challenges arose in identifying structural modes due to overlapping excitations. The $3P$ rotor harmonic frequently masked or coincided with the tower mode, especially at moderate wind speeds, complicating spectral analysis and occasionally leading to ambiguous peak identification. The mooring system contributes additional stiffness and damping to the platform, and its own tension–compliance modes can interact with the global dynamics. While the first tower-bending mode is largely decoupled from mooring stretch, higher-frequency coupling effects, such as those involving heave–pitch motions or line tensioning—could still alter the response near the tower's natural frequency. In this study, no clear evidence of a distinct mooring-induced mode within the 0.4–0.5 Hz band was identified, but the moorings nevertheless influenced the effective stiffness and damping captured by the vessel model.

Finally, the progression from Scenario A to Scenario C highlighted the influence of environmental complexity. Whereas Scenario A produced sharp and clean peaks, the addition of irregular waves in Scenario B increased background energy, and turbulence in Scenario C further blurred the modal signatures, making frequency identification more uncertain.

Overall, the study shows that the beam model offers simplicity, stability, and robustness, while the vessel model provides greater physical fidelity at the cost of higher input requirements and greater sensitivity to stochastic excitation. The choice between the two thus involves a trade-off between practicality and accuracy.

5.2 Future Work

Building on the insights gained from this research, several avenues for future work are recommended to enhance the analysis of FOWT coupled dynamics and to address the challenges identified:

- **Mesh sensitivity of structural models:** The present work employed standard discretisations for the tower and beam models. Performing systematic mesh sensitivity studies would help quantify the influence of element resolution on the identified frequencies and ensure that the results are not affected by numerical artefacts.
- **Advanced modal identification techniques:** While band-pass filtering was effective in mitigating harmonic interference, more robust approaches should be explored. In particular, time-domain methods such as Covariance-Driven Stochastic Subspace Identification (SSI-COV) are widely used in low-frequency applications and may provide clearer separation of structural modes from rotor harmonics.
- **Broader stochastic sampling:** Increasing the number of seeds for both wind and wave realisations would improve statistical confidence in the identified frequency bands. This applies both to the OrcaFlex simulations and to reference models such as HAWC2. Extending the comparison framework to include OpenFAST would further strengthen the validation across different aero–hydro–servo–elastic codes.
- **Control strategy assessment:** The influence of turbine control settings on the coupled dynamics warrants further investigation. Different pitch or torque control strategies may alter the interaction between rotor harmonics and structural modes, and could potentially be tuned to mitigate modal interference.
- **Directional effects:** Finally, the present study focused on aligned wind and wave directions. Future work should evaluate misaligned conditions, where wind and wave directions differ, as well as nonzero headings. These cases are highly relevant for offshore environments and may significantly affect both the excitation spectra and the platform's dynamic response.
- **Extended hydrodynamic studies:** This dissertation did not aim to perform an in-depth hydrodynamic characterisation, but rather to conduct a modal analysis and compare two modelling strategies. Nevertheless, future work could focus on a more detailed hydrodynamic investigation. For instance, analysing the infinite added mass and its impact on the coupled dynamics would complement the present results and broaden the understanding of the physical mechanisms at play.

Appendix A

Appendices

A.1 Spectral normalisation of PM and JONSWAP

Let $S(f)$ [m^{2}s] denote the one-sided variance density as a function of linear frequency f [Hz]. The zeroth spectral moment is $m_0 = \int_0^\infty S(f)\,df$. The significant wave height satisfies $H_s \approx 4\sqrt{m_0}$, so a consistent normalisation requires

$$m_0 = \int_0^\infty S(f)\,df = \frac{H_s^2}{16}. \tag{A.1}$$

PM spectrum Using the dimensional form

$$S_{\mathrm{PM}}(f) = \alpha_{\mathrm{PM}}\,\frac{g^2}{(2\pi)^4}\,f^{-5}\exp\left[-\frac{5}{4}\left(\frac{f_p}{f}\right)^4\right], \tag{A.2}$$

with gravitational acceleration g and peak frequency f_p (often denoted f_m), equivalence with the H_s-normalised form

$$S_{\mathrm{PM}}(f) = \frac{5}{16}\,H_s^2\,f_p^4\,f^{-5}\exp\left[-\frac{5}{4}\left(\frac{f_p}{f}\right)^4\right] \tag{A.3}$$

implies

$$\boxed{\alpha_{\mathrm{PM}} = \frac{5}{16}\,H_s^2\,f_p^4\,\frac{(2\pi)^4}{g^2}}. \tag{A.4}$$

Integrating (A.3) gives $m_0 = \frac{5}{16}H_s^2\int_0^\infty x^{-5}\exp\left[-\frac{5}{4}x^{-4}\right]dx = \frac{5}{16}H_s^2\cdot\frac{1}{5} = \frac{H_s^2}{16}$, which satisfies (A.1) [59, 55, 71].

JONSWAP spectrum A convenient form is

$$S_{\mathrm{JON}}(f) = \alpha_{\mathrm{J}}\,\frac{g^2}{(2\pi)^4}\,f^{-5}\exp\left[-\frac{5}{4}\left(\frac{f_p}{f}\right)^4\right]\gamma^{\,b(f)}, \tag{A.5}$$

with peak-enhancement factor γ and peak-shape function

$$b(f) = \exp\left[-\frac{1}{2\sigma^2}\left(\frac{f}{f_p}-1\right)^2\right], \qquad \sigma = \begin{cases}\sigma_1, & f \le f_p,\\ \sigma_2, & f > f_p,\end{cases} \tag{A.6}$$

where typical values are $\sigma_1 \approx 0.07$ and $\sigma_2 \approx 0.09$ [59, 72]. Define the dimensionless integral

$$I_J(\gamma,\sigma_1,\sigma_2) = \int_0^\infty x^{-5}\exp\left[-\frac{5}{4}x^{-4}\right]\gamma^{b(x)}\,dx, \qquad x = \frac{f}{f_p}. \tag{A.7}$$

Then

$$m_0 = \alpha_\mathrm{J}\,\frac{g^2}{(2\pi)^4}\,f_p^{-4}\,I_J(\gamma,\sigma_1,\sigma_2). \tag{A.8}$$

Imposing (A.1) yields the required scaling

$$\boxed{\alpha_\mathrm{J} = \frac{H_s^2}{16}\,\frac{(2\pi)^4}{g^2}\,f_p^4\,\frac{1}{I_J(\gamma,\sigma_1,\sigma_2)}}. \tag{A.9}$$

Limit $\gamma = 1$: JONSWAP reduces to PM Setting $\gamma = 1$ gives $\gamma^{b(x)} \equiv 1$ and $I_J(\gamma{=}1,\sigma_1,\sigma_2) = \int_0^\infty x^{-5}\exp\left[-\frac{5}{4}x^{-4}\right]dx = 1/5$. With (A.9), this makes $\alpha_\mathrm{J} = \alpha_\mathrm{PM}$ from (A.4), so $S_\mathrm{JON}(f)$ reduces exactly to the PM spectrum with the same H_s normalisation [55, 59].

Symbols used in this appendix $S(f)$ one-sided variance density spectrum; f linear frequency; f_p peak frequency; H_s significant wave height; g gravitational acceleration; $\alpha_\mathrm{PM}, \alpha_\mathrm{J}$ scale parameters for PM and JONSWAP; γ peak-enhancement factor; $b(f)$ peak-shape function; σ_1, σ_2 spectral widths below and above f_p; m_0 zeroth spectral moment; I_J dimensionless integral defined in (A.7).

Appendix B

MATLAB Post-Processing Scripts

B.1 Band-Pass Cleaning Filter

The function below band-passes tower-top signals and returns the filtered time history together with the cleaned PSD (see Sec. 3.3).

```
function [sig_filt,freq,PSDclean] = cleanfilter(low,high,sig)
% VESTAS WIND SYSTEMS A/S (2025)
% Band-pass cleans a signal using FFT windowing.
% INPUTS:
% low, high : frequency bounds [Hz]
% sig(:,1) : time vector [s]
% sig(:,2) : signal (e.g., tower-top acceleration)
% OUTPUTS:
% sig_filt : [t, x_filtered]
% freq : frequency vector [Hz]
% PSDclean : cleaned one-sided PSD (windowed)

t_sim = sig(:,1);
dat_sens= sig(:,2);
n = length(t_sim);
dt = t_sim(n)-t_sim(n-1);

X = fft(dat_sens);
PSD = X.*conj(X)/n;
freq= 1/(dt*n)*(0:n-1);

% keep only [low,high] band
keep = (freq>low) & (freq<high);
Xclean = zeros(size(X));
Xclean(keep) = X(keep);
PSDclean = zeros(size(PSD));
PSDclean(keep) = PSD(keep);

```

```
% back to time domain
dat_sens_clean = real(ifft(Xclean));
sig_filt = zeros(n,2);
sig_filt(:,1) = t_sim;
sig_filt(:,2) = dat_sens_clean;

% optional quick-look plot (comment out for batch use)
% figure; plot(freq,PSDclean); xlim([0 1]); grid on;
% xlabel('Frequency [Hz]'); ylabel('PSD [arb.]'); title('Cleaned PSD');
end
```

Listing B.1: cleanfilter.m

Bibliography

[1] Global Wind Energy Council. *Offshore Wind Policy*. Accessed: 2025-08-27. 2024. URL: https://www.gwec.net/policy/offshorewind#:~:text=Offshore%20wind%20will%20be%20a,on%20a%20massive%20scale%20to.

[2] DHI Group. *Floating Wind Farms: A New Dimension to Offshore Wind Energy*. Accessed: 2025-08-27. 2024. URL: https://blog.dhigroup.com/floating-wind-farms-a-new-dimension-to-offshore-wind-energy/#:~:text=Traditionally%2C%20wind%20turbines%20typically%20stand,per%20MWh%20in%20contrast%20to.

[3] Marta de Castro, Marina Costa, and Celso Ferreira. "Offshore Renewable Energy in Portugal: Current Status and Future Perspectives". In: *Sustainability* 15.3 (2023), pp. 1–20. DOI: 10.3390/su15032428. URL: https://www.mdpi.com/.

[4] WindFloat Atlantic. *WindFloat Atlantic Project*. Accessed: 2025-08-27. 2020. URL: https://www.windfloat-atlantic.com/.

[5] Royal HaskoningDHV. *Portugal Targets 10 GW Offshore Wind Capacity by 2030*. Accessed: 2025-08-27. 2023. URL: https://www.haskoning.com.

[6] Reuters. *Portugal sets 10 GW offshore wind target and prepares first auction*. Accessed: 2025-08-27. 2023. URL: https://www.reuters.com.

[7] U. S. Department of Energy. *The Inside of a Wind Turbine*. https://www.energy.gov/eere/wind/inside-wind-turbine-0. Accessed: 2025-02-25.

[8] CM Vivek, P Gopikrishnan, R Murugesh, and R Raja Mohamed. "A review on vertical and horizontal axis wind turbine". In: *International Research Journal of Engineering and Technology (IRJET)* 4.4 (2017), pp. 247–250.

[9] Muhammad Mahmood Aslam Bhutta, Nasir Hayat, Ahmed Uzair Farooq, Zain Ali, Sh. Rehan Jamil, and Zahid Hussain. "Vertical axis wind turbine – A review of various configurations and design techniques". In: *Renewable and Sustainable Energy Reviews* 16.4 (2012), pp. 1926–1939. ISSN: 1364-0321. DOI: https://doi.org/10.1016/j.rser.2011.12.004. URL: https://www.sciencedirect.com/science/article/pii/S136403211100596X.

[10] Mohamed Ebeed. "Enhancement Protection and Operation of The Doubly Fed Induction Generator During Grid Fault". PhD thesis. Apr. 2013. DOI: 10.13140/RG.2.2.16718.25925.

[11] Zhenyu Wang, Wei Tian, and Hui Hu. "A Comparative study on the aeromechanic performances of upwind and downwind horizontal-axis wind turbines". In: *Energy Conversion and Management* 163 (2018), pp. 100–110.

[12] Hu Zhou and Decheng Wan. “Numerical investigations on the aerodynamic performance of wind turbine: Downwind versus upwind configuration”. In: *Journal of Marine Science and Application* 14.1 (Mar. 2015), pp. 61–68. ISSN: 1993-5048. DOI: 10.1007/s11804-015-1295-9. URL: https://doi.org/10.1007/s11804-015-1295-9.

[13] Amina Bensalah, Georges Barakat, and Yacine Amara. “Electrical Generators for Large Wind Turbine: Trends and Challenges”. In: *Energies* 15 (Sept. 2022). DOI: 10.3390/en15186700.

[14] U. S. Department of Energy. *Experts Predict 50% Lower Wind Costs Than They Did in 2015*. https://www.energy.gov/eere/wind/articles/experts-predict-50-lower-wind-costs-they-did-2015-0. Accessed: 2025-02-25. 2021.

[15] Mehmet Bilgili, Abdulkadir Yasar, and Erdogan Simsek. “Offshore wind power development in Europe and its comparison with onshore counterpart”. In: *Renewable and Sustainable Energy Reviews* 15.2 (2011), pp. 905–915. ISSN: 1364-0321. DOI: https://doi.org/10.1016/j.rser.2010.11.006. URL: https://www.sciencedirect.com/science/article/pii/S1364032110003758.

[16] Vinod Kumar, R.L. Shrivastava, and S.P. Untawale. “Fresnel lens: A promising alternative of reflectors in concentrated solar power”. In: *Renewable and Sustainable Energy Reviews* 44 (2015), pp. 376–390. ISSN: 1364-0321. DOI: https://doi.org/10.1016/j.rser.2014.12.006. URL: https://www.sciencedirect.com/science/article/pii/S1364032114010582.

[17] International Renewable Energy Agency (IRENA). *Renewable Power Generation Costs in 2023*. Accessed: 2025-02-25. Abu Dhabi: International Renewable Energy Agency, 2024. ISBN: 978-92-9260-621-3. URL: https://www.irena.org/Publications/2024/Sep/Renewable-Power-Generation-Costs-in-2023.

[18] Belachew Desalegn, Desta Gebeyehu, Bimrew Tamrat, Tassew Tadiwose, and Ababa Lata. “Onshore versus offshore wind power trends and recent study practices in modeling of wind turbines’ life-cycle impact assessments”. In: *Cleaner Engineering and Technology* 17 (2023), p. 100691. ISSN: 2666-7908. DOI: https://doi.org/10.1016/j.clet.2023.100691. URL: https://www.sciencedirect.com/science/article/pii/S2666790823000964.

[19] Shifeng Wang, Sicong Wang, and Jinxiang Liu. “Life-cycle green-house gas emissions of onshore and offshore wind turbines”. In: *Journal of Cleaner Production* 210 (2019), pp. 804–810. ISSN: 0959-6526. DOI: https://doi.org/10.1016/j.jclepro.2018.11.031. URL: https://www.sciencedirect.com/science/article/pii/S0959652618334310.

[20] P. H. Dahl, P. G. Reinhall, A. N. Popper, M. C. Hastings, and M. A. Ainslie. “Underwater sound from pile driving, what is it and why does it matter”. In: *Acoustics Today* 11.2 (2014), pp. 18–25.

[21] Dong-Gyun Han and Jee Woong Choi. “Measurements and spatial distribution simulation of impact pile driving underwater noise generated during the construction of offshore wind power plant off the southwest coast of Korea”. In: *Frontiers in Marine Science* 8 (2022), p. 654991. DOI: 10.3389/fmars.2021.654991.

[22] Laura Botero Bolívar, Oscar A. Muñoz, Martín de Frutos, and Esteban Ferrer. “Can aerodynamic noise from large offshore wind turbines affect marine life?” In: *Unpublished manuscript* (2025). arXiv preprint available.

[23] HowStuffWorks. *How Wind Power Works.* Accessed: 10th March 2025. 2006. URL: https://science.howstuffworks.com/environmental/green-science/wind-power.html.

[24] Repsol. *How does a wind turbine work?* Accessed: 10 March 2025. 2023. URL: https://www.repsol.com/en/energy-and-the-future/future-of-the-world/wind-turbine/index.cshtml.

[25] Eugen-Vlad Năstase. "Influence of the material used to build the blades of a wind turbine on their starting conditions". In: *MATEC Web of Conferences* 112 (Jan. 2017), p. 10017. DOI: 10.1051/matecconf/201711210017.

[26] SKF. *Dancing with the wind – Pitch and yaw systems.* Accessed: 10 March 2025. 2023. URL: https://windfarmmanagement.skf.com/pitch-and-yaw-systems-dancing-with-the-wind/.

[27] Heesoo Shin, Mario Rüttgers, and Sangseung Lee. "Neural Networks for Improving Wind Power Efficiency: A Review". In: *Fluids* (Nov. 2022). DOI: 10.3390/fluids7120367.

[28] P. A. Lynn. *Onshore and Offshore Wind Energy: An Introduction.* Wiley, 2012.

[29] J. Jonkman, S. Butterfield, W. Musial, and G. Scott. *Definition of a 5-MW Reference Wind Turbine for Offshore System Development.* Technical report. NREL, 2009.

[30] Sánchez, López-Gutiérrez, Vicente Negro, and M. Dolores Esteban. "Foundations in Offshore Wind Farms: Evolution, Characteristics and Range of Use. Analysis of Main Dimensional Parameters in Monopile Foundations". In: *Journal of Marine Science and Engineering* 7 (Dec. 2019), p. 441. DOI: 10.3390/jmse7120441.

[31] M. D. Esteban, J. S. López-Gutiérrez, V. Negro, C. Matutano, F. M. García-Flores, and M. A. Millán. "Offshore Wind Foundation Design: Some Key Issues". In: *J. Energy Resour. Technol.* 137 (2014), pp. 1–6.

[32] H. K. Jacobsen, P. Hevia-Koch, and C. Wolter. "Nearshore and Offshore Wind Development: Costs and Competitive Advantage Exemplified by Nearshore Wind in Denmark". In: *Energy Sustain. Dev.* 50 (2019), pp. 91–100.

[33] International Renewable Energy Agency (IRENA). *Floating Offshore Wind Outlook.* Abu Dhabi, 2024. URL: https://www.irena.org/Publications/2024/Jul/Floating-offshore-wind-outliook.

[34] U.S. Department of Energy. *Offshore Wind Energy.* 2025. URL: https://windexchange.energy.gov/markets/offshore.

[35] Esther Dornhelm, Helene Seyr, and Michael Muskulus. "Vindby—A Serious Offshore Wind Farm Design Game". In: *Energies* 12 (Apr. 2019), p. 1499. DOI: 10.3390/en12081499.

[36] Saleh Jalbi and Subhamoy Bhattacharya. "Concept design of jacket foundations for offshore wind turbines in 10 steps". In: *Soil Dynamics and Earthquake Engineering* 139 (2020), p. 106357. ISSN: 0267-7261. DOI: https://doi.org/10.1016/j.soildyn.2020.106357. URL: https://www.sciencedirect.com/science/article/pii/S0267726120309623.

[37] E. C. Edwards, E. Ransley, and R. Simmonds. “Evolution of floating offshore wind platforms: A review of at-sea devices”. In: *Renewable and Sustainable Energy Reviews* 183 (2023), p. 113416. DOI: 10.1016/j.rser.2023.113416.

[38] Iberdrola. *Floating Offshore Wind: What Is It and How Does It Work?* https://www.iberdrola.com/innovation/floating-offshore-wind. Accessed: 2025-03-25.

[39] T. Tran, D. Kim, and J. Song. “Computational Fluid Dynamic Analysis of a Floating Offshore Wind Turbine Experiencing Platform Pitching Motion”. In: *Energies* 7.8 (2014), pp. 5011–5026. DOI: 10.3390/en7085011.

[40] *Developing a World Leading Research Program in Deepwater Offshore Wind Energy*. Tech. rep. University of Maine, 2012. URL: https://umaine.edu/epscor/wp-content/uploads/sites/25/2013/06/UMaine_DeepWind.pdf.

[41] Amy Robertson, Jason Jonkman, Mitchell Masciola, H. Song, Andrew Goupee, Andrew Coulling, and C. Luan. *Definition of the Semisubmersible Floating System for Phase II of OC4*. Tech. rep. NREL/TP-5000-60601. National Renewable Energy Laboratory, 2014. URL: https://www.nrel.gov/docs/fy14osti/60601.pdf.

[42] H. Zhao et al. “Exploring Motion Stability of a Novel Semi-Submersible Platform for Offshore Wind Turbines”. In: *Energies* 17.10 (2024). Accessed: 2025-08-13, p. 2313. DOI: 10.3390/en17102313. URL: https://www.mdpi.com/1996-1073/17/10/2313.

[43] Y. Huang, Y. Zhuang, and D. Wan. “Hydrodynamic Study and Performance Analysis of the OC4-DeepCWind Platform by CFD Method”. In: *International Journal of Computational Methods* (2020). Accessed: 2025-08-13, 2050020–1–20. URL: https://dcwan.sjtu.edu.cn/userfiles/HydrodynamicStudy-åůšåŐŇçijĽ.pdf.

[44] Wanli Yu, Piguang Wang, Mi Zhao, Renqiang Xi, and Xiuli Du. “A numerical method for evaluating the earthquake response of a 5MW OC4 semi-submersible FOWT under multidirectional excitations”. In: *Soil Dynamics and Earthquake Engineering* 196 (2025), Article 109467. DOI: 10.1016/j.soildyn.2025.109467.

[45] Pekka Ruponen, Teemu Manderbacka, and Daniel Lindroth. “On the calculation of the righting lever curve for a damaged ship”. In: *Ocean Engineering* 149 (2018), pp. 313–324. ISSN: 0029-8018. DOI: https://doi.org/10.1016/j.oceaneng.2017.12.036. URL: https://www.sciencedirect.com/science/article/pii/S0029801817307588.

[46] Carlos A. Rodríguez, Antonio Souto-Iglesias, and Carlos López-Pavón. “Hydrodynamic influence of heave plates on floating offshore wind turbines: Experimental and numerical analysis”. In: *Ocean Engineering* 249 (2022), p. 111067. DOI: 10.1016/j.oceaneng.2022.111067.

[47] Y. Zhang, X. Liu, Y. Li, J. Yang, and X. Wang. “Operational Modal Analysis of Offshore Wind Turbine Tower under Ambient Excitation”. In: *Journal of Marine Science and Engineering* 10.12 (2022), p. 1963. DOI: 10.3390/jmse10121963. URL: https://www.mdpi.com/2077-1312/10/12/1963.

[48] A. Natarajan, M. Saleem, E. Cheynet, R. Brincker, et al. “Damping identification of offshore wind turbines using OMA: a review”. In: *Wind Energy Science* 7.1 (2022), pp. 161–189. DOI: 10.5194/wes-7-161-2022. URL: https://wes.copernicus.org/articles/7/161/2022/.

[49] DNV and Risø National Laboratory. *Guidelines for Design of Wind Turbines*. Hørsholm, Denmark: Det Norske Veritas and Risø National Laboratory, 2002. ISBN: 87-550-2874-2.

[50] J. van der Tempel and P. Molenaar. *Soft- Soft, Soft- Stiff, Stiff- Stiff: Frequency Intervals for Wind Turbine Design*. TU Delft course notes or lecture, cited in Delft OCW materials. 2002.

[51] Fahad Bin Zahid, Zhi Chao Ong, and Shin Yee Khoo. "A review of operational modal analysis techniques for in-service modal identification". In: *Journal of the Brazilian Society of Mechanical Sciences and Engineering* 42.8 (2020), p. 398. DOI: 10.1007/s40430-020-02470-8. URL: https://doi.org/10.1007/s40430-020-02470-8.

[52] K. Kim, K. Lee, S. Park, Y. Bae, and K. Kim. "Resonance Avoidance Control for Semi-Submersible Floating Offshore Wind Turbines". In: *Energies* 14.14 (2021), p. 4138. DOI: 10.3390/en14144138. URL: https://www.mdpi.com/1996-1073/14/14/4138.

[53] J. M. Jonkman, B. J. Jonkman, G. Hayman, et al. *FAST Modular Framework for Wind Turbine Simulation: User's Guide*. Tech. rep. Includes Campbell diagram of the NREL 5-MW baseline turbine. National Renewable Energy Laboratory (NREL), 2016. URL: https://www.nrel.gov/docs/fy16osti/64735.pdf.

[54] C. Devriendt, W. Weijtjens, M. El-Kafafy, and P. Guillaume. "Damping estimation of an offshore wind turbine on a monopile: a comparison of different methods". In: *Proceedings of ISMA2012-USD2012*. 2013, pp. 5115–5129. URL: https://past.isma-isaac.be/downloads/isma2012/papers/isma2012_0511.pdf.

[55] J.M.J. Journée and W.W. Massie. *Offshore Hydromechanics*. First. Delft, Netherlands: Delft University of Technology, 2001.

[56] John Nicholas Newman. *Marine Hydrodynamics*. Updated Edition. Cambridge, MA: The MIT Press, 2018.

[57] G. F. M. Remery and J. A. Hermans. "The Slow Drift Oscillations of a Moored Object in Random Seas". In: *Proceedings of the Offshore Technology Conference (OTC)*. OTC-1500. Houston, TX, USA, 1971. DOI: 10.4043/OTC-1500-MS.

[58] Germanischer Lloyd (GL). *Rules and Guidelines Industrial Services: Guideline for the Certification of Offshore Wind Turbines*. Standard. 2012.

[59] *Environmental Conditions and Environmental Loads – Recommended Practice*. Standard. DNV-GL-RP-C205. 2010.

[60] *Wind Turbines – Part 1: Design Requirements*. Standard. IEC 61400-1. 2005.

[61] *Wind Turbines – Part 3: Design Requirements for Offshore Wind Turbines*. Standard. IEC 61400-3. 2006.

[62] J M Jonkman. *Dynamics Modeling and Loads Analysis of an Offshore Floating Wind Turbine*. Tech. rep. National Renewable Energy Lab. (NREL), Golden, CO (United States), Dec. 2007. DOI: 10.2172/921803. URL: https://www.osti.gov/biblio/921803.

[63] D. C. Montgomery and G. C. Runger. *Applied Statistics and Probability for Engineers*. 3rd. John Wiley & Sons, Inc., 2003.

[64] Leo H. Holthuijsen. *Waves in Oceanic and Coastal Waters.* Definition and role of fetch in wind wave generation. Cambridge University Press, 2007, pp. 37–38. ISBN: 9780521129954. DOI: 10.1017/CBO9780511618536.

[65] W. Wang et al. "Wind Energy Input to the Surface Waves". In: *Journal of Physical Oceanography* (2004). Wind energy input into the ocean is primarily produced through surface waves. URL: https://journals.ametsoc.org/view/journals/phoc/34/5/1520-0485_2004_034_1276_weitts_2.0.co_2.xml.

[66] NOAA Chemical Sciences Laboratory. *Wind Shear Formula.* https://csl.noaa.gov/projects/lamar/windshearformula.html. Accessed: 2025-08-14.

[67] D. L. Elliott. *Adjustment of Land-Based Wind Speed Data to Reflect Offshore Conditions.* Tech. rep. NASA-TM-78927. Accessed: 2025-08-14. National Aeronautics and Space Administration (NASA), 1979. URL: https://ntrs.nasa.gov/api/citations/19800005367/downloads/19800005367.pdf.

[68] Alfredo Peña, Sven-Erik Gryning, and Jakob Mann. "On the length-scale of the wind profile". In: *Quarterly Journal of the Royal Meteorological Society* 136.653 (2010), pp. 2119–2131. DOI: 10.1002/qj.714.

[69] H. El-Shalakany, Jesús Artal-Sevil, V. Ballestín-Bernad, and José Antonio Domínguez Navarro. "Ocean Wave Energy Converters: Analysis, Modeling, and Simulation. Some case studies". In: *Renewable Energy and Power Quality Journal* 20 (Sept. 2022), pp. 783–788. DOI: 10.24084/repqj20.435.

[70] M. J. Tucker. *Waves in Ocean Engineering.* Chichester: Ellis Horwood Ltd., 1991.

[71] Willard J. Pierson and Lionel Moskowitz. "A Proposed Spectral Form for Fully Developed Wind Seas Based on the Similarity Theory of S. A. Kitaigorodskii". In: *Journal of Geophysical Research* 69.24 (1964), pp. 5181–5190. DOI: 10.1029/JZ069i024p05181.

[72] K. Hasselmann, T. P. Barnett, E. Bouws, H. Carlson, D. E. Cartwright, K. Enke, J. A. Ewing, H. Gienapp, D. E. Hasselmann, P. Kruseman, A. Meerburg, P. Müller, D. J. Olbers, K. Richter, W. Sell, and H. Walden. "Measurements of Wind-Wave Growth and Swell Decay during the Joint North Sea Wave Project (JONSWAP)". In: *Deutsche Hydrographische Zeitschrift* (1973). Supplement A(8), No. 12. DOI: 10.1007/BF02245558.

[73] David Apsley. *Waves and Tides: Linear Wave Theory.* Lecture Notes, Hydraulics 3. 2023. URL: https://personalpages.manchester.ac.uk/staff/david.d.apsley/lectures/hydraulics3/WavesLinear.pdf.

[74] Orcina Ltd. *OrcaFlex Manual: Wave Theory.* https://www.orcina.com/webhelp/OrcaFlex/Content/html/Wavetheory.htm. Orcina Ltd. 2024.

[75] Zhen-wei Zhang and Zhi-li Zou. "Application of power law to vertical distribution of longshore currents". In: *Water Science and Engineering* 12.1 (2019), pp. 73–83. DOI: 10.1016/j.wse.2019.04.004. URL: https://www.sciencedirect.com/science/article/pii/S1674237019300250.

[76] J. R. Morison, M. P. O'Brien, J. W. Johnson, and S. A. Schaaf. "The force exerted by surface waves on piles". In: *Petroleum Transactions, AIME* 189 (1950), pp. 149–154.

[77] Orcina Ltd. *Morison's Equation*. Accessed: 2025-05-13. 2024. URL: https://www.orcina.com/webhelp/OrcaFlex/Content/html/Morison%27sequation.htm.

[78] Orcina. *Line Theory: Overview*. Accessed: April 10, 2025. Orcina. 2025. URL: https://www.orcina.com/webhelp/OrcaFlex/Content/html/Linetheory,Overview.htm.

[79] Orcina. *6D Buoys*. Accessed: April 10, 2025. Orcina. 2025. URL: https://www.orcina.com/webhelp/OrcaFlex/Content/html/6Dbuoys.htm.

[80] Orcina Ltd. *Vessels - OrcaFlex Documentation*. Accessed June 2025. 2024. URL: https://www.orcina.com/webhelp/OrcaFlex/Content/html/Vessels.htm.

[81] *Wave Loads and RAOs in OrcaFlex*. Online documentation. Orcina. 2024. URL: https://www.orcina.com/webhelp/OrcaFlex/Content/html/WaveLoads.htm (visited on 09/09/2025).

[82] Orcina Ltd. *OrcaFlex Documentation: Vessel Modelling Overview*. Available at: https://www.orcina.com/webhelp/OrcaFlex/Content/html/Vesselmodellingoverview.htm [Accessed 23 June 2025]. 2024.

[83] *Vessel Load RAOs*. Online documentation. Orcina. 2024. URL: https://www.orcina.com/webhelp/OrcaFlex/Content/html/VesselLoadRAOs.htm (visited on 09/09/2025).

[84] John N. Newman. "Second-order, slowly-varying forces on vessels in irregular waves". In: *Proceedings of the International Symposium on Dynamics of Marine Vehicles and Structures in Waves*. Ed. by R. E. D. Bishop and W. G. Price. London: Mechanical Engineering Publications Ltd, 1974.

[85] Orcina Ltd. *Wave Drift and Sum Frequency Loads*. https://www.orcina.com/webhelp/OrcaFlex/Content/html/Vesseltheory,Wavedriftandsumfrequencyloads.htm. Accessed: 2025-07-01. 2025.

[86] Orcina Ltd. *OrcaFlex Documentation: Inertia Compensation for Vessels*. Accessed on 23 June 2025. 2023. URL: https://www.orcina.com/webhelp/OrcaFlex/Content/html/Vesseltheory,Inertiacompensation.htm.

[87] Orcina Ltd. *OrcaFlex Documentation: Stiffness, Added Mass and Damping*. Accessed on 23 June 2025. 2023. URL: https://www.orcina.com/webhelp/OrcaFlex/Content/html/Vesseltypes,Stiffness,addedmassanddamping.htm#VesselTypeAddedMassAndDampingMethod.

[88] Orcina Ltd. *OrcaFlex Documentation: Morison elements*. Accessed on 26 June 2025. 2023. URL: https://www.orcina.com/webhelp/OrcaFlex/Content/html/Morisonelements.htm.

[89] Orcina Ltd. *OrcaFlex Documentation: Turbines*. Accessed June 2025. Orcina Ltd. 2025. URL: https://www.orcina.com/webhelp/OrcaFlex/Content/html/Turbines.htm.

[90] P. J. Moriarty and A. C. Hansen. *AeroDyn Theory Manual*. Technical Report NREL/EL-500-36881. National Renewable Energy Laboratory (NREL), 2005. URL: https://www.nrel.gov/docs/fy05osti/36881.pdf.

[91] J. M. Jonkman, A. N. Robertson, and G. J. Hayman. *HydroDyn User's Guide and Theory Manual*. Technical Report. National Renewable Energy Laboratory (NREL), 2015. URL: https://www.nrel.gov/docs/fy15osti/63177.pdf.

[92] M. O. Hansen. *Aerodynamics of Wind Turbines*. 3rd. Routledge, 2015. ISBN: 9781138775073.

[93] Lorenz Haid, Gordon Stewart, Jason Jonkman, Amy Robertson, Matthew Lackner, and Denis Matha. “Simulation-Length Requirements in the Loads Analysis of Offshore Floating Wind Turbines”. In: June 2013. DOI: 10.1115/OMAE2013-11397.

[94] Ricardo Faerrón Guzmán, Kolja Müller, Po Wen Cheng, and Luca Vita. *Simulation Requirements and Relevant Load Conditions in the Design of Floating Offshore Wind Turbines*. Slideshare presentation at the International Conference on Ocean, Offshore Arctic Engineering, June 2018. 2018.

[95] N. Neil Kelley and Bonnie Jonkman. *TurbSim User’s Guide: Version 1.50*. Tech. rep. National Renewable Energy Laboratory (NREL), 2009.

[96] Amy Robertson, Jason Jonkman, Fabian Wendt, Andrew Goupee, and Habib Dagher. *Definition of the OC5 DeepCwind Semisubmersible Floating System*. Tech. rep. National Renewable Energy Laboratory (NREL), 2016. URL: https://a2e.energy.gov/api/datasets/oc5/oc5.phase2/files/oc5.phase2.model.definition-semisubmersible-floating-system-phase2-oc5-ver15.pdf.

[97] Orcina Ltd. *Example L02: OC4 Semi-submersible Floating Wind Turbine*. OrcaFlex Example Model. 2020. URL: https://www.orcina.com/wp-content/uploads/examples/l/l02/L02%20OC4%20Semi-sub.pdf.

[98] Brigham Young University FLOW Lab. *CCBlade.jl Documentation*. Accessed: 2025-08-29. 2025. URL: https://flow.byu.edu/CCBlade.jl/stable/reference/.

[99] Torben J. Larsen and Anders M. Hansen. *How 2 HAWC2, the User’s Manual*. Tech. rep. Risø-R-1597(ver. 12.7)(EN). Edited by the DTU Wind Energy HAWC2 Development Team. Roskilde, Denmark: Risø National Laboratory, Technical University of Denmark, May 2019.

[100] L. V. I. Roqueta. “Implementation of Quadratic Damping”. In: *Journal of Physics: Conference Series*. Vol. 1618. 5. Describes Morison drag formulation in the HAWC2–WAMIT coupled model. IOP Publishing, 2020, p. 052032. DOI: 10.1088/1742-6596/1618/5/052032.

[101] Lucas Carmo, Jason Jonkman, and Regis Thedin. “Investigating the interactions between wakes and floating wind turbines using FAST.Farm”. In: *Wind Energy Science* 9.5 (2024), pp. 1105–1126. DOI: 10.5194/wes-9-1827-2024.

[102] José Dias Rodrigues. *Apontamentos de Vibrações de Sistemas Mecânicos*. Lecture notes. Edição 2021.2. 2021.